DESIGN AND MULTI-OBJECTIVE OPTIMIZATION OF A HIGH-SPEED SPINDLE CONSIDERING DYNAMIC AND THERMAL BEHAVIORS

by

SAIF AHMAD AFRIDI

Submitted to the Graduate School of Engineering and Natural Sciences

in partial fulfillment of

the requirements for the degree of Master of Science

Sabancı University

July 2024

DESIGN AND MULTI-OBJECTIVE OPTIMIZATION OF A HIGH-SPEED SPINDLE CONSIDERING DYNAMIC AND THERMAL EFFECTS

DATE OF APPROVAL: July 24, 2024

ABSTRACT

DESIGN AND MULTI-OBJECTIVE OPTIMIZATION OF A HIGH-SPEED SPINDLE CONSIDERING DYNAMIC AND THERMAL BEHAVIORS

SAIF AHMAD AFRIDI

MANUFACTURING ENGINEERING, M.S THESIS, JULY 2024

Thesis Supervisor: Prof. Erhan Budak

Keywords: high-speed spindle, multiobjective optimization, teaching learning based optimization, receptance coupling

High-speed spindles are critical machine tool components with complicated underlying behaviors. Among these, the dynamic and thermal behaviors are the most dominant and interdependent, exhibiting strong links to multiple spindle parameters and performance indicators. This creates a complex design space for spindle designers, warranting the need for a comprehensive optimization approach to maximize spindle performance. While this optimization avenue has been investigated before, the full scope of this problem remains unexplored, particularly in its application to integrated thermal-dynamic models.

This thesis presents a multiobjective optimization approach targeting various facets of thermal and dynamic behaviors of high-speed spindles. A novel optimization approach is developed based on the Teaching Learning Based Algorithm (TLBO) and Non-Dominated Sorting Algorithm (NSGA-III) to identify optimal spindle design configurations and reveal the inherent tradeoffs between dynamic and thermal behaviors of spindles. The optimization study was implemented as a step-by-step procedure across different stages of the spindle design process, considering the prevalent objectives, constraints, and design status at each stage. This approach towards multiobjective optimization can serve as a practical framework for optimizing complex mechanical systems. Additionally, a detailed commentary is also included on the practical design and manufacturing constraints regarding high-speed spindles.

A proof-of-concept study for the reverse identification of spindle parameters using modal parameters is also presented. A database-assisted machine learning approach based on the XGBoost algorithm is used for this. High prediction accuracies were obtained for the machine learning system, indicating that such studies can be explored further.

ÖZET

DİNAMİK VE TERMAL DAVRANIŞLARI DİKKATE ALARAK YÜKSEK HIZLI BİR İŞ MİLİNİN TASARIMI VE ÇOK AMAÇLI OPTİMİZASYONU

SAIF AHMAD AFRIDI

ÜRETİM MÜHENDİSLİĞİ, YÜKSEK LİSANS TEZİ, TEMMUS 2024

Tez Danışmanı: Prof. Erhan Budak

Anahtar Kelimeler: Yüksek hızlı iş mili, çok amaçlı optimizasyon, teaching learning based optimization, receptance coupling

Yüksek hızlı iş milleri, karmaşık temel davranışlara sahip kritik takım tezgahı bileşenleridir. Bu davranışlar arasında dinamik ve termal etkiler en baskın ve birbirine bağımlı olanlardır; ayrıca bu etkiler, iş mili parametreleri ve performans göstergeleriyle güçlü bağlantılar sergiler. Bu durum, iş mili tasarımcıları için karmaşık bir tasarım alanı yaratır ve iş mili performansını en üst düzeye çıkarmak için kapsamlı bir optimizasyon yaklaşımı ihtiyacını ortaya çıkarır. Bu optimizasyon konusu daha önce araştırılmış olsa da, özellikle entegre termal-dinamik modellere uygulanması açısından sorunun tam kapsamı henüz tam anlamıyla keşfedilmemiştir.

Bu tez, yüksek hızlı iş millerinin termal ve dinamik davranışlarının çeşitli yönlerini hedef alan çok amaçlı bir optimizasyon yaklaşımı sunmaktadır. Optimum iş mili tasarım konfigürasyonlarını belirlemek ve iş millerinin dinamik ve termal davranışları arasındaki doğal dengeleri ortaya çıkarmak amacıyla Teaching Learning Based Optimization (TLBO) ve Non-Dominated Sorting (NSGA-III) temel alınarak yeni bir optimizasyon yaklaşımı geliştirilmiştir. Optimizasyon çalışması, her aşamada geçerli hedefler, kısıtlamalar ve tasarım durumu dikkate alınarak, iş mili tasarım sürecinin farklı aşamalarında adım adım bir prosedür olarak uygulanmıştır. Çok amaçlı optimizasyona yönelik bu yaklaşım, karmaşık mekanik sistemlerin optimize edilmesi için pratik bir çerçeve sunabilir. Ek olarak, yüksek hızlı iş millerine ilişkin pratik tasarım ve üretim kısıtlamalarına dair ayrıntılı bir değerlendirme de yer almaktadır.

Son olarak, iş mili parametrelerinin modal parametreler kullanılarak ters tanımlanmasına yönelik bir kavram kanıtlama çalışması sunulmaktadır. Bu amaçla, XGBoost algoritmasına dayalı veritabanı destekli bir makine öğrenimi yaklaşımı kullanılmıştır. Makine öğrenimi sistemi için yüksek tahmin doğrulukları elde edilmiş olup, bu tür çalışmaların daha fazla araştırılabileceğini göstermektedir.

ACKNOWLEDGEMENTS

I would like to express my gratitude to my advisor, Prof. Erhan Budak, for providing me with this opportunity and for his support and guidance throughout the course of my study. Your passion for research is deeply inspiring. I also wish to acknowledge the help of my project partner, Esra Yüksel, whose contributions were fundamental to my work.

I extend my special thanks to my colleagues and fellow researchers in the Manufacturing Research Laboratory (MRL) for their friendship and engaging discussions. I appreciate the time spent with Arash, Amin, Vahid, Suzan, and Saltuk; your presence made the lab a welcoming and positive environment.

I also acknowledge the support of Muharrem Bey, Ertuğrul Bey, Süleyman Bey, and the Maxima team for their significant contributions in designing and manufacturing the spindle. These interactions provided me with valuable practical skills.

To my friends and family, especially my wife, Sadia, your encouragement, patience, and unwavering belief in me have been a constant source of strength.

I would also like to acknowledge TÜBİTAK, whose financial support made this research possible.

To my family and friends.

TABLE OF CONTENTS

LIST OF TABLES

LIST OF FIGURES

LIST OF ABBREVIATIONS

FRF	Frequency Response Function
RPM	Revolutions Per Minute
FE	Finite Elements
RCSA	Receptance Coupling Substructure Analysis
ACBB	Angular Contact Ball Bearing
CFD	Computational Fluid Dynamics
PSO	Particle Swarm Optimization
TLBO	Teaching Learning Based Optimization
NSGA-III	Non-Dominated Sorting Genetic Algorithm-III
ZDT	Zitzler-Deb-Thiele
NBR	Nitrile Butadiene Rubber

1. INTRODUCTION

High-speed machining is a cornerstone of modern machine tools technology, offering remarkable benefits in terms of cost-saving, productivity, machinability of novel materials, micro-machinability, and quality of production [1]. Its capacity to achieve finer surface finishes and tighter tolerances has attracted industries where precision is paramount, such as aerospace, automotive, and medical device manufacturing.

Reaching such high speeds, however, comes with its fair share of problems. The machine tool infrastructure, particularly high-speed spindles, must be capable of withstanding the additional dynamic and thermal loads exclusive to high-speed operation [2]. This requires extensive re-designing of conventional machine tool spindles, including the utilization of high-speed rotodynamic theories, better component selection, and the inclusion of various auxiliary devices/systems to tackle the specific challenges of high-speed operation.

An extensive body of knowledge focused on various aspects of high-speed spindle design and modeling has been developed over the past four decades. The following section provides a summary of these studies.

1.1. Thermo-Dynamic Considerations in High-Speed Spindle Design

The primary challenges in high-speed spindle design come from the dynamic and thermal behaviors since they dominate the problems faced during operation. The dynamic behavior of spindles, judged primarily by its frequency response function (FRF), is well-known to be speed-dependent [3], [4]. The FRF is considered a standard indicator of

spindle dynamic performance as it carries crucial information like natural frequencies, damping ratios, mode shapes, and is highly useful in process-driven applications like the calculation of chatter stability limits [5]. The thermal performance of high-speed spindles is characterized by performance-driven factors like thermal expansion at the spindle tip, which contributes to machining accuracy, and failure-centric factors like peak temperatures at bearings and shaft, heat transfer coefficients, and cooling/lubrication system efficiencies. These parameters are often reliant on each other, creating a highly interdependent system of dynamic and thermal behaviors.

Due to this multidisciplinary nature of high-speed spindles, a significant portion of the literature focuses on developing integrated thermo-dynamic models for spindles and investigating their interdependencies.

In this regard, the study of Li et al. [6] is a benchmark in integrated spindle thermo-dynamic modeling. They developed a modular thermo-mechanical model comprising bearing, dynamic, and thermal modules to predict speed-varying temperatures, thermal growth, and dynamic response. The models were experimentally validated for speeds up to 30,000 RPM. Their study identified increasingly non-linear behavior of bearings and spindle dynamics at higher speeds. However, their model disregarded the centrifugal effects on the spindle shaft.

The work in Lin et al. [7] used a similar FE approach to predict spindle behavior and concluded that centrifugal effects significantly ‘soften’ the shaft at high speeds and are the main contributors to the shift in spindle performance at high speeds. Their model considered thermally induced bearing preloads and centrifugal and gyroscopic effects on the spindle shaft at speeds up to 25,000 RPM. However, their bearing stiffness module assumes full ball contact loading, thus ignoring crucial high-speed effects like skidding. Fang et al. [8]developed a mechanistic model for high-speed bearings to investigate the skidding effect, where the ball-raceway contact transitions into the rolling-sliding regime from pure rolling. They observed that skidding appears at speed above 8,000 RPM in their design, changing the heat generation behavior. This study prompts spindle designers to include skidding thresholds while selecting bearings to avoid loss of ball-raceway contact at higher speeds. Cao et al. [9] presented a more application-oriented research to study the effects of bearing preloads and operating speed on milling stability. They showed that stiffness increases with preloads but tends to decrease as speed increases. They also

concluded that spindle modeling accuracy can be improved by considering the effects of mounting joints with machine tool, signifying the need for rigid joints when designing new spindles. Matsubara et al. [10] adapted an experimental approach to characterize the effects of speed-dependent thermal behaviors on spindle stiffness in the radial direction. They concluded that there is no significant linkage between radial stiffness and speed-dependent heat generation, which indicates that thermally induced preloading is generally more applicable in the axial direction.

The role of bearing stiffness is significant in determining spindle dynamics; thus, it has been thoroughly investigated as a separate topic in many studies. Among early studies, the quasi-static models of Jones [11] and DeMul [12] are considered fundamental in determining the load-deformation relationship between bearing elements and the bearings' Jacobian stiffness matrix. Gupta [13] developed a dynamic model to obtain time-varying bearing response. The core feature of these analytical methods is their leveraging of classical contact theories (for example Hertzian contact) to define the interaction between bearing elements, which makes them fairly accurate in predicting bearing response. For an in-depth review of the literature in this field, readers are directed to Hong et al. [14].

Apart from bearings, other main contributors to spindle dynamics are the shaft geometry and spindle assembly. Ertürk et al. [15] applied the receptance coupling substructural analysis (RCSA) method to compute the dynamic response of a shaft-holder assembly. Their study revealed the effects of using different shaft geometries on the FRF, particularly the length of the spindle tail section. Özşahin et al. [16] extended their approach to include the effect of contact mechanics at the bearing-shaft interfaces. Li et al. [17] conducted an important study investigating the effects of bearing configurations on spindle dynamics. Angular contact ball bearings (ACBB) can be assembled on the shaft in various configurations, namely O-, X-, or tandem. This manifests as differences in the linear-rotational coupling between the bearing and shaft, which in turn changes the fundamental natural frequencies. The authors demonstrated that assigning negative values to specific off-diagonal terms in the bearing Jacobian stiffness matrix, depending upon the bearing's direction, is necessary to accurately model the spindle equation of motion. Rabréau et al. [18] added further context to this study by mapping axial force versus displacement relationships for different preloading methods and speeds.

Kazi [19] modeled the dynamic characteristics of multi-stepped rotor-bearing units, demonstrating significant changes in critical speeds with changes in diameters of rotor sections on the shaft. Liu et al. [20] established the influence of the tightness of bearing interference fits on bearing stiffness by considering radial deformations in the inner ring due to tight tolerances. They noted that this dependence is high for low preload conditions, which is a characteristic feature in high-speed spindles. Thus, signifying the need to be careful in determining design tolerances and assembling of bearings on the shaft.

Similarly, there is a group of researchers who have investigated the thermal aspects of spindle structures. Bossmanns et al. [21] developed a finite difference thermal model based on their earlier work on power distribution in spindle structures. They identified relevant heat sources and sinks and the heat transfer mechanism between them to predict heat distribution in a high-speed spindle at various speeds. Chen et al. [22] used an autoregression thermal error model from on-line thermal displacement measurements to study spindle thermal growth. They concluded that spindle thermal behavior is highly nonlinear and complicated due to the numerous joints and contact interfaces. Liu et al. [23] characterized spindle thermal errors with an FE-based model by assuming that spindle axial and radial thermal errors are isolated for their analytical model. Meng et al. [24] concluded that the topography of contact surfaces has significant effects on the temperature distribution and temperature rise in motorized spindles. They used the fractal contact theory to determine the thermal contact resistances for their thermal network model. Jorgensen et al. [25] characterized the effects of thermal expansion on stiffness in shaft-bearing systems.

Overall, there is a strong body of knowledge in the thermo-dynamic modeling of machine tool spindles. The design and optimization work presented in this thesis was based on the knowledge gained from this research.

1.2. Optimization of Spindles

The literature discussed in the previous section showed that spindle dynamic and thermal performance are dependent on a wide variety of parameters coming from design, assembly, and component selection. Their effects on performance are non-linear, interdependent, and significant. Thus, they form a multi-dimensional, complex design space that poses significant challenges in spindle design. This situation creates a rich opportunity for optimizing spindle designs, which has been availed by numerous researchers over the years.

This section will present a chronological survey of the major spindle optimization studies reported in the literature.

The early studies in spindle optimization focused on basic spindle structures (shaft-bearing systems). Hamada et al. [26] utilized classic Kuhn-Tucker conditions to find pareto optimal solutions for the best spindle weight, static compliance, and torsional angular natural frequency. Although their selection of objectives and choice of analytical sensitivity analysis is unique, the optimization methodology solved the multi-objective problem as a single-objective problem using self-assigned weights, restricting the flexibility in mapping the true pareto curve.

Spindle deflection at a single point was minimized using gradient-based methods by investigating bearing positions and lateral bearing stiffnesses in Hoyt et al. [27]. However, the global minimum was not guaranteed, and the bearing stiffness values did not translate directly to real bearings since theoretical springs were used.

Maeda et al. [28] were amongst the first to apply optimization methods to more realistic spindle structures. In their work, they optimized bearing spans (locations) to maximize the chatter stability limit for a pre-defined cutting condition. They considered axial and radial bearing stiffnesses as well as geometric constraints imposed by their lubrication system. Ertürk et al. [15] presented an exploratory sensitivity analysis, mapping the effects of various terms in the bearing stiffness matrix and shaft dimensions on the tooltip

FRF. A similar sensitivity analysis was conducted by Lin et al. [29], but for high speeds. These studies revealed important monotonic and non-monotonic trends concerning spindle dynamics, which are helpful in planning spindle optimization studies with an informed decision variable selection.

Similar efforts to map the design space have been made with respect to structural elements in spindles. Erturk et. al. [15] reported on the dynamic absorber effect observed when the length of the spindle's tail section is increased. The tail length tuning creates the dynamic absorber effect, where multiple modes merge and attenuate each other's response. This phenomenon was demonstrated as an optimization problem by Mohammadi et al. [30], who found the exact dimensions of the tail extension theoretically required to maximize dynamic performance.

Experimentation-based optimization is a major challenge in research on machine tool spindles. They are expensive and complex machine components, limiting the flexibility of researchers in designing complicated experiments for system optimization. Despite these problems, some studies have produced interesting results from experimentation-based methods. Kim et al. [31] used a design of experiments approach to minimize spindle-tip thermal displacement by mapping the design space for six variable including coolant temperature, preload, and spindle dimensions. In Yue et al. [32] optimal temperature-sensitive measurement points for spindle thermal error modelling were identified by placing 12 thermal sensors on a milling spindle. Comprehensive experimental studies on machine tool spindles, however, remain a challenge due to design complexity and high costs.

The recent development of high computational power and high-fidelity finite element methods have provided a workaround experimental challenges by offering the alternate option to conduct investigation in simulation environments. Fan et al. [33] performed a simulation-based optimization of thermal contact resistances at shaft-bearing interfaces to minimize thermal elongation. They performed experimental verification for just the optimal solution. The use of computational fluid dynamics is another convincing application of simulation-based optimization as an experimental alternative is impractical. The studies of Koch et al. [34] and Li et al. [35] are notable examples of this. Both evaluated the thermal performance of different cooling channel patterns and dimensions using CFD-based design of experiments. The latter verified their optimal

solution with an experiment. However, such simulation systems, while allowing for elaborate analyses and circumventing rigorous experimentation, are quite time-taking and lack the reliability of pure analytical and experimental methods.

In short, researchers in the past have approached spindle optimization from multiple perspectives, taking into account different behaviors, objectives, and decision variables.

It is interesting to note here that while the modeling efforts for high-speed spindles have covered a vast majority of spindle behaviors and their interdependencies, the literature on optimization of high-speed spindles usually focuses on a single aspect of spindle behaviors at a time. Particularly, dynamic and thermal behaviors were rarely assessed together in an optimization study. A key reason for this inconsistency between modeling and optimization can be the inability of conventional optimization methods to effectively deal with complex, multi-dimensional design spaces. Studying multiple spindle behaviors requires defining multiple optimization objectives, which seriously complicates the problem of finding an optimal solution set, both in terms of theory and computational effort. Initial studies solved this problem by either converting multiobjective problems to a single objective problem or breaking down the broad problem into smaller, manageable problems [26], [36]. However, this is not ideal as the composite single objective function is essentially a weighted average of its constituent multiple objectives. Since these weights are self-assigned based on intuition, there is no guarantee that the single objective problem is fully representative of the original multiobjective problem.

In recent years, the concept of multiobjective optimization has become popular and provides a better alternative for solving such problems. The crux of these techniques is to correctly identify the pareto front, which is essentially a set of equally optimal but unique solutions in a multiobjective optimization problem. A solution is considered pareto optimal if there does not exist another solution that is better than it in all objectives simultaneously. Additionally, the pareto front is also helpful in observing the tradeoff between different objectives, should there exist any. These concepts are explained through Figure 1. In this dual-objective case, both objective functions are to be minimized. The plot shows a group of solutions in the objective space, only a subset of which are the pareto optimal solutions. Each of these solutions represents a case where, if one objective improves, the other suffers. Thus, a tradeoff is identified along with a set of optimal

solutions. This information is crucial for the designers of the system, who can choose a solution that best suits their requirements.

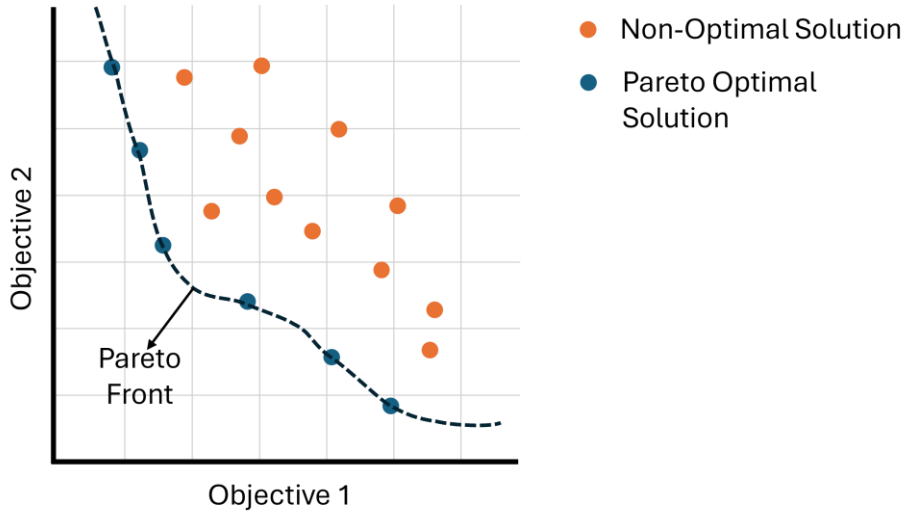

Figure 1: Pareto front

These multiobjective techniques have lately gained traction in spindle optimization efforts. The study of Tong et al. [36] is a strong example of multiobjective optimization, who formulated multiple case studies for multiobjective optimization of spindles and used the Particle Swarm Optimization (PSO) algorithm to find pareto optimal solutions for bearing locations and preloads. However, they also used composite functions to represent multiple objectives and presented their study as different multiobjective case studies rather than employing a comprehensive approach. In their unique energy-based research, Yi et al. [37] applied the multi-objective Teaching-Learning Based Optimization (TLBO) to find numerous pareto optimal design configurations for an energy-efficient lathe spindle. Pereira et al. [38] compiles an excellent review on the applications of multiobjective optimization in engineering problems. These studies strongly indicate that multiobjective approaches carry potential to optimize multi-disciplinary systems like high-speed spindles.

There are, however, clear gaps in the literature that can be addressed. These are identified as:

- Researchers have not yet fully explored multiobjective schemes in the field of spindles. Machine tool spindles are complicated systems with multiple performance indicators and conflicting behaviors, presenting an excellent opportunity for implementing such schemes.

- Most optimization studies have focused on either specific sub-systems or simplified models of spindles. Considering more realistic spindle geometries and using integrated models representing different behaviors can achieve more realistic results.
- Optimization algorithms are applied on already built spindle models, which cannot be altered much, constricting opportunities to optimize the structure. No study from the cited literature provides a practical optimization framework that spindle designers can use during the product design stage.

The objective of this thesis is to present a practical and holistic approach towards spindle design optimization. To do so, various past works and established meta-modeling techniques are leveraged in a novel multi-objective optimization scheme.

The implementation of this scheme is discussed in light of the practical constraints faced at different stages of our project, which is a more pragmatic application of optimization.

1.3. Thesis Scope and Outline

The work presented in this thesis was conducted as part of a research project concerning the design and manufacturing of a 40,000 RPM high-speed spindle. At the time of writing this thesis, the design process was finished, and the production of the spindle was underway.

Therefore, much of the presented work is simulation-based. However, care has been taken wherever possible to utilize proven analytical methods with strong references from literature. Experimentally backed results are planned to be shared after completion of manufacturing.

The scope of this thesis is mainly concerned with the optimization aspect of the aforementioned project. In this regard, the thesis is organized as follows:

- **Chapter 2** provides a theoretical background on the in-house dynamic and thermal spindle models used for optimization. Additionally, a detailed description

and verification of the multi-objective scheme developed in this work is also presented.

- **Chapter 3** presents the four-stage design-guided optimization strategy adapted in this work. The chapter follows the progression of the project from an optimization point of view, with each stage representing a different period in the project timeline.
- **Chapter 4** includes detailed notes on different design and manufacturing aspects of the project. The salient features of our design and manufacturing considerations are discussed.
- **Chapter 5** presents a proof-of-concept study on the machine learning-assisted reverse identification of spindle parameters from modal parameters acquired from the FRF.
- **Chapter 6** summarizes the key findings of this study, reflects on the significance of the research, and suggests directions for future works.

1.4. Summary

This chapter presented a detailed literature review on various aspects of high-speed spindles. The review covered key benchmark studies and the evolution of modeling techniques over the past few decades.

Initially, the modeling efforts for spindle dynamics and thermal behaviors was covered. Integrated thermal-dynamics modeling was highlighted as a necessary approach for investigating high-speed spindles.

Then, a comprehensive review of spindle optimization efforts was presented in a chronological manner, covering various optimization objectives and algorithms. It was identified that multiobjective optimization using integrated thermal-dynamic modeling is unexplored.

2. ANALYTICAL METHODS

The primary goal of this work is to develop an optimization scheme to find the best-performing design parameters for a high-speed spindle. The main prerequisite for this is to have high-performance, high-fidelity models that adequately estimate different spindle behaviors.

In this regard, various independently developed in-house spindle codes were used as the base models for optimization studies. The upcoming sections briefly explain the theoretical background of these models.

The later sections explain how these independent models were combined to develop the integrated thermal-dynamic spindle model used for optimization. Finally, a detailed discussion on the theory and validation of the multi-objective optimization scheme is presented.

2.1. Spindle Dynamics

The dynamic response of a spindle represents one of its core design interests, considering that machine tools are subjected to complex dynamic loads across a wide frequency spectrum. In line with the reviewed literature, the FRF at the spindle tip is deemed a suitable candidate for optimizing dynamic response.

To effectively model the FRF, the Receptance Coupling Substructural Analysis (RCSA) technique is used.

2.1.1. Receptance Coupling Substructural Analysis

RCSA analytically predicts the frequency response function of mechanical assemblies by mathematically coupling their individual substructure endpoint receptances. It was first used for machine tool spindles by Schmitz [39] to predict tooltip FRF and has since been adapted as one of the primary spindle dynamics analysis tools. Research works like [40] and [16] have further solidified the suitability of this method for analyzing spindle dynamics. Figure 2 illustrates the general workflow of the RCSA algorithm.

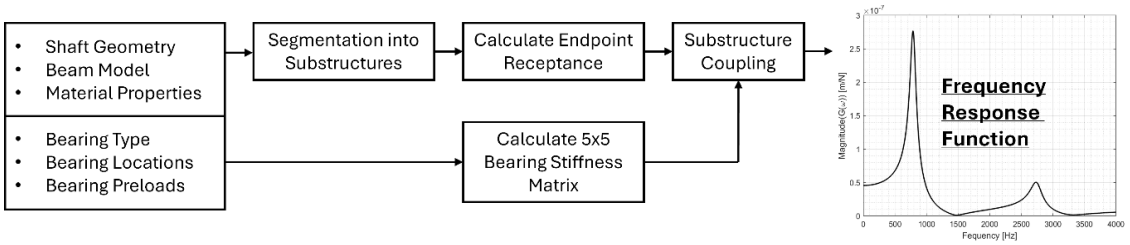

Figure 2: Receptance coupling substructural analysis process

The first step in the RCSA algorithm is to divide the structure into its respective substructures, as guided by the used. The substructures in question are the different sections of the spindle shaft with unique geometric or material properties. In the next step, it computes the endpoint receptance matrices for each substructure.

To compute the endpoint receptance matrices for each substructure, the Timoshenko beam model [41] has been applied to hollow round beams in free-free condition. The Timoshenko beam model is appropriate to use in this case as it considers shear deformation and rotational effects in the beam. Both effects are important to consider in short beam sections, that are characteristic of spindle shaft geometries.

Following the complete solution of the Timoshenko beam's partial differential equations of motion with forced harmonic input, the endpoint receptance matrices for each

substructure are found as in Eq. 2.1 The details of the solution procedure can be found in [42].

$$Ra, ij(\omega) = \begin{bmatrix} h_{ij} & l_{ij} \\ n_{ij} & p_{ij} \end{bmatrix} \tag{2.1}$$

Here, the square matrix, $R_{a,ij}$, is 8x8 in size, and is frequency-dependent, with frequency denoted by ω. The matrix component, h_{ij}, l_{ij}, n_{ij}, and p_{ij}, are 2x2 matrices representing different receptance forms of the beam segment.

The superscripts, *h, l, n,* and *p* are the displacement-force, displacement-moment, rotation-force, and rotation-moment receptance functions of the corresponding substructure; respectively. The subscripts, *i* and *j*, are the points of response and excitation, respectively. For example, h_{12}, represents the transverse displacement response of the beam at point 1 when a harmonic force is applied at point 2.

The RCSA method is then applied to analytically couple these substructure receptances one by one. The general formula to compute the assembly response of the new structure, C, from two substructures, A and B, is computed using Eqs. 2.2-2.5. Here, each substructure matrix (A, B, C) is of the form Eq. 2.1.

$$[C_{11}] = [A_{11}] - [A_{12}][R_2]^{-1}.[A_{21}] \tag{2.2}$$

$$[C_{12}] = [A_{12}].[R_2]^{-1}.[B_{12}] \tag{2.3}$$

$$[C_{21}] = [B_{21}][R_2]^{-1}.[A_{21}] \tag{2.4}$$

$$[C_{22}] = [B_{22}] - [B_{21}][R_2]^{-1}.[B_{12}] \tag{2.5}$$

Depending upon the nature of the joint between the two substructures, the coupling can be rigid or non-rigid. A rigid coupling applies when no flexibility is present at the joint. This is the case for substructures that are part of the same solid entity (shaft), and without external components like bearings, sleeves, or nuts.

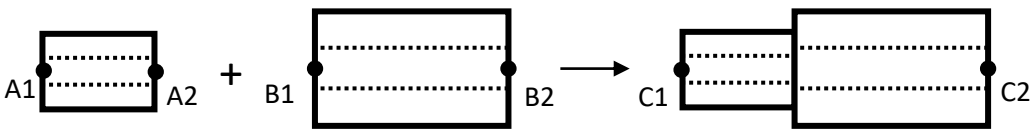

Figure 3: Rigid substructure coupling

The difference between these two coupling types appears in the matrix R_2. For two rigidly coupled substructures (Figure 3), R_2 is defined by Eq. 2.6.

$$R_2 = R_{A,22} - R_{B,22} + K^{-1} \tag{2.6}$$

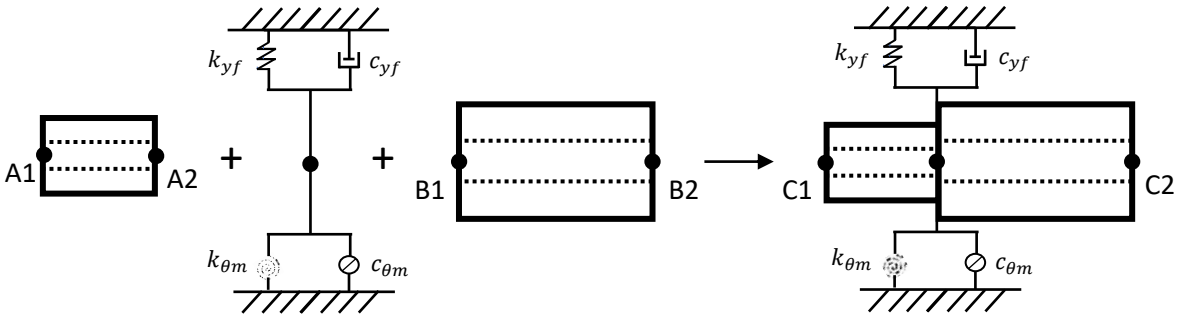

Figure 4: Non-rigid substructure coupling

In the case the shaft segment has a bearing (Figure 4) the connection becomes non-rigid due to the stiffness and damping introduced by the bearing. To couple these substructures, the matrix R_2 includes the bearing stiffness matrix, K, as given in Eq. 2.7 and Eq. 2.8, respectively.

$$R_2 = R_{A,22} - R_{B,22} + K^{-1} \tag{2.7}$$

$$K = \begin{bmatrix} k_{yf} + i\omega c_{yf} & k_{\theta f} + i\omega c_{\theta f} \\ k_{ym} + i\omega c_{ym} & k_{\theta m} + i\omega c_{\theta m} \end{bmatrix} \tag{2.8}$$

In Eq. 1.8, k_{yf}, k_{ym}, $k_{\theta f}$, and $k_{\theta m}$, represent the displacement-force, displacement-moment, rotation-force, and rotation-moment stiffnesses of the bearing, respectively. These four stiffness values are extracted from the standard 5x5 bearing stiffness matrix, which is discussed in the next section.

The corresponding damping values are generally difficult to compute analytically as they depend on highly variable factors like bearing condition, material, assembly inconsistencies, and temperature. The damping values used in this work are either taken from the referenced literature or reverse identified from experimental results.

2.1.2. Bearing Modeling

The preceding section mentioned the use of bearing stiffness terms to couple non-rigid shaft segments. A 5-degree of freedom analytical bearing model developed at the Vibration & Measurement Lab, Kumoh National Institute of Technology is used in this work. It is built for Angular Contact Ball Bearings (ACBB), which are the bearing types used in our high-speed spindle design.

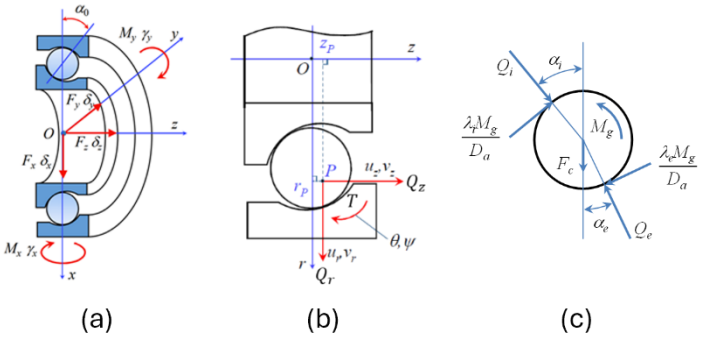

Figure 5: Bearing coordinate systems and ball free-body diagram, (a) Global coordinate system, (b) Local coordinate system, and (c) Free-body diagram of the bottom ball

Figure 5 shows the global coordinate system, the local coordinate system, and the free-body diagram for an arbitrary rotating element of an ACBB. In Figure 5(a) and Eq. 2.9, the external load vector, $\{F\}$, and the corresponding displacement vector, $\{\delta\}$, are defined respectively. Here, the force component F_z is of primary importance as it represents the axial preload force, which will be discussed as the main stiffness-inducing parameter in subsequent sections.

$$\{F\} = \{F_x,\ F_y,\ F_z,\ M_x,\ M_y\}^T, \{\delta\} = \{\delta_x,\ \delta_y,\ \delta_z,\ \gamma_x,\ \gamma_y\}^T \tag{2.9}$$

Figure 5(b) and Eq. 2.10 illustrate the displacement vector of the inner ring cross-section, and the corresponding inner ring contact load vector defined at the local ball.

$$\{u\}^T = \{u_r, u_z, \theta\}, \qquad \{Q\}^T = \{Q_r, Q_z, T\} \tag{2.10}$$

Here, u_r, u_z, θ are the radial displacement, axial displacement, and rotation of the inner ring. Q_r, Q_z, T represent the radial and axial contact loads, and the contact moment at the local ball.

Figure 5(c) shows the free-body diagram for one of the bottom balls of an ACBB. Here, Q_i and Q_e denote the contact loads between the inner and outer rings, respectively. Their corresponding local contact angles can be expressed as α_i and α_e. The centrifugal force of the ball, F_c, is expressed in Eq. 2.11. Here, m, d_m, and ω_c are the mass of the ball, bearing pitch diameter, and ball orbital speed, respectively.

$$F_C = {}^1\!/_2\, m d_m \omega_c^2 \tag{2.11}$$

$$m_g = {}^1\!/_{10}\, m {D_B}^2 \omega_c \omega_r \sin\beta \tag{2.12}$$

The gyroscopic moment m_g is expressed by Eq. 2.12. D_B is the diameter of the ball, and ω_r and β are the ball's rotational speed and the pitch angle, respectively. The respective contact loads at ball-inner ring contact and the ball-outer ring contact are obtained from the Hertz contact theory as follows:

$$Q_i = K_i \delta_i^{1.5}\,, Q_e = K_e \delta_e^{1.5} \tag{2.13}$$

Here, δ_i and δ_e are the deformations between the ball and the inner and outer rings, while K_i and K_e are the corresponding load-displacement coefficients. Using the free-body diagram in Figure 5(c), Eqs. 2.14 equation can be obtained:

$$\begin{gathered} Q_i \cos(\alpha_i) - Q_e \cos(\alpha_e) + F_c - \frac{M_g}{D}(\lambda_i \sin(\alpha_i) - \lambda_e \sin(\alpha_e) = 0 \\ Q_i \sin(\alpha_i) - Q_e \sin(\alpha_e) - \frac{M_g}{D}(\lambda_i \cos(\alpha_i) - \lambda_e \cos(\alpha_e) = 0 \end{gathered} \tag{2.14}$$

Here, λ_i and λ_e denote the support ratios of the inner and outer rings to gyroscopic moments. The outer race control mode is assumed to be defined by complete rolling motion in a high-speed application, for which λ_e=2, otherwise λ_i=λ_e=1.

The equilibrium equation for the entire bearing in the global coordinate system is expressed by Eq. 2.15.

$$\{F\} + \sum_{j=1}^{Z} \left[T_\psi\right]_j^T \{Q\}_j = 0 \tag{2.15}$$

Here, Z is the number of balls and $\left[T_\psi\right]_j^T$ is a transformation matrix from the center coordinates of the inner ring curvature radius to the global coordinates. Eq. 2.14 and Eq. 2.15 are non-linear, and Eq. 2.14 is obtained while solving Eq. 2.15. In this process, all displacements of the bearing centre coordinates are calculated.

The 5x5 bearing stiffness matrix, *K*, is obtained from Eq. 2.15 as follows:

$$K = \left[\frac{\partial\{F\}}{\partial\{\delta\}}\right] = -\sum_{j=1}^{Z} \left[T_\psi\right]_j^T \left[\frac{\partial\{Q\}_j}{\partial\{u\}}\right] \left[T_\psi\right]_j \tag{2.16}$$

The full form of the K matrix is in Eq. 2.17.

$$[K] = \begin{bmatrix} k_{xx} & k_{xy} & k_{xz} & k_{x\theta_x} & k_{x\theta_y} \\ k_{yx} & k_{yy} & k_{yz} & k_{y\theta_x} & k_{y\theta_y} \\ k_{zx} & k_{zy} & k_{zz} & k_{z\theta_x} & k_{z\theta_y} \\ k_{\theta_x x} & k_{\theta_x y} & k_{\theta_x z} & k_{\theta_x\theta_x} & k_{\theta_x\theta_y} \\ k_{\theta_y x} & k_{\theta_y y} & k_{\theta_y z} & k_{\theta_y\theta_x} & k_{\theta_y\theta_y} \end{bmatrix} \tag{2.17}$$

F

our terms from Eq. 2.17 are used to populate the stiffness matrix, K, in Eq. 2.8. The displacement-force (kyf) and rotation-moment (kθm) terms exhibit the following relationships:

$$kyf = kxx = kyy \tag{2.18}$$
$$k\theta m = k\theta x\theta x = k\theta y\theta y$$

The remaining two terms, $k_{\theta f}$ and k_{ym} are represented by the dominant off-diagonal terms in the bearing stiffness matrix, defining the cross-interactions between rotational and transverse motions of the bearing. [17] showed that these four terms ($k_{x\theta_y}$, $k_{\theta_y x}$, $k_{\theta_x y}$, $k_{y\theta_x}$) are the only dominant off-diagonal terms if there is no external radial load and only axial preload is applied, which is the case for this study. Furthermore, in this case, all four of these terms are equal. Therefore,

$$(k_{\theta f} = k_{ym}) = (kx_{\theta y} = k_{\theta yx} = k_{\theta xy} = ky_{\theta x}) \quad (2.19)$$

They also demonstrated that the sign of these terms depends on the ACBB's orientation with respect to the coordinate system of the shaft. The bearing configuration of the existing spindle is "O-configuration" or "back-to-back", so the off-diagonal terms are taken as negative for front bearings (positive bearings) and as positive for rear bearings (negative bearings).

2.2. Thermal Modeling

An in-house finite element-based metamodel was used to represent the thermal behaviors of high-speed spindles. Relevant heat sources, heat sinks, and thermal resistance interfaces are included in the analysis, as shown in Figure 6.

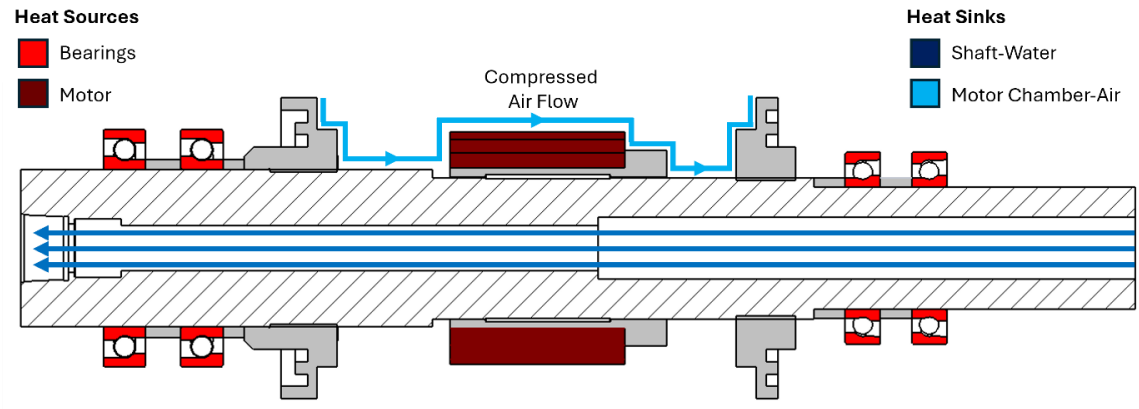

Figure 6: Heat sources and sinks in spindle

2.2.1. Heat Sources

The main heat sources in a high-speed motorized spindle are the bearings and the built-in motor.

Bearing frictional moments of inner (M_i) and outer (M_e) rings are calculated for thermal modeling as indicated in Eq. 2.20 and Eq. 2.21 and in [43]. f_o and f_1 are dependent upon the bearing type and lubrication conditions, D is the bearing diameter, γ is kinematic viscosity, and ω_c denotes the rolling velocity.

$$M_i = \left[0.675 f_o (\gamma \omega_c)^{2/3} D^3 + f_1 \left(Q_i / Q_{i\_max}\right)^{1/3} Q_i D\right] \tag{2.20}$$

$$M_e = \left[0.675 f_o (\gamma \omega_c)^{2/3} D^3 + f_1 \left(Q_e / Q_{e\_max}\right)^{1/3} Q_e D\right] \tag{2.21}$$

Additionally, the spin moments of the bearings at inner and outer rings (M_{si}) and (M_{se}) are calculated as shown in Eq. 2.22 and Eq. 2.23, respectively. Here, μ_s is the friction coefficient, a_i and a_e are the major axes of the contact at bearing rings.

$$M_{si} = 3\mu_s Q_i a_i \zeta / 8 \tag{2.22}$$

$$M_{se} = 3\mu_s Q_e a_e \zeta / 8 \tag{2.23}$$

The results from Eqs. 2.20-2.23 are used to compute the bearing heat generation at inner (H_i) and outer (H_e) rings, as given by Eq. 2.24 and Eq. 2.25. The resultant heat generation values are applied as boundary conditions in the finite element model.

$$H_i = \omega_c . M_i + \omega_{ri} . M_{si} \tag{2.24}$$

$$H_e = \omega_c . M_e + \omega_{re} . M_{se} \tag{2.25}$$

Regarding the heat produced by built-in motor for high-speed spindles, there is no well-established calculation model in the litrature. Therefore, an emprical heat genearation formula given by the step motor producer, Akimmetal [44], was used.

2.2.2. Heat Sinks

Two types of heat sinks are considered for the development of the finite element model, as shown in Figure 6. Firstly, the heat disippation due to forced convection caused by through-shaft cooling. The internal wall of the shaft's central cooling hole is taken as the cooling interface. This hole was initially planned to have a supply of flowing water. However, due to manufacturing constraints, this feature was not part of the final design, but will be discussed in subsequent chapters.

The forced convection coefficient (h_{liqiud}) inside the shaft cooling hole is calculated by Eq. 2.26 and Eq. 2.27. In Eq. 2.26, Nu is Nusselt number, k_{liquid} is fluid conductivity, and D is the cross-sectional flow of a tube. The Reynolds number is calculated by considering u (average speed of fluid) and η (fluid kinematic viscosity).

$$h_{liqiud} = {}^{Nu.\,k_{liquid}}/_{D} \tag{2.26}$$

$$Re = {}^{u.\,D}/_{\eta.\,k_{liquid}}\text{, where } u = \sqrt{u_{axial}^2 + u_{radial}^2} \tag{2.27}$$

Secondly, the finite element model also accounts for thermal resistances introduced by auxiliary shaft components like locknuts and sleeves. These components are press-fit on the shaft, enlarging the forced convection area on the shaft. Their outer diameter surface is mostly exposed to the internal space of the spindle assembly, which is filled with circulating air for cooling and sealing purposes.

The forced convection coefficients (h_{air}) at these interfaces are calculated using Eq. 2.28 and Eq. 2.29. Here, ϑ_{air} is kinematic viscosity and l_{shaft} is perimeter of the shaft assembly with auxiliary components. The Reynolds number is predicted by

employing u_{air} (air speed around shaft), which depends on n, the spindle speed. These predicted forced convection coefficients are applied as boundary conditions to the FE model.

$$h_{air} = {Nu.\vartheta_{air}}/{l_{shaft}} \text{ , where } l_{shaft} = \pi d_{shaft} \tag{2.28}$$

$$Re = {u_{air} l_{shaft}}/{\vartheta_{air}} \text{ , where } u_{air} = {l_{shaft}.n}/{60} \tag{2.29}$$

Since this finite element analysis is to serve as an input to the optimization algorithm, it needs to be rerun multiple times with different inputs. Therefore, parametric finite element models are used to conveniently pass variables in the design to the simulation. In this case, these are the changes in sensitive shaft dimensions.

To ensure that the finite-element simulation is up-to-speed with the other algorithms (bearings, dynamics, optimizer), a response surface-based reduced-order model is created beforehand by running the simulation an appropriate number of times. The output of this procedure is a *'.fmu'* extension file, which can conveniently be run from third-party platforms like *MATLAB* and has a runtime comparable to the other models.

This model was utilized in section 3.3, where the exact details can be found. Moreover, it is to be noted that the details in this section are specific to the geometry of our design.

2.3. Multi-Objective Optimization

The dynamic and thermal spindle models explained in sections 2.1 and 2.2 were used as base metamodels in the optimization scheme.

A heuristic approach is preferred for this optimization problem owing to the large size of the design space, difficulty in analytically handling the sensitivity analysis required for gradient-based approaches, and the reported success of heuristic methods in the reviewed literature.

Furthermore, a multi-objective approach is deemed suitable for this problem owing to the variety of possible performance metrics coming from different spindle behaviors. It will also be shown in upcoming chapters that most performance metrics show non-monotonic behaviors with complex trade-offs, further justifying the need for a multi-objective approach.

The Teaching Learning Based Algorithm (TLBO) was used as the core optimizer. To equip it for handling multi-objective problems, it was augmented by the multi-objective handling scheme in the Non-Dominated Sorting Genetic Algorithm-III (NSGA-III) algorithm.

2.3.1. Teaching Learning Based Optimization

The TLBO method is a metaheuristic optimization algorithm introduced by Rao et. al in 2011 [45] This evolutionary technique takes inspiration from the learning process of students in a classroom environment. The design parameters, fitness values, and population size of the optimization problem are referred to as the students' subjects, test scores, and class, respectively. The algorithm improves class performance in two phases per iteration. In the 'teaching phase', the best performing learner from the class is chosen as the teacher, who then transfers their knowledge to the rest of the class. In the 'learning phase', the students interact with each other to transfer knowledge in-between themselves. This process continues in iterations until the termination criteria is met.

This technique has only two algorithm-specific parameters to tune: class size and number of iterations, which is regarded as one of its strongpoints in terms of ease of use. Moreover, it has been demonstrated to outperform various other algorithms on numerous problems taken from literature [46].

TLBO Initialization

In the initialization phase, the optimization problem is formulated by defining objectives, constraints, and decision variables. The class size, maximum iterations, and termination criterion, if applicable, are also defined as hyperparameters.

A randomized population is generated without parameter bounds and its fitness is evaluated. This initial population then enters the first iteration loop.

Teaching Phase

In each iteration, the teaching phase comes first. The author uses the following index convention for explaining the algorithm:

- *i,* iteration number
- *m,* number of subjects (design parameters)
- *n,* number of learners (population)
- *j,* subject scores (parameter values)

The best learner is first picked as the teacher based on fitness value. Then, the mean subject scores of the entire class, $M_{j,i,}$ are calculated to represent the subject-wise averaged performance of the class. Then, the difference in knowledge between the teacher and students in each subject is calculated using Eq. 2.30.

$$Difference\_Mean = r_i(X_{j,kbest,i} - T_F M_{j,i}) \tag{2.30}$$

Here, $X_{j,kbest,i}$ are the teacher's scores in each subject, r_i is a random number between 0 and 1, and T_F is the teaching factor which is randomly selected as either 1 or 2, , with equal probability between the two. The latter two variables are randomly generated in each loop and determine the amount of knowledge to be transferred from the teacher to students, introducing the characteristic randomness of heuristic algorithms.

Each of the existing solutions is then modified using the results from Eq. 2.30 by Eq. 2.31.

$$X'_{j,k,i} = X_{j,k,i} + Difference\_Mean_{j,k,i} \tag{2.31}$$

Here $X'_{j,k,i}$ are the modified scores which represent the new performance of the students after knowledge transfer with the designated teacher. At this stage, the parameter values are compared against their respective box constraints, if any, and a simple modification is applied using Eq. 2.32. If the calculated value exceeds its limits, it is re-assigned the extreme allowable value:

$$X'_{j,k,i} = \min\left(X'_{j,k,i}, Lower\ Bounds\right)$$
$$X'_{j,k,i} = \max\left(X'_{j,k,i}, Upper\ Bounds\right) \tag{2.32}$$

The updated performance of the students is then compared with their previous performance and if an improvement is seen in the fitness functions, the new solution replaces the original solution.

This procedure is applied to each student during the teaching phase.

Learning Phase

In the learning phase, the students transfer knowledge amongst themselves. A study partner, Q, is randomly chosen for each learner, P, and the learning process between two occurs according to Eq. 2.33.

$$X''_{j,P,i} = X'_{j,P,i} + r_i\left(X'_{j,P,i} - X'_{j,Q,i}\right), \qquad If\ X'_{total-P,i} < X'_{total-Q,i}$$
$$X''_{j,P,i} = X'_{j,P,i} + r_i\left(X'_{j,Q,i} - X'_{j,P,i}\right), \qquad If\ X'_{total-P,i} < X'_{total-Q,i} \tag{2.33}$$

Here $X''_{j,P,i}$ represent the scores of learner P after the learning phase, X'_{total} represent the overall fitness of students after the teaching phase, and r_i is a random number between 0 and 1.

The above formulae are for minimization problems only. Since all problems in this work are exclusively posed in the standard negative null form, the maximization formulae are not discussed.

The same procedure as the teaching phase is adapted for handling box constraints, as shown in Eq. 2.34.

$$X''_{j,k,i} = \min\left(X''_{j,k,i}, Lower\ Bounds\right)$$
$$X''_{j,k,i} = \max\left(X''_{j,k,i}, Upper\ Bounds\right) \tag{2.34}$$

The fitness values for new solutions are evaluated and compared with old solutions, and the better of two is accepted.

It is to note that the interaction among students in the learning phase can be either one-to-one or one-to-all. In the first case, two learners are randomly chosen, and they interact

with each other, while in the latter all students interact with each other. The second approach greatly increases the computational requirement of the algorithm and is thus not chosen in this work.

2.3.2. Multiobjective Optimization

The TLBO procedure explained above is for single objective optimization problems. A separate technique is required to equip it for multiobjective handling. With this additional capability, the optimizer can guide the algorithm towards solutions that improve all objectives simultaneously. Moreover, it also allows the optimizer to identify the 'pareto front, which is a set of non-similar solutions that are all equally optimal, but with varying tradeoffs among the different objectives. This kind of approach is especially useful in engineering design problems, where designers prefer to have numerous optimal design configurations, giving them the freedom of choice.

In his book [46], Rao utilized the Non-Dominated Sorting (NSGA-II) algorithm proposed by Deb et. al [47] to solve multiobjective problems. It is a well-established multiobjective algorithm that works by ranking the entire population into various 'fronts' based on their dominance, favoring higher ranked solutions across all objectives to pass on to subsequent generations. The algorithm also includes the 'crowding distance' calculation, which is a measure of how sparsely located a solution is in the objective space. More sparse solutions are also favored to push the optimization algorithm into unexplored regions.

NSGA-II, however, only works efficiently for up to 2-3 objectives. Since this work is based on problems with a higher number of objectives, the NSGA-II algorithm is deemed insufficient.

Deb et. al [48] introduced the NSGA-III algorithm as an extension to their previous work. In their paper, they provided strong evidence for this method to be compatible with problems having up to 15 objectives (many-objective problems). Therefore, this algorithm will be used in this study.

2.3.2.1. Non-Dominated Sorting III (NSGA-III)

The NSGA-III algorithm is similar in nature to its predecessor in that it ranks solutions and preserves the most unique ones in each population. The mechanism to maintain diversity among pareto solutions, however, was altered to accommodate a higher number of objectives.

Instead of the crowding distance calculation, the solutions in the current population are mapped onto a hyperplane and linked to pre-defined reference points to determine their 'sparsity' in the multidimensional objective space.

A brief step-by-step explanation of its procedure is given below.

1. **Classification of Population into Non-Dominated Fronts**: The current population's fitness is evaluated, and it is divided into various fronts. The most dominant solutions (solutions where none of the objectives can be improved further without worsening at least one other objective) are part of the first front and are the first to enter the next population. If these are not enough to fill the population, the algorithm moves to the second front, and so on. When filling the last available slots in the next population from the current population, there is a need for a selection criterion to pick the most suitable candidates from the active non-dominated front. These candidates are the most sparse, non-dominated ones in the remaining population. The following steps explain this sparse selection method.
2. **Determination of Reference Points on a Hyper-Plane:** The user defines the number of objectives and number of divisions, Z, at the start. A hyper-plane is created with an intersect of 1 on all axes (equal to the number of objectives) and Z divisions in between 0 and 1. This generates several reference points on this hyper-plane.
3. **Adaptive Normalization of Population Members:** The entire population is normalized by taking the most extreme points of each objective's fitness values as reference. The points can then be mapped in the objective space.
4. **Association with Reference Points:** The normalized solutions are then assigned to the reference points on the hyper-plane. Each solution is then assigned to the closest reference point on the hyperplane, with the cartesian distance serving as

the criteria for closeness. Ideally, the Z value should be selected in a way that the hyperplane has slightly more reference points than the population size. This helps ensure that the sparsity of sparse solutions is captured as distinct reference points on the hyperplane.

5. **Niche-Preserving Operation:** This is an important step in selecting appropriate members from a front for including in the next population. If the entire front cannot be transferred to the next population, a limited number of members from it must be chosen selectively. In such a case, the reference points with the least number of members associated with them are chosen and the closest one is allowed into the next population. This niche-preserving procedure adds diversity to the population.

Constraint Handling

The TLBO algorithm does not have an inherent method to handle constraints. As with most multiobjective evolutionary algorithms, it handles constraints in its selection and sorting scheme. Deb et. al [49] introduced the constrained optimization version of NSGA-III, which is used in this study.

The non-dominated sorting mechanism is replaced by the constraint-domination principle, which is:

Solution A constraint-dominates solution B if any of the following condition holds:

a) A is feasible and B is infeasible
b) A and B are infeasible, but A has a smaller constraint violation than B
c) A and B are feasible, but A dominates B

The Constraint Violation, *CV*, for a particular solution is calculated by adding the normalized violation for all constraints. The higher the *CV* value, the more infeasible the point is considered.

The sorting and selection mechanisms are different for feasible and infeasible population members. When filling up the next generation, the algorithm first favors feasible solutions and operates on them via the same principles of non-dominated sorting and niche-

preserving as described above. In case the feasible solutions are not enough to fill up the next generation, the infeasible solutions with the least *CV* are favored.

Developed MO-TLBO Algorithm

A hybrid algorithm for TLBO and NSGA-III was developed in *MATLAB* using the two theories explained above. The external archive approach adopted by Zhou et. al [50]was utilized to preserve the best solutions produced in the optimization at any point. In this method, an external repository is maintained and updated at all iterations to store the best non-dominated/niche solutions so far. Moreover, the teacher selection for each iteration is also performed from solutions within this repository, based on their non-dominance rank and uniqueness.

Moreover, advantage is also taken of the Opposition-Based Learning scheme proposed by Tizhoosh [51]. In this scheme, the 'mathematical opposite' of each population member is computed as shown in Eq. 2.35 and a combined populated is obtained. A selection scheme (Non-Dominated Sorting + Niche-Preserving) is then utilized to select the best solutions from this population. In this study, this method is only applied to the initial population to orient the iterative part of the algorithm towards more feasible solutions.

$$x_{opposite} = x_{max} - (x - x_{min}) \tag{2.35}$$

To develop the code for this hybrid algorithm, the open-source NSGA-III code by [52] was used as a reference.

The working of this hybrid algorithm is illustrated in the flowchart in Figure 7 below.

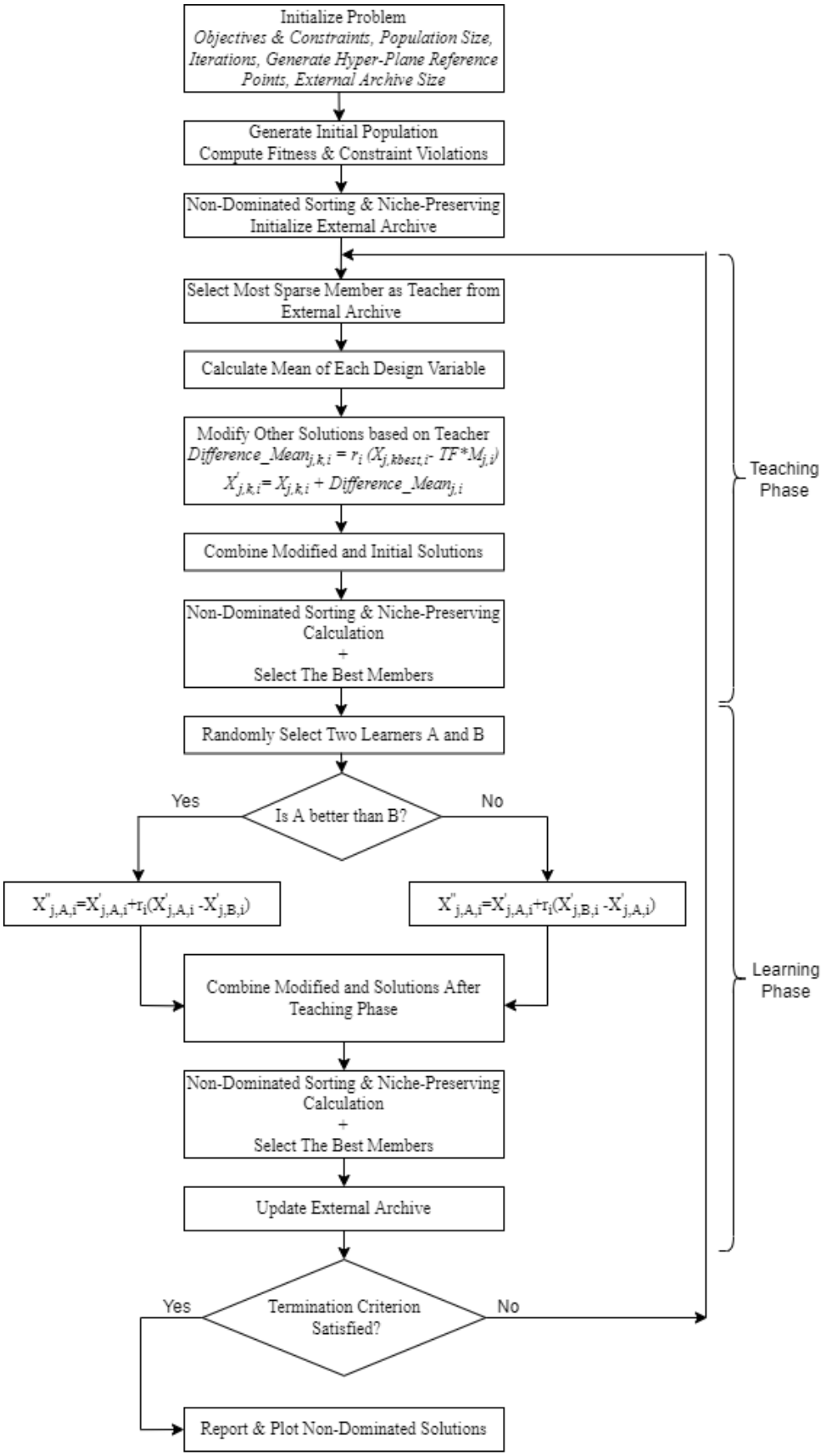

Figure 7: Flowchart of multiobjective optimization scheme

Since the code for this hybrid algorithm was written by the author, there was a need for it to be tested. To check the accuracy of the developed code, it was tested with the well-known Zitzler–Deb–Thiele (ZDT) optimization functions [53], which are a group of benchmark problems to test evolutionary optimization algorithms. The obtained results were comparable with the respective true pareto fronts. Figure 8 shows the performance of the code on the different tested problems in the ZDT suite.

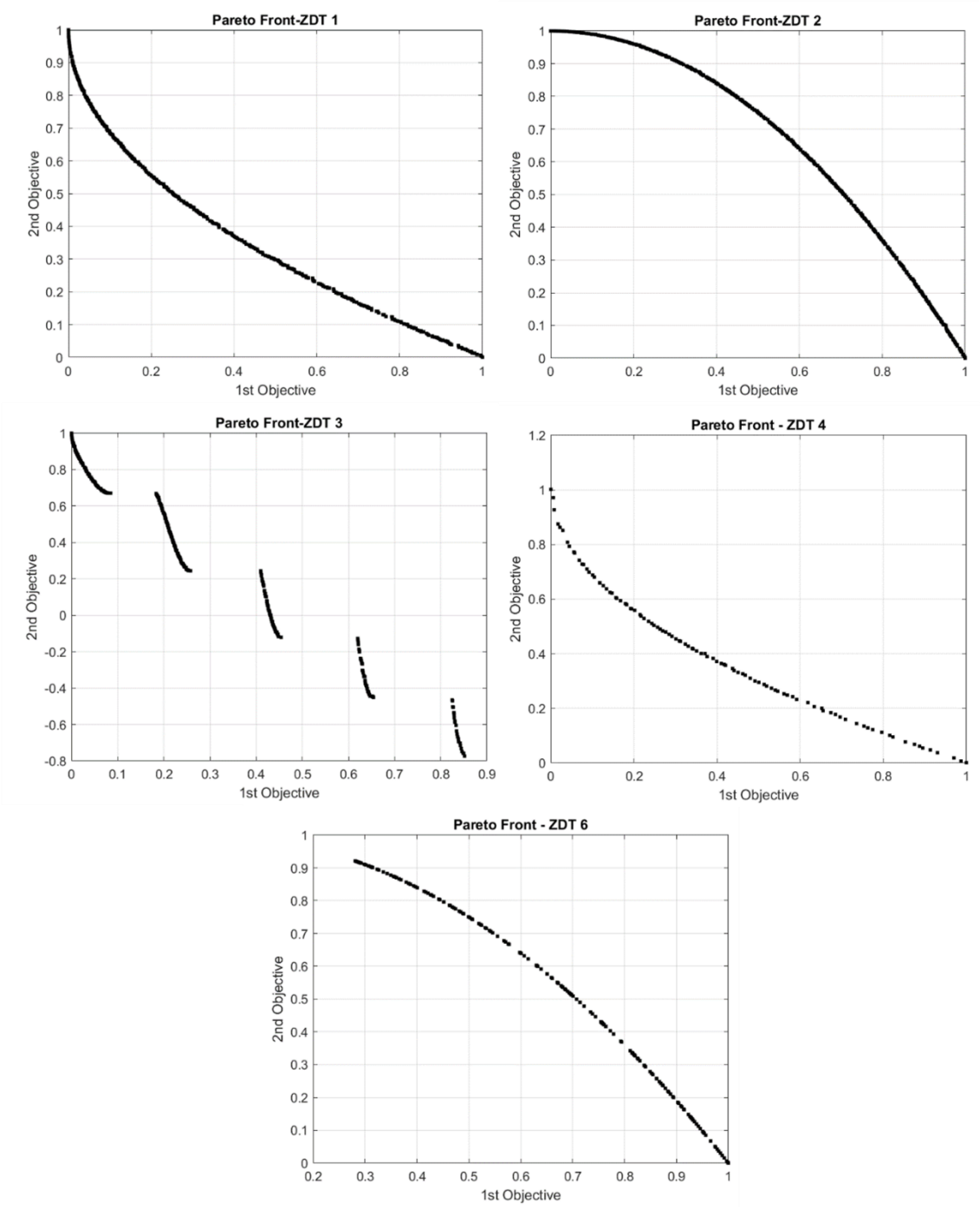

Figure 8: Verification results of multiobjective optimization code

2.4. Summary

A detailed theoretical background was provided on the analytical models used in this work. For spindle dynamic modeling, the bearing stiffness calculation method and the RCSA technique were discussed. Practical considerations like bearing configurations were also covered.

The FE approach for thermal modeling of our spindle design was presented. The appropriate calculations for computing heat transfer characteristics at the identified heat sources and sinks were explained. The meta-modeling technique for this FE model was also discussed.

In the last section, the theory and verification of the multiobjective optimization scheme developed for this thesis was discussed. It combines the TLBO algorithm with the NSGA-III technique.

3. MULTI-OBJECTIVE OPTIMIZATION OF HIGH-SPEED SPINDLE

A comprehensive optimization procedure was adapted in this study to improve different performance aspects of the high-speed spindle. The main goal was to fully utilize the developed optimization methodology in a holistic way, and thus, explore the maximum number of avenues for design improvement and exploit the ones with the highest potential.

It is important to share that this optimization effort ran parallel to the actual design and manufacturing process of our spindle, as well as the development of the various spindle models utilized in this study. Working in this scenario presented both unique opportunities as well as certain drawbacks.

The main positive was that the author had the opportunity to participate in the entire design process from beginning to end. This allowed better control over almost all spindle design parameters. This is rarely the case in academic studies, where the researchers are restricted to working with a pre-designed spindle with only a limited number of alterable attributes.

The challenges were equally profound. The main challenge was the constantly evolving state of the spindle design as our project progressed. While this was beneficial as results from each stage guided the process in subsequent stages, this was also not always the case due to practical reasons like manufacturing constraints and the research group's growing knowledge of the subject.

Consequently, this optimization study was largely guided by the spindle design process. A stepwise optimization strategy was adapted that started with a large, unexplored design space that eventually funneled down to a few design propositions. At each step, the

optimization problem was formulated based on the prevalent state of the design and known practical limitations.

Therefore, this chapter presents the optimization effort in four stages. At each stage, a short summary of the current design and practicalities is provided along with details of the findings.

However, before the actual optimization study can be explained, a short discussion on some of the preliminary decision-making is necessary to contextualize the work explained in upcoming sections.

3.1. Preliminary Design-Guided Decisions

The number of potentially optimizable design variables in high-speed spindles is very high. Since this work followed the design of a high-speed spindle from scratch, the entire pool of optimization variables was open for investigation.

However, some initial decisions were quite straightforward and were made on practical grounds without a formal optimization approach. The decision-making at this stage was guided by reference spindle designs from our research project collaborators, industry standards, and the core specification of designing a 40,000 RPM spindle.

These initial design-guided decisions and their respective rationales are enlisted below:

- **Angular contact ball bearings:** The choice of bearing types was a straightforward decision. Angular contact ball bearings are widely used in machine tool spindles as they are suitable for both axial and radial loads and offer a tradeoff between rigidity and thermal stability with varying preloads.
- **Back-to-back bearing configuration:** ACBBs can be mounted on the shaft in various configurations, depending on the orientation of individual bearings with respect to the shaft. Generally, the choice for spindle designs is between the back-to-back (O-configuration) and face-to-face (X-configuration) options. The back-

to-back configuration was preferred owing to its higher rigidity and thermal stability at high speeds.

- **Constant preload mechanism:** Preload can be applied to spindles in different ways. The constant preload mechanism was chosen as it prevents bearing preload from increasing at high speed due to thermal expansions. This simplified the dynamic analysis as well since thermally induced preloads were omitted from the modelling.
- **Motorized spindle:** A built-in motor on the shaft is a common design feature for high-speed spindles. It ensures even power delivery to the shaft instead of methods like belt drives, which induce force imbalance into the structure. It is significant in this study as the mass of the motor's mounting sleeve and rotor affect the spindle-tip dynamics, restrict the bearing span by taking up space in the middle of the shaft, and generate extensive heat during operation.
- **Cooling system:** The general layout of the spindle cooling system was also decided in the beginning. The design features water cooling channels in the vicinity of the motor and bearings, and a constant flow of air in the motor chamber housing the rotor and the stator. These effects were considered when conducting thermal analysis.

The finalization of these design features narrowed down the design space for optimization by fixing a basic configuration for the spindle.

In addition to these details, it is also important to share that the focus of the optimization efforts was primarily on thermal and dynamic behaviors as these have been identified to be the most conflicting characteristics. To illustrate this conflict in a simplistic manner, the behavior of angular contact ball bearings is discussed below. Figure 9(a) and (b) represent the change in different bearing stiffness terms from Eq. 2.8 with respect to the axial preload. Figure 9(c) shows the variation of maximum bearing temperature for different preloads across a wide speed range [54]. These trends are universal for all bearings, regardless of bearing specifications. It can be inferred from these figures that both stiffness and bearing temperature rise with preload. From a practical point of view, higher stiffness and lower temperatures are desired. Thus, there is a tradeoff between stiffness (a dynamic property) and temperature (a thermal property) with respect to the preload, which must be carefully selected to balance both behaviors. This tradeoff is

observed in various spindle design parameters in addition to bearing preloads, and the following sections will discuss the efforts to identify and optimize these parameters.

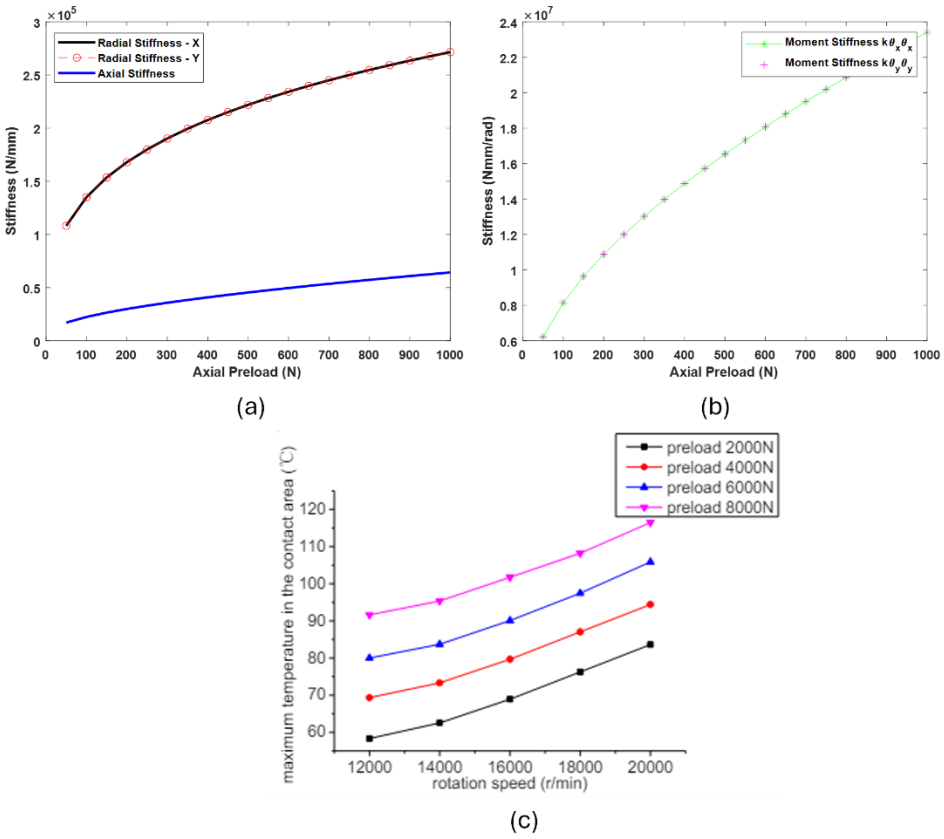

Figure 9: Dynamic and thermal characteristics of bearings [54]

3.2. Stage 1: Exploratory Sensitivity Analysis

The first step in this study was to identify sensitive design variables that showed a strong potential to improve spindle behaviors. This was done by mapping the results of varying each design variable across a range while keeping all other parameters fixed. The range in which the parameter is varied is defined around a nominal value while keeping practical limitations and general design intuition in mind. Parameters that caused large variations in spindle behaviors were considered sensitive.

These identified sensitive variables are suitable to include in the optimization scheme while non-sensitive variables can be safely eliminated from the pool of candidate variables.

3.2.1. Current Status of Project

At this initial stage of the project, the spindle design had not begun. Therefore, the geometry of a reference spindle model provided by our research collaborator was used for conducting sensitivity analysis. The relevant details of this reference model are given in Table 1. The front bearings and rear bearings were mounted on section 6 and 8, and 15 and 17, respectively.

In Table 2, the bearing stiffnesses and damping values used in the simulations are shared. Dummy values shared by our collaborator were used at this stage. Only translational stiffness and damping terms were used for simplicity. It is understood that adding the rotational and cross-stiffness terms changes the FRF, but limited data was available at this point. Moreover, the identified trends were later verified with the complete stiffness matrix and found to be roughly the same.

Segment	Length (mm)	Inner Diameter (mm)	Outer Diameter (mm)
1	*12.5*	*30*	*25*
2	*12.5*	*30*	*22*
3	*6*	*30*	*18*
4	*14.5*	*32*	*0*
5	*20*	*61.5*	*0*
6	*16*	*45*	*0*
7	*16*	*55*	*0*
8	*16*	*45*	*0*
9	*5*	*45*	*0*
10	*7*	*51*	*0*
11	*15.8*	*41.5*	*0*
12	*98.4*	*26*	*0*
13	*21*	*41.5*	*0*
14	*15*	*37*	*0*
15	*13*	*30*	*0*
16	*9*	*40*	*0*
17	*13*	*30*	*0*
18	*12.8*	*30*	*8*

Table 1: Spindle dimensions

	Translational Stiffness (N/.m)	Translational damping coefficient (N.s/m)
Front Bearings	*1.35e7*	*200*
Rear bearings	*3.5e7*	*50*

Table 2: Bearing stiffness and damping values

Since the main goal at this point was to begin designing a basic structure, the focus was on investigating the effects of main geometric dimensions and bearings. With this in mind, the following list of parameters were chosen for sensitivity analysis:

- Bearing Stiffnesses
- Bearing Locations
- Tail Length
- Inner Diameter
- Bearing Configuration

Moreover, at this stage, the effects of these parameters on only the spindle-tip FRF were checked. Thermal analysis was not included as its main behavior was already known (more bearing preload, more heat generation and thermal growth), the status of the work was still premature, and the specifics of the cooling system were also unfinalized.

3.2.2. Bearing Stiffness

The bearings are the main stiffness-inducing components in spindle structures. To check their effects on spindle-tip FRF, the methodology followed by Ertürk et al [15] is adapted. The bearing stiffness values were first doubled, then halved, and the FRFs were compared. This process was repeated three times, once each for the front bearings, rear bearings, and both bearing sets.

The results are shown in Figure 10 and Figure 11. There is a clear observation that using stiffer bearings results in a more rigid structure with higher natural frequencies. In terms of peak modal amplitudes, which represent the maximum vibration amplitudes at modal frequencies, the effect of bearing stiffnesses is also significant. For stiffer bearing sets, the results show a compromise between peak amplitudes of the first and second modes. While the second mode appears to be more stable, the first mode's peak amplitude is higher for stiffer bearings.

Figure 11 shows the individual effects of each bearing set on the spindle-tip FRF. A comparison with Figure 10 points towards evidence that the front bearing set primarily influences the first mode while the rear bearings only effect the second mode. These observations are consistent with those of Ertürk et al [15]. It is also evident that front

bearings have a larger share of the overall influence of bearing stiffnesses on spindle dynamics.

Thus, from a dynamics point of view, it is always favorable to have higher preloads. Moreover, the decision of bearing preloads should carry more weight from the front bearing set.

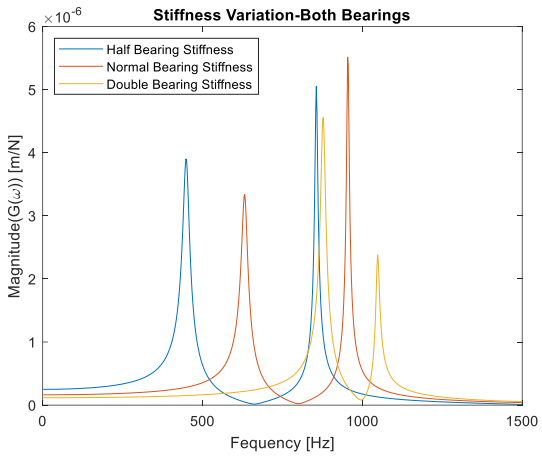

Figure 10: Bearing Stiffness Sensitivity-Both Bearing Sets

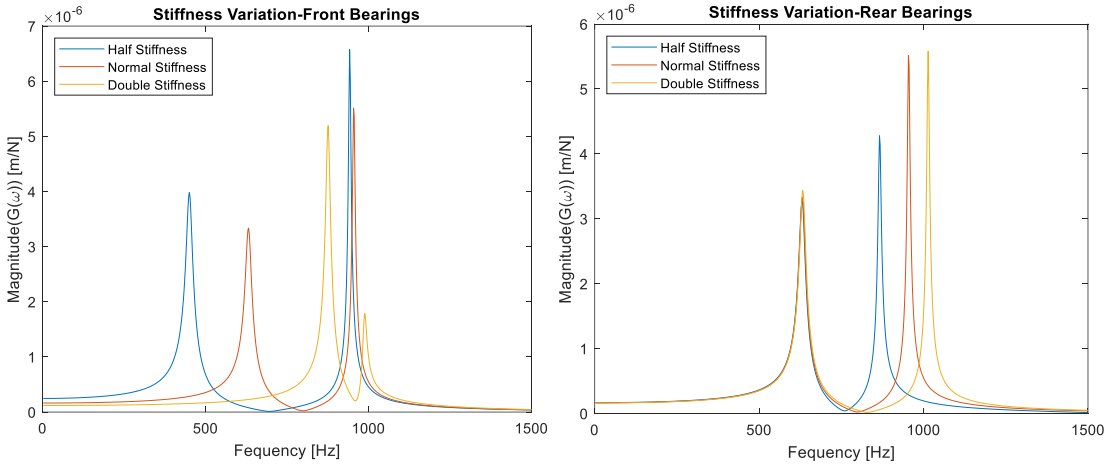

Figure 11: Bearing Stiffness Sensitivity-Front & Rear Bearing Sets

3.2.3. Bearing Locations

Bearing locations play a critical role in spindle dynamics and rigidity. To check their sensitivities, the segments *L1* and *L2* in the schematic in Figure 12 were varied by +5mm

and -5mm. It is pertinent to mention here that only *L1* and *L2* were changed for each analysis, that is, the shaft length changed slightly for each simulation. It was pre-verified that this slight change in shaft length does not have any discernible influence on the structure.

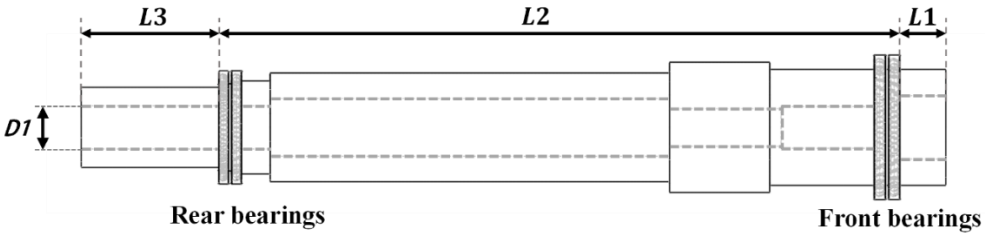

Figure 12: Schematic for bearing locations and shaft hole

Figure 13 has two key observations. The spindle performance is best in terms of modal frequencies when the front bearings are closer to the spindle tip. With regards to the peak modal amplitudes, a conflicting trend between first and second modes was observed. Moving the front bearing set closer to the spindle tip had a positive effect on the first mode but the opposite effect on the second mode.

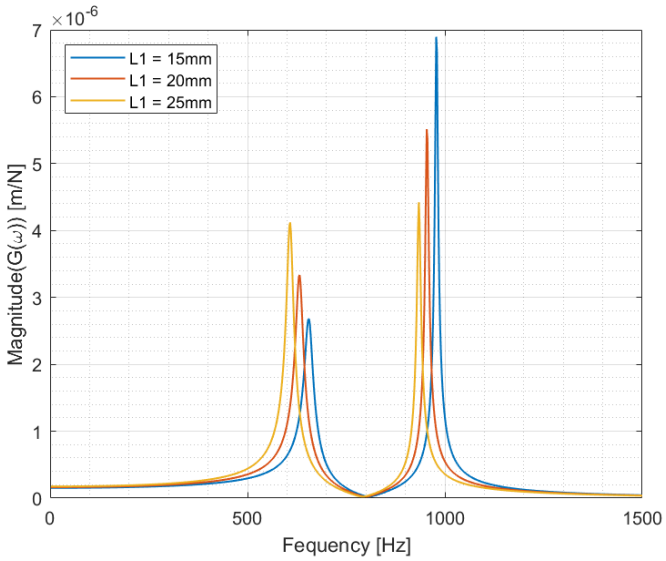

Figure 13: Sensitivity of Front Bearing Set Location

This conflicting trend indicates that any alteration in front bearing location can adversely impact the vibration response of at least one of the first two modes. This compromise makes it clear that front bearing location is to serve as an important decision variable in the dynamic optimization scheme.

Figure 14 corroborates key evidence obtained in the bearing stiffness variation comparisons for the rear bearing set. The rear bearing location (*L2*) solely affected the peak modal amplitude and modal frequency of the second mode. This analysis indicates positive effects of locating the rear bearing closer to the spindle tip in terms of both peak modal amplitudes and modal frequencies. Thus, the absence of a trade-off shows that the rear bearing set should be placed as close as possible to the spindle tip. In other words, the spindle shaft should be designed short by keeping the bearing span minimum.

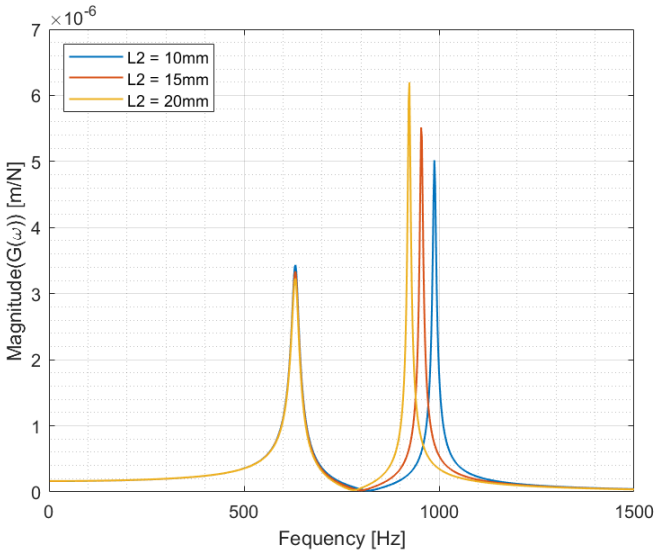

Figure 14: Sensitivity of Rear Bearing Set Location.

3.2.4. Tail Length

The tail portion of the spindle shaft (*L3* in Figure 12) is a point of interest in literature due to its potential application as a dynamic absorber [30]. A dynamic absorber can be described as an auxiliary inertial system that is custom designed to match its natural frequency with that of a main inertial system. When integrated into the structure of the main system, it can dampen the vibration response of the main system at its resonant frequencies. Thereby creating a positive impact on its dynamic performance.

On an FRF plot, this appears as the dominant FRF peak being split into two peaks of lesser magnitudes.

In a shaft-bearing system, the middle section of the shaft held between the bearing sets (*L2*) acts as the main system, while the tail (*L3*) and the front (*L1*) sections act as auxiliary inertial systems that can alter the dynamic response of the shaft. Moreso, they can also serve as dynamic absorbers if designed correctly.

Both these avenues have been actively explored in literature. Changing the front section with toolholder extensions and tool length tuning is a common topic of interest for positively altering tooltip FRF in different studies [55]. However, their application as perfect dynamic absorbers are limited since the geometry of such extensions is restricted by physical constraints by the machine tool's machining volume and concerns regarding tool vibrations and life. Moreover, investigating the front section was also beyond the scope of this spindle design project.

Since some studies have already investigated the effects of changing the tail length to achieve the dynamic absorber effect, and taking advantage of the design freedom, the tail length was included in the sensitivity analysis.

The sensitivity check of the tail length was initially performed by introducing small variations of 5mm. However, these failed to yield discernible results, indicating that small changes in the tail length are insignificant in terms of dynamics and rigidity.

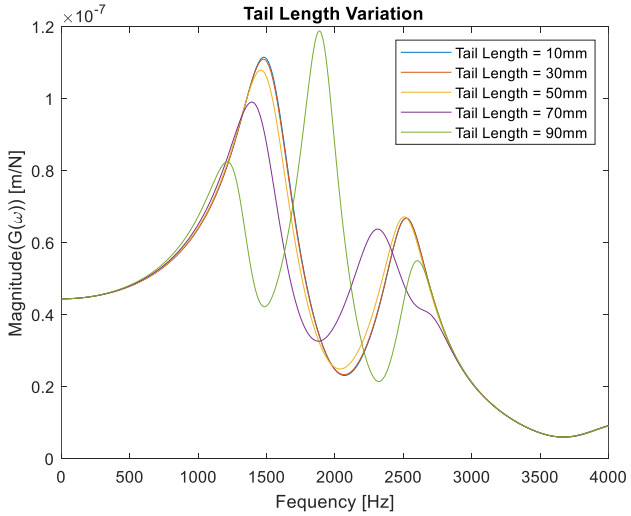

Figure 15: Sensitivity of Tail Length

Figure 15 shows various simulations run for larger variations of 20mm in the tail length. Five simulations were run for 10, 30, 50, 70, and 90 mm tail lengths. The results may be split into two phases: below 50 mm and above 50 mm. For tail lengths shorter than 50mm,

it is observed that the spindle dynamics show no significant change. After 50 mm, the second mode suddenly shows a remarkable change in both peak amplitude and frequency due to its interaction with a new, third mode that appears close to it on the frequency spectrum. This shows that the sensitivity of auxiliary dimensions like the tail length is variable, exhibiting large, and rather abrupt, results at certain values, and a relatively soft response at other values.

Since there is no experimental verification for this found in the literature, a simple shaft-bearing system was designed with variable tail length and middle section diameter, as shown in Figure 16.

Figure 16: Experimental setup for tail length sensitivity analysis

The shaft is mounted on two angular contact ball bearings in back-to-back configuration, as in our design. In the first set of experiments, the tail length is varied by adding weights of 15mm length to the back of the shaft. In the second set, the same tail length variation is applied but with a uniform mass attached to the middle section of the shaft, increasing its diameter from 40mm to 50mm. The results in Figure 17 clearly indicate that both parameters produce significant variations in the FRF, rendering it a strong candidate for optimization.

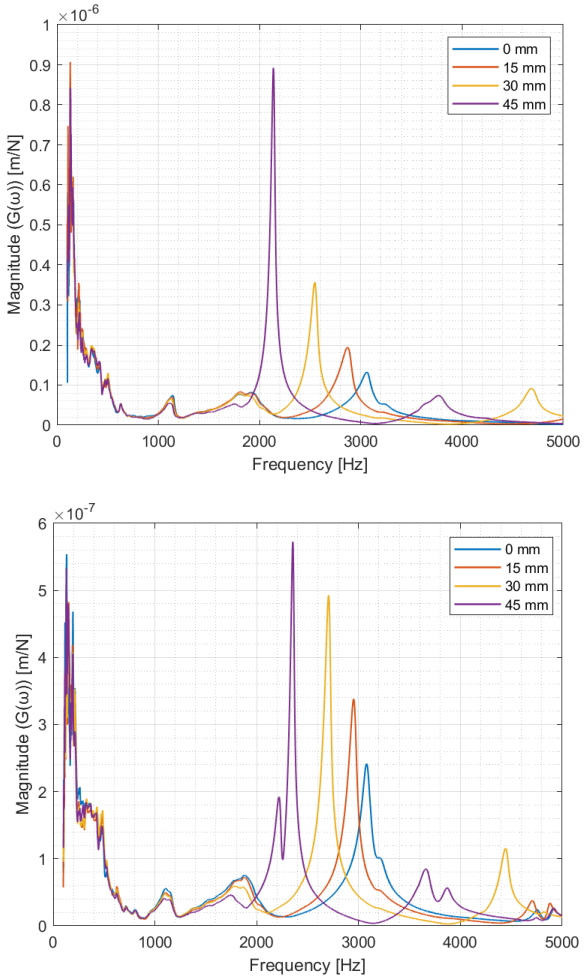

Figure 17: Experimental FRF plots for changing tail length

3.2.5. Shaft Hole Diameter

The effect of the shaft's inner hole diameter on the spindle-tip FRF was also investigated. Machine tool researchers have reported the positive effects of hollow cutting tools on the tooltip stiffness [56], [57], [58]. Thus, it is reasoned that the inner diameter of a hollow spindle shaft can also be a sensitive parameter. Figure 18 shows that increasing the inner diameter (*D1* in Figure 12) made the shaft more rigid by shifting the natural frequencies of both modes to higher frequencies. The peak modal amplitudes also showed a net positive impact as the first mode remained almost constant while the second mode showed considerable improvement.

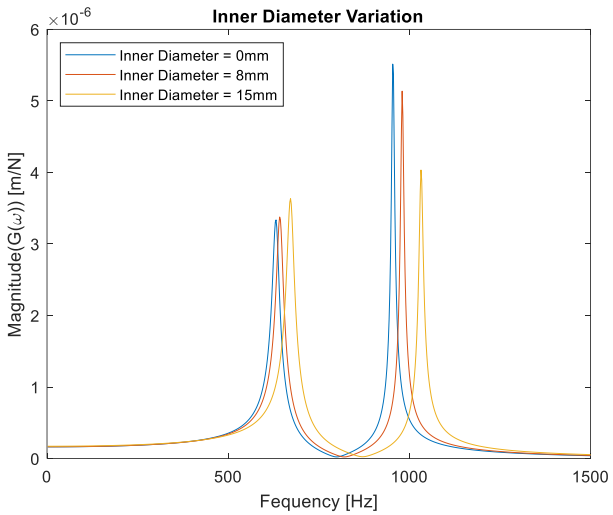

Figure 18: Sensitivity of Inner Diameter

Since the observation of a larger hole increasing the dynamic stiffness of a shaft is slightly counterintuitive, a cross-verification was performed using an FE-based modal analysis. A fairly slender beam of 500 mm length and 50 mm outer diameter was chosen for this to capture the behavior of several modes in a low-frequency window. As only the behavior of beam dimensions is desired, the modal analysis was conducted with free-free boundary conditions. Figure 19 shows the variation of several modal frequencies for different hole diameters, obtained through a 2D FE analysis in *ANSYS 21*. The first three modal frequencies showed an improvement as the hole diameter increased from 0 mm to 25 mm, verifying the aforementioned observations. However, high-frequency modes showed the opposite trend, where a larger hole diameter caused the modal frequencies to decrease, indicating a decline in stiffness. The 7^{th} mode is used to show this in Figure 19(b), which decreased by 437 Hz for a hole diameter of 25 mm hole compared to no hole. Therefore, it is observed that at some high-frequency mode, the effects of hole diameter shift from being positive to negative. However, the frequency range where this occurs is generally too high, even for slender, flexible beams. For example, the 7^{th} mode in the discussed case is at around 15,000 Hz, which is much higher than the frequency range of interest for machine tool applications. Therefore, the results in Figure 18 are reliable. These results were also confirmed to be nearly identical with the Timoshenko beam analysis method utilized in the in-house RCSA code.

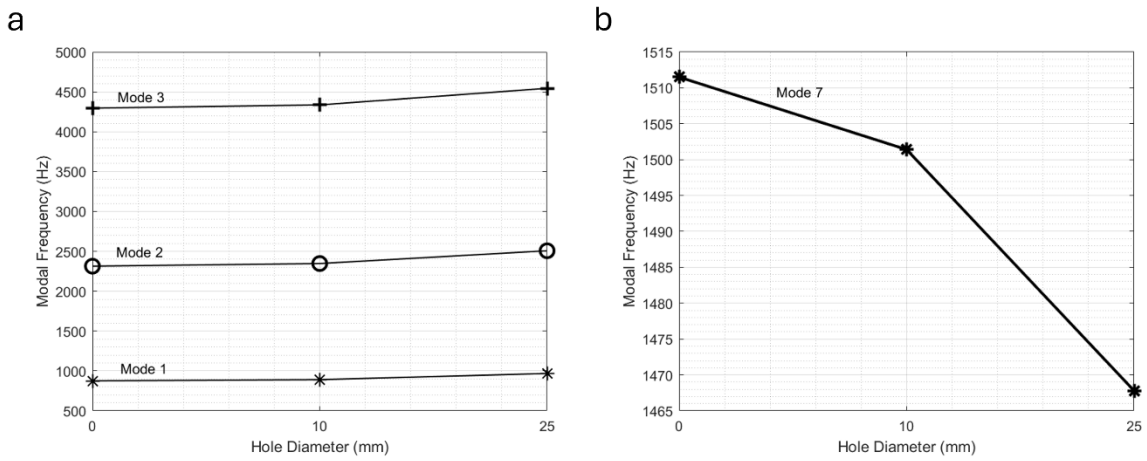

Figure 19: (a) Modal frequency variations for different hole diameters for modes 1-3, (b) Modal frequency variation for mode 7.

While the inner diameter of the spindle shaft is a sensitive parameter as shown, it may not be very flexible due to its small range and its negative impact on shaft strength when enlarged. Moreover, in an actual spindle, the shaft also houses auxiliary components like the drawbar at its center, limiting the variability of its hole diameter.

However, since at this point the dimensions of the inner hole in the shaft were undecided and its impact on spindle dynamics was exclusively positive, it was carried on as a design variable into the subsequent optimization stage. Moreover, shaft cooling was also considered by our team, which requires the drilling of cooling channels in the shaft.

3.3. Stage 2: Optimization of Shaft-Bearing System

The sensitivity analysis in the previous section was fundamental in identifying important design parameters and mapping their effects on spindle dynamics. In this section, the basic optimization approach on the initial spindle design is presented.

3.3.1. Current State of Project

At this stage of this project, some basic design decisions regarding the geometric layout of the spindle were finalized. Moreover, some off-the-shelf components had been selected as well. A summary of these activities is as follows:

- There was a clear idea regarding the general dimensions of the shaft. The bore sizes of the front and rear bearing sets dictated the diameters of the front and rear portions of the shaft. The size of the driving motor gave an idea about the middle section's length and diameter. The range for the total length of the shaft was also somewhat known based on the number of auxiliary components mounted on the shaft.
- The bearings had been selected from the SKF super-precision bearing series. These bearings are suitable for high-speed machine tool spindle applications. Table 3 provides a summary of their major specifications required for computing their stiffness matrices.
- Details of the other auxiliary components on the shaft and peripheral systems were not finalized yet. Therefore, in this section, the optimization problem is built around a simple 'shaft-bearing system' only.
- In this shaft-bearing system, some of the dimensions were fixed based on selected components. For example, the width of the spacers in each bearing set was considered equal to the bearing width, as guided by the bearing manufacturer. A drawbar was planned to be installed inside the shaft. A 20 mm diameter through hole was included in the geometry to represent this. Moreover, the total length of the shaft was kept constant at 350 mm.

Specification	Front Bearing	Rear Bearing
Bore Diameter (mm)	*45*	*35*
Outer Diameter (mm)	*68*	*55*
Width (mm)	*12*	*10*
Ball Diameter (mm)	*6.35*	*5.556*
Number of Balls	*21*	*19*
Contact Angle (Degrees)	15^o	15^o
Inner Race Curvature Ratio	*0.5355*	*0.5355*
Outer Race Curvature Ratio	*0.5255*	*0.5255*
Ball Material	*Bearing Steel*	*Bearing Steel*

Table 3: SKF bearing specifications

3.3.2. Optimization Problem

A multi-objective optimization problem was formulated as shown Eq. 3.1 using the design variables indicated in Figure 20.

$$
\begin{aligned}
&\textit{Min} \quad J(1): \max(|\boldsymbol{R_{11}}|_1) \,/\, \max(|\boldsymbol{R_{11}}|_1)_{nom} \\
&\textit{Min} \quad J(2): 1/(\boldsymbol{\omega_1/\omega_{1,nom}}) \\
&\textit{Min} \quad J(3): \max(|\boldsymbol{R_{11}}|_2) \,/\, \max(|\boldsymbol{R_{11}}|_2)_{nom} \\
&\textit{Min} \quad J(4): 1/(\boldsymbol{\omega_2/\omega_{2,nom}}) \\
&\textit{Min} \quad J(5): \delta_{running} \,/\, \delta_{running,nominal} \\
&\\
&\textit{s.t} \quad 10 < X(1): L\_Front < 30 \\
&\qquad 150 < X(2): L\_Mid < 250 \\
&\qquad 50 < X(3): Front\ Preload < 200 \\
&\qquad 40 < X(4): Rear\ Preload < 150
\end{aligned}
\tag{3.1}
$$

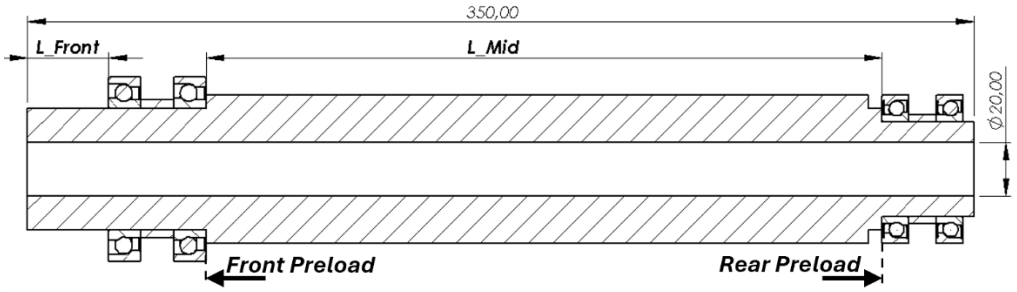

Figure 20: Schematic for optimization stage 2

Here, the matrix *J* represents the five objective functions. *J(1)* and *J(3)* are the FRF amplitudes of the two most dominant modes. Similarly, *J(2)* and *J(4)* are the reciprocals of the natural frequencies for these two modes. Reciprocals are taken as objectives are formulated for a minimization problem. A visual representation of these four objectives on a sample FRF are shown in Figure 21.

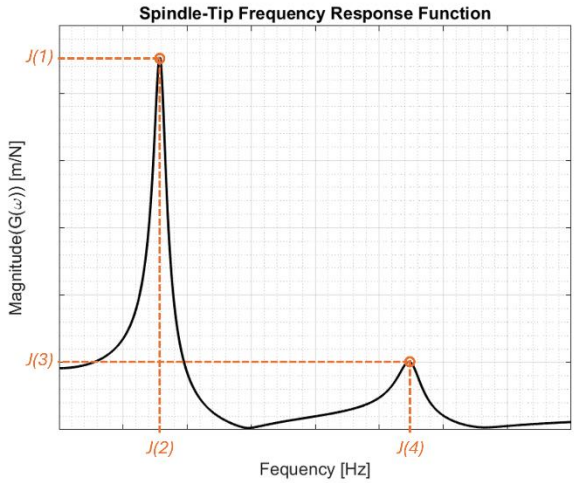

Figure 21: Objective functions for Eq. 3.1

J(5) is the sum of the running torques of all four bearings. The calculation is performed using an empirical model published by NSK [59]. Figure 22 shows the variation of running torque for both bearings. This objective function serves the important purpose of adding a thermal constraint to the problem, which would otherwise most likely converge to higher bearing preloads for the best dynamic properties. Running torque, which should ideally be as minimal as possible for lesser heat generation and power consumption, increases monotonically with bearing preloads. Thus, it pushes the optimization algorithm to identify bearing preloads that maximize dynamic characteristics while avoiding excessive thermal loads.

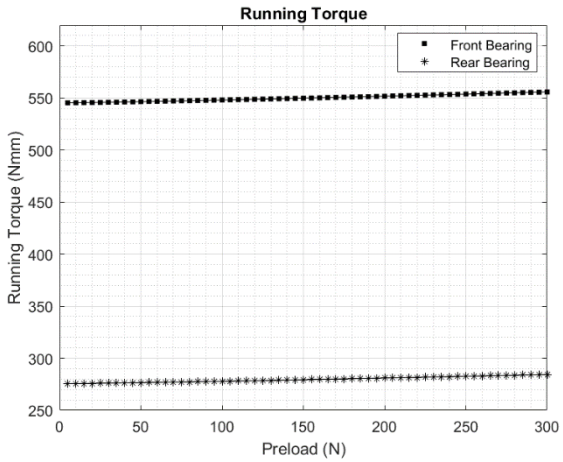

Figure 22: Bearing running torque vs preload

The matrix *X* comprises the four design variables, as Figure 20 illustrates. *X(1):L_Front* is the distance of the front bearing set to the spindle tip, *X(2):L_Mid* is the bearing span, and *X(3): Front Preload* and *X(4): Rear Preload* the preloads of the front and rear bearing sets, respectively. The bearing preload ranges are taken as the lowest two preload classes from the bearing catalogue.

Since there was no nominal design to serve as a reference for improvement at this stage, the nominal values in Table 4 were arbitrarily chosen from the defined box constraints. Moreover, all five objectives were normalized against their nominal values shared in Table 4.

L_Front (mm)	**L_Mid (mm)**	**Front Preload (N)**	**Rear Preload (N)**
30	*250*	*50*	*40*

Table 4: Nominal values for stage 2 optimization problem

3.3.3. Optimization Results

The optimizer was run with a population size of 25, an external archive of 50, and for 20 iterations. The algorithm showed strong convergence towards a pareto optimal solution

set. Figure 23 shows the value of each decision variable for the entire population of 25 members.

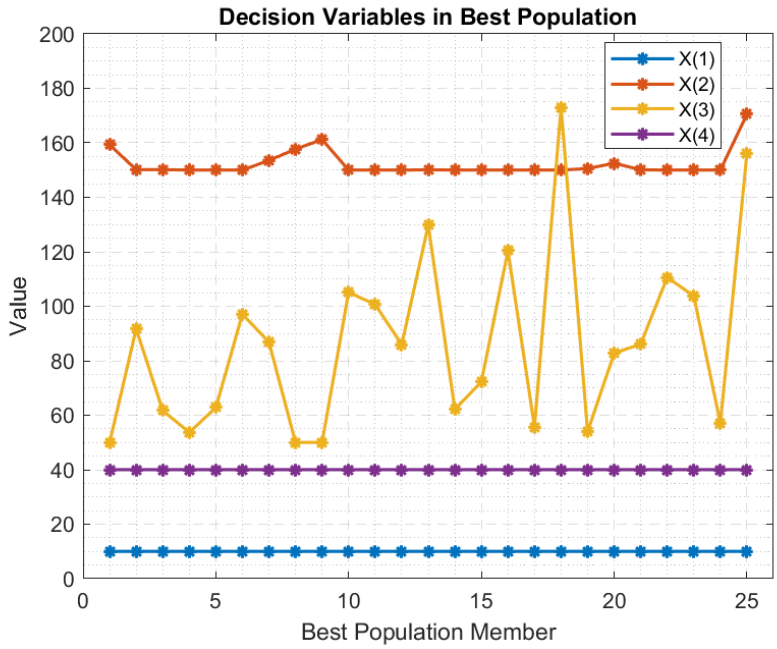

Figure 23: Optimal decision variables for stage 2 optimization problem

It is clear that certain parameters exhibit a monotonic relationship with respect to the objectives due to their strict convergence to specific values. *L_Front* was 10mm for the whole population, showing that the front bearing set should be as close as possible to the spindle tip. Similarly, *L_mid* also varied slightly close to its minimum value of 150mm, indicating that the bearing span should also ideally be as small as possible. These results confirm the observations presented in the sensitivity analysis in stage 1.

The preload values in the final population showed variations. A trade-off was expected between the dynamic and thermal objectives with respect to the bearing preloads. While this tradeoff did exist (Figure 23), it was only caused by the front bearing preload, which varied across a wide range. The rear bearing preload also converged to its lowest value of 40N.

This result is slightly unexpected as higher preload is better for rigidity and the tradeoff should be a result of both bearings. However, the following reasoning may justify this behavior. Firstly, it was concluded in the sensitivity analysis that rear bearings have a smaller impact on spindle performance. These results are a manifestation of this observation. Moreover, in this case, the rear bearings are smaller than the front bearings

and have lower preloads. This means that they have a bigger impact on spindle rigidity and total running torque. Hence, the front bearing preload values may have dominated the movement of the optimization algorithm.

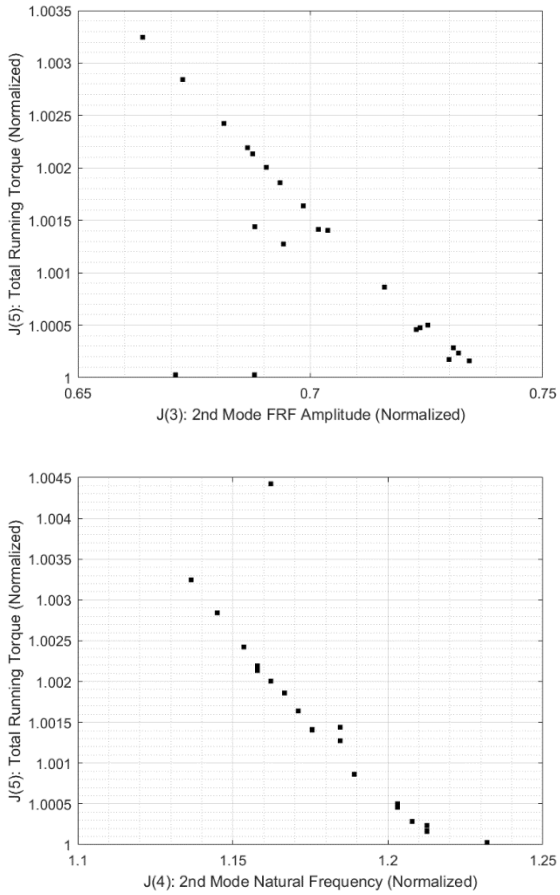

Figure 24: Selected pareto fronts for stage 2 optimization problem

Figure 24 shows the pareto front generated by selected objective functions. Since five objectives are difficult to represent, a 2D representation is used. While a crystal clear pareto front would have been ideal, a general trend is still clearly visible between the objective function values. A few outliers are also part of the solution set, but they were confirmed to be irrelevant from a practical design point of view.

The second FRF mode showed larger variations, so it was chosen to represent the tradeoff between dynamic (modal amplitudes and natural frequencies) and thermal (running torque) indicators. Therefore, it is confirmed that from the four design variables, the front bearing preload can be used to find the optimal balance between dynamic and thermal characteristics.

Finally, two solutions are chosen from the best population (solutions #18 and #25) to illustrate the effectiveness of the developed optimization scheme. Figure 25 and Table 5 show the FRF's of these two solutions and the optimized variables in comparison to the nominal values. Significant improvements were noticed in the modal amplitudes for both modes. The first natural frequency also showed a strong improvement for one of the selected solutions and stayed almost unchanged for the second one. The second natural frequency, however, decreased for both solutions. While this is an undesirable effect, it does not carry much practical weight as modal amplitudes have decreased significantly. Moreover, the shift in the modal frequencies has brought both modes closer to each other, causing their dominant vibration response to act in the same frequency zone. Thus, the previous design with two distinct, dominant modes is changed to a design with roughly a single dominant mode in approximately the same frequency range. The running torque values are slightly higher for both optimal cases. This is expected since the minimum preload values are selected as the nominal values for bearing preloads. Thus, any solution would yield higher total running torque.

	X(1)	**X(2)**	**X(3)**	**X(4)**	**max($\|R_{11}\|_1$) (µm/N)**	**ω_1 (Hz)**	**max($\|R_{11}\|_2$) (µm/N)**	**ω_2 (Hz)**	**$\delta_{running}$ (Nm)**
Nominal Solution	*30*	*250*	*50*	*40*	*0.114878*	*920*	*0.140983*	*1540*	*1646*
Optimal Solution 1	*10*	*150*	*173*	*40*	*0.051307*	*955*	*0.088345*	*1400*	*1655*
Optimal Solution 2	*10*	*170*	*156*	*40*	*0.072291*	*1200*	*0.070494*	*1320*	*1653*

Table 5: Stage 2 optimization results

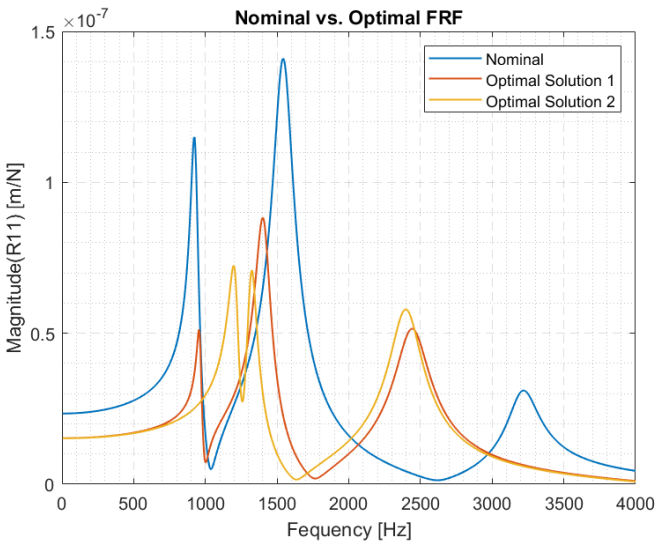

Figure 25: Nominal FRF vs optimal FRF (stage 2 optimization problem)

3.4. Stage 3: Structural Optimization Via Auxiliary Components

The previous sections discussed the sensitivities of various design variables like bearing preloads, bearing positions, and critical shaft dimensions. This information was used to guide the spindle design process, where the dimensions were kept as close as possible to the optimal values previously found.

3.4.1. Current State of Project

At the beginning of this stage of the project, decisions regarding the major shaft dimensions and bearing locations had been finalized and a preliminary design was in hand. Various updates were added to the design based on design and practical considerations. A summary of these is as follows:

- Numerous auxiliary components were added to the design (Figure 26). These components are necessary to achieve a working spindle assembly, as will be explained shortly. With the addition of these components, the geometry of the design diverged considerably from a simple shaft-bearing system, with potential effects on the system dynamics and thermal behavior.
- It was decided to exclude the drawbar from the design due to financial constraints. Considering this as an opportunity, it was decided that the central hole in the shaft would be utilized for cooling. Cooling media can be circulated inside a moving shaft with the help of a rotary union.
- The general range for bearing preloads was set based on guidelines from an industrial partner specializing in high-speed spindles. The guidelines speculated that the medium preload classes specified by the manufacturer should be targeted. For example, for the front bearing, the SKF preload classes are Class A, 55 N; Class B, 166 N; Class C, 331 N. This suggestion is based on experience and the fact that precise preloading during assembly is not always guaranteed and there is a margin of up to +/- 20-30 N with spring preloading. Therefore, targeting the middle value is a safe option. These guidelines were partially in line with the previous findings, where the front bearing preload values in the pareto front were spread throughout the defined range but the rear bearing preload values converged towards the minimum value. For the simulations in this section, this guideline was adapted, and the medium class preload values were assigned to all bearings.

3.4.2. Auxiliary Shaft Components

A number of auxiliary components were incorporated into the design for practical reasons. These components add mass to the system, altering the stiffness/damping of the overall structure. Moreover, from a thermal point of view, these components can also affect the heat transfer capabilities of the spindle due to their direct contact with the shaft and interaction with the internal environment of the spindle housing, which carries circulating air and other cooling media. A brief discussion to explain the purpose of these auxiliary components is provided below.

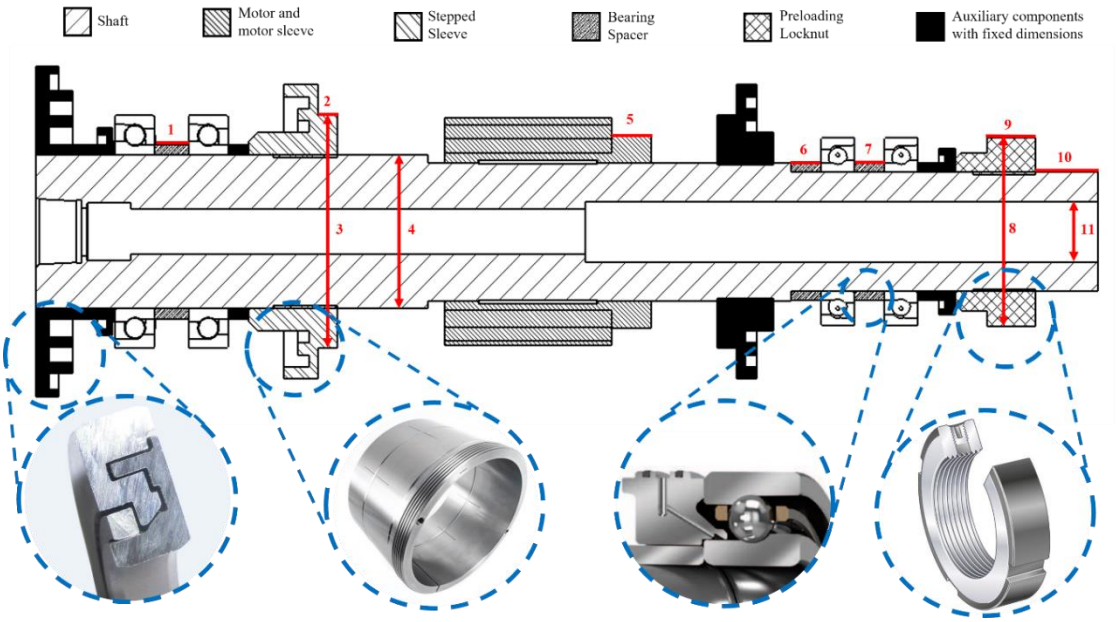

Figure 26: Auxiliary components in spindle shaft assembly

3.4.2.1. Press-fitted sleeves

Press-fitted sleeves on a spindle shaft can be categorized as stepped sleeves and motor sleeves. The additional mass and stiffness press-fitted sleeves introduce into the system contribute to changing dynamic responses. Since the locations of press-fitted sleeves are

generally close to heat sources such as bearings and motor in a spindle, they also contribute to thermal dissipation by enhancing forced convection heat transfer by enlarging rotating surfaces while composing a thermal resistance medium between the heat sources and the spindle shaft instead of enlarging shaft with shoulders during the design.

Stepped sleeves

Stepped sleeves are designed to lock the shaft bearings or built-in motors in their determined axial positions. They have an internal step and are press-fitted on the shaft, usually with high interference fits to stiffen the shaft against bending moments and axial displacements. Depending on the design, the interference fit may occur on either one or both portions of the internal step. They can serve as labyrinth seal rotors for oil leakage prevention and contamination.

Motor sleeves

Motor sleeves are employed in electro-spindles to assemble a motor to a shaft. The spindle housing contains the stator while the rotor is mounted on the shaft over a press-fitted sleeve. Since this rotor has a non-negligible mass, occupies a significant portion along the length of the shaft, and is a major source of heat, it is an important auxiliary component in the context of thermal and dynamic behaviors.

3.4.2.2. Bearing spacers

Bearing spacers are ring-like components between individual bearings in the front and rear bearing sets. They comprise a rotor on the spindle shaft and a stator part assembled on the spindle housing. They are an essential part of the bearing preloading mechanism. Their width is generally adjusted within a small range through precision grinding, enabling fine relative axial movements of the bearing rings. This axial displacement induces preload in the bearing set. This work focuses only on the spacer rotors they are in direct contact with the shaft.

3.4.2.3. Preload Locknuts

Preload locknuts are precision bearing accessories used to accurately locate and preload spindle bearings. The preloading is applied by tightening the lock nut against either the inner or outer ring of the bearing, while the other ring remains locked in position.

3.4.3. Dynamic Sensitivity

Figure 27 illustrates the aggregate impact of all auxiliary components on the spindle-tip FRF for the shaft geometry shown in Figure 26. It is clear that the inclusion of auxiliary components, while not drastically changing the dynamic properties of the spindle, are still feasible parameters for fine-tuning the design for improved performance.

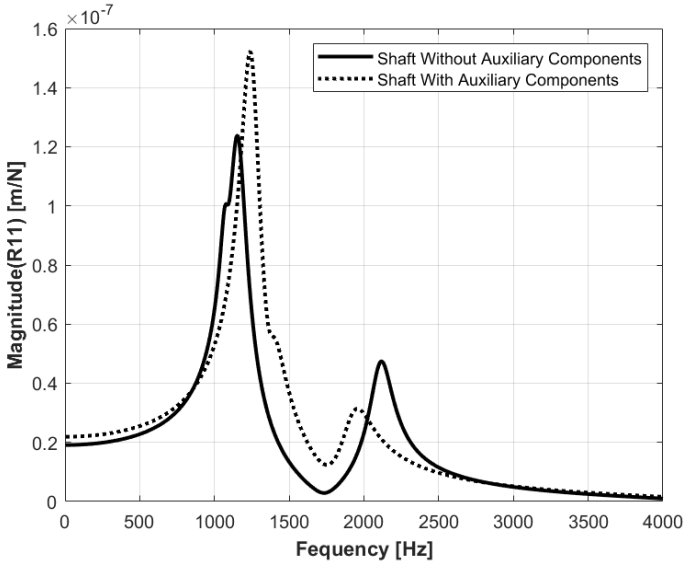

Figure 27: Spindle-tip FRF with and without auxiliary components

To quantify the effect of each auxiliary component, a sensitivity analysis was initially conducted for spindle dynamics. The dimensions that could still be varied based on the prevalent state of the design were identified as shown in Table 6. The chosen performance indicators for this sensitivity test were the natural frequency and FRF amplitude of the first dominant mode.

Variable No.	Variable Name	Lower Bound (mm)	Upper Bound (mm)
1	*Front bearing spacer length*	*5*	*15*
2	*Front stepped sleeve length*	*5.75*	*25*
3	*Front stepped sleeve diameter*	*55*	*80*
4	*Motor shoulder diameter*	*45*	*65*
5	*Motor sleeve length*	*5*	*20*
6	*First rear spacer length*	*6*	*12*
7	*Second rear spacer length*	*6*	*12*
8	*Rear locknut diameter*	*40*	*70*
9	*Rear locknut length*	*15*	*35*
10	*Tail extension length*	*0*	*150*
11	*Shaft central hole diameter*	*10*	*30*

Table 6: Upper and lower bounds of variable dimensions

These performance indicators were checked throughout the defined range for each variable and the largest change in each indicator was recorded for each variable. Figure 28 shows the sensitivities of each variable with respect to both the performance indicators. A minimum threshold of at least 5% change in dynamic behaviors was used to identify a variable as being ‘sensitive’. According to this criteria, six out of the eleven variable dimensions are sensitive. It was observed that the natural frequency is much less sensitive to change compared to the FRF amplitude, which varied up to ±10% at certain instances. Some of these sensitive dimensions are discussed further in the remainder of the section.

It is pertinent to mention here that it was assumed that the auxiliary components were rigidly coupled to the shaft. Therefore, the effects of contact mechanics due to press-fit and threaded joints are ignored.

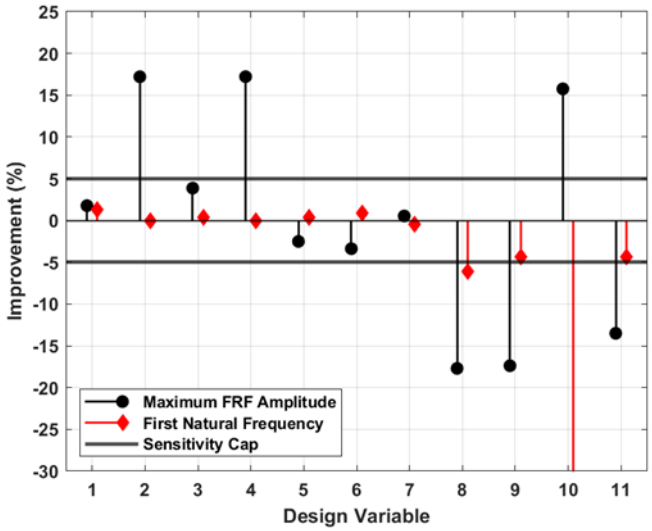

Figure 28: Summary of sensitivity analysis

3.4.3.1. Front Stepped Sleeve and Motor Shoulder

The length of the front stepped sleeve (variable 2) and the diameter of the motor shoulder (variable 3) show high sensitivity for the dominant FRF amplitude. They act as the same variable, though, as they add mass to the same section of the shaft (behind the front bearing set). Figure 29 demonstrates the effect of changing the sleeve's length from 5 mm to 25 mm, which decreases the amplitude of the dominant mode by 17% through mode

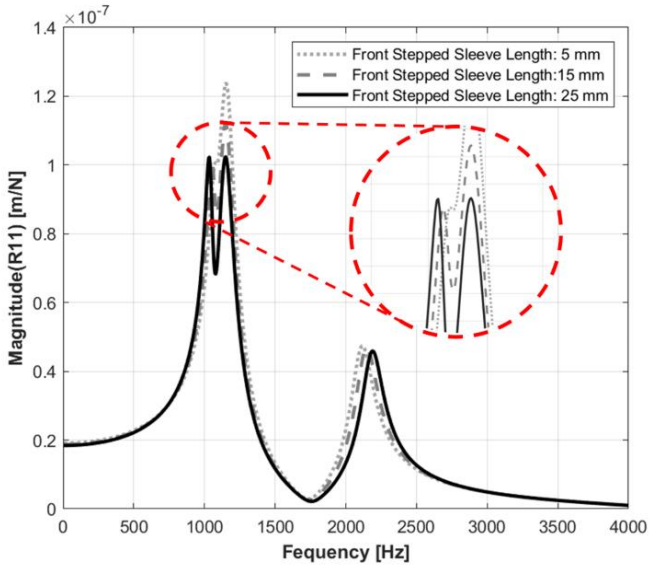

Figure 29: Sensitivity of front stepped sleeve length splitting.

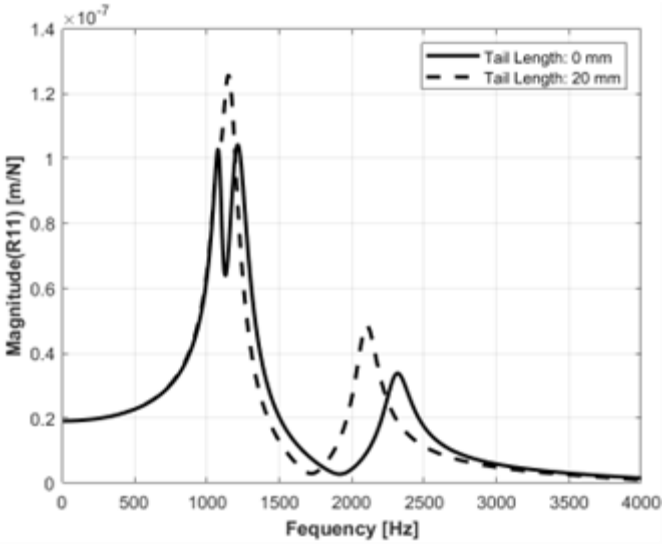

Figure 30: Tail length sensitivity

3.4.3.2. Spindle Tail Components (Shaft Tail and Preloading Locknut)

The tail diameter and length, and the length of the preloading locknut (variables 8, 9, and 10) define the tail section. As observed previously, these can be tuned to achieve the dynamic absorber effect.

The results of the tail length (variable 10) variation were particularly interesting, where decreasing the tail length from 20 mm to 0 mm led to a more rigid assembly (Figure 30). This contrasts with previously reported results [10] [14], where the tail was elongated to achieve the mode-splitting effect, adding mass to the assembly. By decreasing the tail length to 0 mm, a 2.5% weight reduction was achieved. This is a positive outcome that may be exploited in spindle design.

3.4.3.3. Shaft central hole

The hole at the center of the spindle shaft (variable 11) is one of the sensitive parameters. Figure 31 shows that altering the diameter of the central hole can be useful in creating a dynamic absorber effect.

It is to be noted that due to peripheral systems like the drawbar occupying the center of the shaft, the diameter of the shaft hole is not completely free to change as taken in this study. However, it may still be adjustable within a small range with an appropriate selection of drawbar or toolholder size.

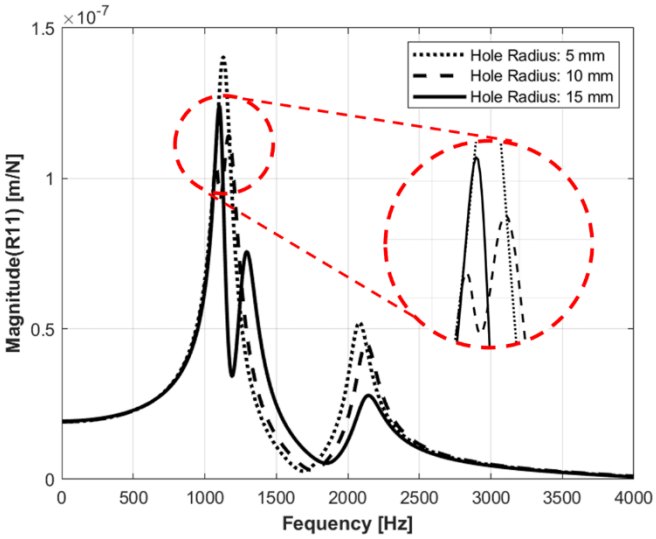

Figure 31: Shaft hole radius sensitivity

3.4.4. Thermal sensitivity

At this stage in the project, our group had a better understanding of the thermal interactions in spindles and different simulation efforts had also been tried for thermal modeling. Since the central hole was to serve as a carrier for cooling media for through-cooling, a thermal sensitivity check was performed for it in addition to the dynamic analysis. A reduced order model based on finite element analysis was built for this purpose representing the thermal response with respect to all design variables. Thermal performance was gauged by the front bearing temperature and spindle-tip thermal growth. To ensure that the shaft was not weakened beyond a certain safe point due to the hole, the normal and shear stress safety factors were also computed as outputs to constrain the hole diameter. It was found that the shaft hole radius is the most sensitive variable with regards to thermal performance, while others showed negligible changes.

The variation of these parameters (normalized with respect to maximum value) throughout the range of the central hole radius is shown in Figure 32. As expected, the spindle-tip thermal growth and front bearing temperature decrease as the hole gets bigger. This is because of a larger coolant volume circulating through the shaft. However, enlarging the hole also causes a loss of strength, as observed by the decreasing stress safety factors. Therefore, there is a trade-off between thermal performance indicators and stress safety factors, warranting the use of an optimization approach.

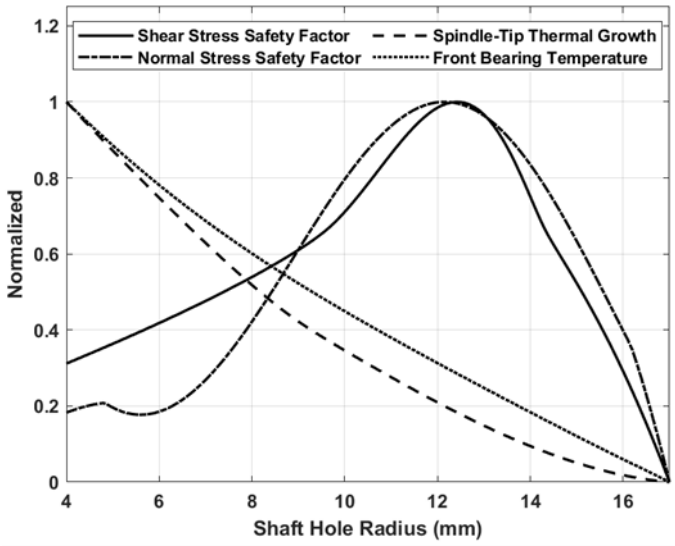

Figure 32: Thermal sensitivity of shaft hole radius

3.4.5. Optimization Problem

Considering the results of the sensitivity analysis and bearing assembly constraints in mind, the following multi-objective optimization problem was formulated:

$$
\begin{aligned}
&\textit{Min} \quad J(1): max(|\boldsymbol{R_{11}}|)/\ max(|\boldsymbol{R_{11}}|)_{nom} \\
&\textit{Min} \quad J(2): 1/(\boldsymbol{\omega_1}/\boldsymbol{\omega_{1,nom}}) \\
&\textit{Min} \quad J(3): \alpha_{spindle\text{-}tip}/\ \alpha_{spindle\text{-}tip,nom} \\
&\textit{Min} \quad J(4): m/m_{nom} \\
&\\
&s.t \quad 5.75 < X(1) < 12 \\
&\qquad 53 < X(2) < 65 \\
&\qquad 45 < X(3) < 70 \\
&\qquad 10 < X(4) < 20 \\
&\qquad 0 < X(5) < 150 \\
&\qquad 9.7 < X(2) < 14.5
\end{aligned}
\tag{3.2}
$$

In Eq. 3.2, the objective function matrix, *J*, contains $max(|R_{11}|)$, the maximum FRF amplitude, ω_1, the first natural frequency, and $\alpha_{spindle\text{-}tip}$, the spindle tip thermal growth, and m, the spindle mass. These set of objective functions represent both dynamic and

thermal behaviors of the spindle. Moreover, the fourth objective related to mass was also added as there was an opportunity to reduce the mass by tuning various dimensions. By reducing the system mass, higher modal frequencies can be achieved as well as better energy efficiency as the motor's work against inertia and friction is reduced.

The design variable matrix, *X*, contains the six sensitive components: front stepped sleeve length (1), motor shoulder diameter (2), rear stepped sleeve length (3), rear stepped sleeve diameter (4), tail length (5), and shaft central hole (6). The box constraints (9.7-14.5) for the shaft hole radius are set based on the following criteria:

- Shear stress safety factor > 2
- Normal stress safety factor > 1

Any hole radius value not satisfying these criteria are filtered out. Thus, the constraining part of this problem is handled by setting appropriate box constraints rather than using a constrained optimization scheme.

For running the simulation, all objectives were normalized against their nominal values. Also, it is to be noted that the simulations were performed for a speed of 40,000 RPM. The bearing softening effects were included in the bearing stiffness calculations, but the shaft softening effects (centrifugal and gyroscopic) were ignored owing to their small contribution to changing behaviors. Moreover, the thermal analysis also represents the spindle conditions at 40,000 RPM. For this study, only shaft cooling is considered while peripheral cooling systems are ignored.

3.4.6. Optimization Results

The optimization problem in Eq. 3.2 was run for 50 iterations with a population size of 25 and an external archive of 50 members. Figure 33 shows the pareto front obtained from this simulation. It was observed that the pareto front was roughly divided into two clusters. In the first cluster, most solutions exhibited improvement for all four objectives, while the remaining had worsened only in terms of the first modal frequency.

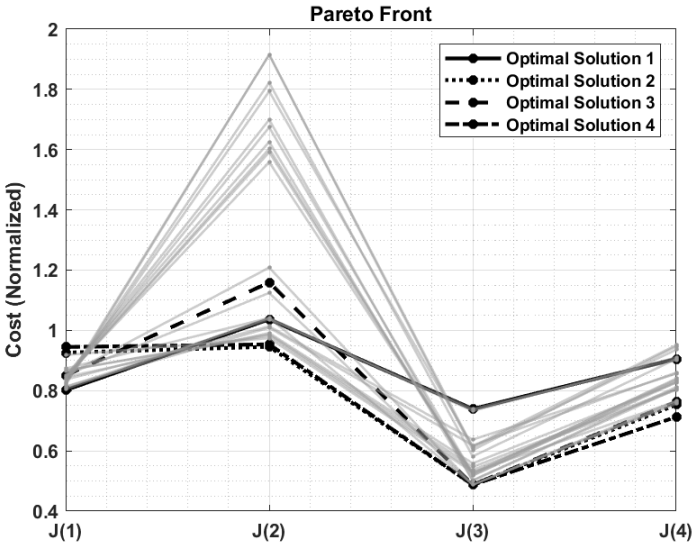

Figure 33: Pareto front for stage 3 optimization problem

The second cluster showed a large deviation from the first cluster in terms of the modal frequency objective, *J(2)*. This is an indication that for this set of solutions, an additional mode appeared in the FRF in the lower frequency range. This occurrence 'tricked' the algorithm into picking the wrong natural frequency as the dominant mode. Since other objective function values still showed strong improvements, these solutions remained a part of the pareto front. Due to this issue, this second cluster represents an irrelevant solution set which will be ignored in the upcoming discussion.

	Hole Radius (mm)	Tail Extension Length (mm)	Rear Stepped Sleeve Length (mm)	Rear Stepped Sleeve Diameter (mm)	Motor Shoulder Diameter (mm)	Front Stepped Sleeve Length (mm)	Maximum FRF Amplitude (μm/N)	1st Natural Frequency (Hz)	Spindle-tip Thermal Growth (μm)	Mass (Kg)
Nominal Solution	6.6	18.8	14.6	55	53	5.75	0.129	1130	22.9	19.1
Nominal Solution	9.7	0	10	66	53	5.75	<u>0.103</u>	1085	16.9	17.3
Nominal Solution	14.5	81.0	10	45	53	5.75	0.117	<u>1190</u>	11.2	14.4
Nominal Solution	14.5	102.9	10	45	53	5.75	0.109	965	<u>11.2</u>	14.6
Nominal Solution	14.5	0	10	45	53	5.75	0.121	1185	11.2	<u>13.6</u>

Table 7: Optimal solutions

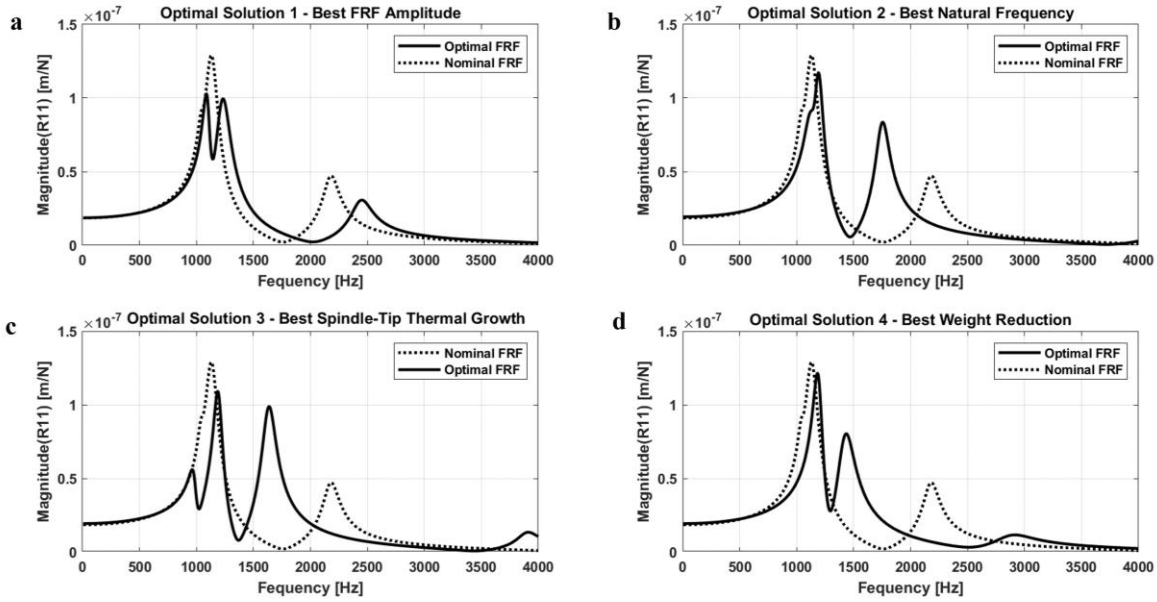

Figure 34: FRFs of pareto optimal solutions

From the remaining solutions, the four best-performing solutions with respect to each objective are shared in Figure 34 and Table 7.

Optimal solution 1 had the best dynamic performance in terms of FRF amplitude, which decreased by 20%. Since the dominant mode splits into two peaks, the dynamic absorber effect was exploited in this case. This solution also exhibited improvements in spindle-tip thermal growth and mass reduction, mainly because of the larger shaft hole accommodating a higher coolant flow. The first natural frequency deteriorated but only to a negligible extent. It is important to note that the tail length in this case is 0. Generally, tail length tuning involves elongating the tail to a specific length to achieve the dynamic absorber effect. In other words, mass is usually added to the spindle assembly. Contrastingly, this solution has a mass reduction. The reason for this could be that dynamic absorber effect relies on the ratio of mass between the principal (shaft) and the absorber (tail) systems [60]. Therefore, it can be achieved by adjusting the masses of either systems. In this case, it seems that the algorithm converged to a solution where both the hole size and tail were reduced to a size that achieved the correct mass ratio for splitting the mode. It is pertinent to mention here that the tail is not entirely eliminated from the design. Rather, only its extendable portion is eliminated. In effect, the tail

comprises everything behind the rear bearing set. In the current design, this includes components like the spacer and locknut. Thus, it is not to be understood that the tail mass is zero.

Optimal solution 2 is the solution with the highest increase in the first natural frequency with an improvement of 5.31%. This is not much, understandably, since the main contributor to natural frequency change is bearing stiffness. Since these remain constant for this analysis, the natural frequency sensitivity is low. Moreover, the second mode shifted to a much lower frequency, which may or may not be beneficial from an application point of view. For this solution, the tail length was 81.9mm, which may be impractical in a working model. In such cases, the dimensions of other components comprising the tail like the rear stepped sleeve can be adjusted to achieve a similar dynamic performance. Increasing the diameter of such components instead of length can be more practical. Using a different material for the auxiliary components can be another method to tune the tail mass.

Optimal solution 3 showed a spindle-tip thermal growth decrease of 51%. Since the hole size is maximum, the cooling effect is maximized, and thus the lower thermal growth. As before, the tail length is exceptionally long at 102.9mm. On the dynamic front, the FRF shows a smaller vibration mode at 965 Hz, which indicates that a small change in any of the parameters may cause unwanted modal interactions in this frequency range.

Optimal solution 4 showed 28.8% mass reduction and had a spindle-tip thermal growth equivalent to optimal solution 3. However, there was not significant change in the dominant dynamic behaviors.

3.5. Stage Four: Fine-Tuning of Adjustable Parameters

The previous stage showed that auxiliary components can be used to improve spindle

performance through dimensional adjustments. The recommendations from this stage were considered in the future design iterations.

In this section, small refinements were applied to the design finalized for manufacturing.

It is also to be noted that the details presented in this section represent the project state at the time of writing this thesis.

3.5.1. Current State of the Project

In stage 3, most of the total design decisions concerning the shaft structure were investigated in detail. However, the design was not finalized, and several further iterations were performed.

Therefore, it is important to discuss here the evolution of our design approach in between these two stages to explain the differences between the final spindle design (refer to chapter 4) and its previous version (Figure 26). During this stage, there was significant interaction with spindle experts from the industry, which was monumental in redefining our design. Only relevant details relevant are mentioned here.

- The frontside stepped sleeve was converted to a press fit sleeve and extended to be in contact with the motor sleeve. This corresponds to variables 2 and 4 in Figure 26. Although the optimizer indicated that their values should be minimal, this upgradation was done for practical purposes to add rigidity to the structure and fix the bearings. The diameter of this sleeve extension was kept small at 58mm.
- Numerous components were added to the rear side of the shaft, changing the mass of the tail section. These include a balance ring, encoder ring, and a locknut to fix these components on the shaft.
- It was decided to exclude the hole in the center of the shaft. This decision was due to the unavailability of appropriate internal cylindrical grinding capabilities up to the desired precision level.
- The tail section was decided to be included as a threaded extension rather than a part of the shaft considering that it is potentially useful in tuning dynamic performance.

- The bearing selection was updated to a more suitable brand. The front and rear bearings are FAG HC71909-C-T-P4S-UL and FAG HC71907-C-T-P4S-UL, respectively. These hybrid bearings are more suitable for high-speed spindles. The ball sizes, numbers, and preload ranges for these bearings are significantly different from the previous bearing models. Their specifications are shared in Table 8.
- Based on the recommendations of industry experts, the preload should be selected from the lowest two classes due to thermal and bearing service life considerations. Thus, the available preload range was shortened to low preloads.
- The front and rear bearing sets are to have the same preload to maintain force balance in the back-to-back configuration. This was true for previous versions as well but understood by the author only recently after interaction with industry experts. In previous analyses, however, the difference in preloads between the front and rear bearing sets is not too high and is deemed to be within a practical range.

Specification	**Front Bearing**	**Rear Bearing**
Bore Diameter (mm)	*45*	*35*
Outer Diameter (mm)	*68*	*55*
Width (mm)	*12*	*10*
Ball Diameter (mm)	*4.3*	*3.4*
Number of Balls	*27*	*25*
Contact Angle (Degrees)	*15º*	*15º*
Inner Race Curvature Ratio	*0.5355*	*0.5355*
Outer Race Curvature Ratio	*0.5255*	*0.5255*
Ball Material	*Ceramic*	*Ceramic*

Table 8: FAG bearing specifications

The extensive nature of these design updates is expected to change the dynamic and thermal behaviors of the spindle design discussed previously. Therefore, there is an undeniable possibility that the optimal results obtained in previous sections are not fully applicable to this new version. However, all changes in the design were guided by previous findings and reevaluated using the aforementioned methods.

Considering these developments, the remaining design variables were fine-tuned for better performance. While formal optimization was not used for this due to the low number of variables, a brief overview of its results is reported in this section. These results were shared with the assembly team for their reference.

3.5.2. Bearing Preloads

The bearing preloads are adjusted during assembly and thus remain variable. While the defined preload range is small, a basic sensitivity analysis is still useful to ascertain the effect of preloads on spindle performance.

Since it was decided to use low preloads to avoid excessive heat generation, thermal considerations were ignored at this point and only the FRF was computed. As before, bearing damping values are unknown due to unavailability of experimental results. Thus, they are taken the same as in previous sections.

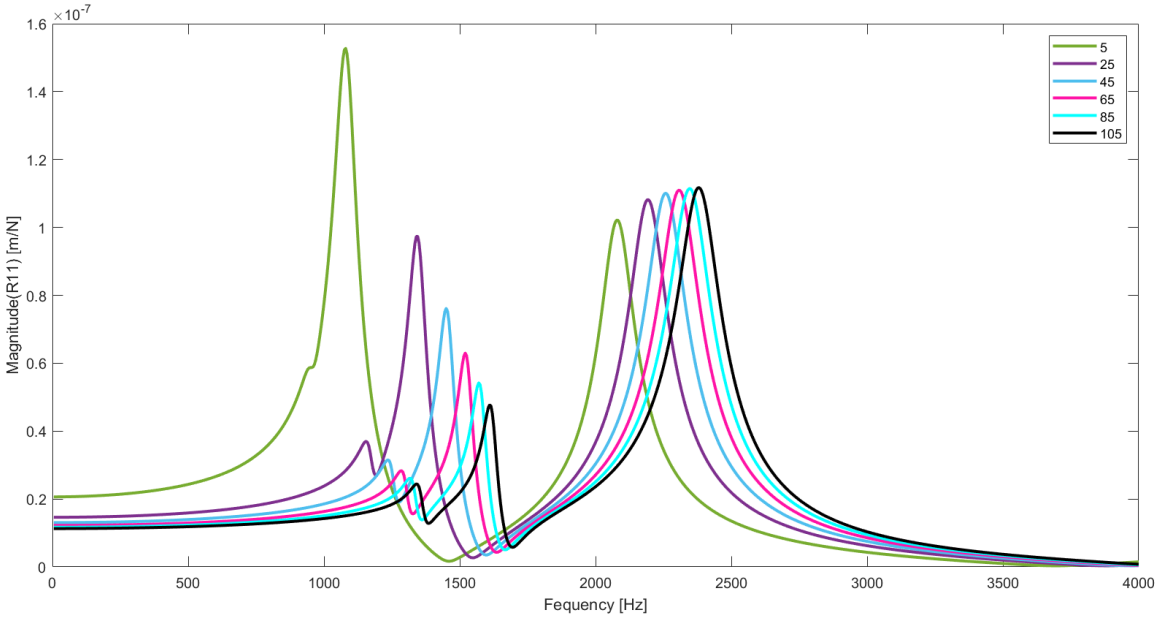

Figure 35: Spindle-tip FRF for various preloads

Figure 35 shows the variation of the spindle-tip FRF for different preloads. The trend is straightforward and expected. Higher preloads cause the spindle rigidity to increase,

particularly for the first mode. The second mode remains relatively unaffected, thus does not have any bearing on the final decision.

Considering this trend, a preload in the range of 40-60N per bearing will be suggested to the manufacturer. For assembly purposes, the total preload force would be 80-120N considering two bearings in each set. This suggestion is in-line with their advice and the preload ranges defined by the bearing manufacturer.

3.5.3. Tail Length

The last remaining variable is the tail length. It can be tuned to a specific length, or diameter, to fine-tune the spindle-tip FRF. In the final spindle geometry, the tail is included as a detachable extension, allowing control over its dimensions.

Figure 36 shows the sensitivity of FRF to the tail length when preload is fixed at 50 N. The dominant mode can be shifted slightly by adjusting the tail length. Moreover, the amplitude of the mode at ~1500 Hz can also be reduced with a longer tail. While the changes in the FRF are not substantial, tail length-tuning can be a viable option for fine-tuning spindle dynamics to suit the application.

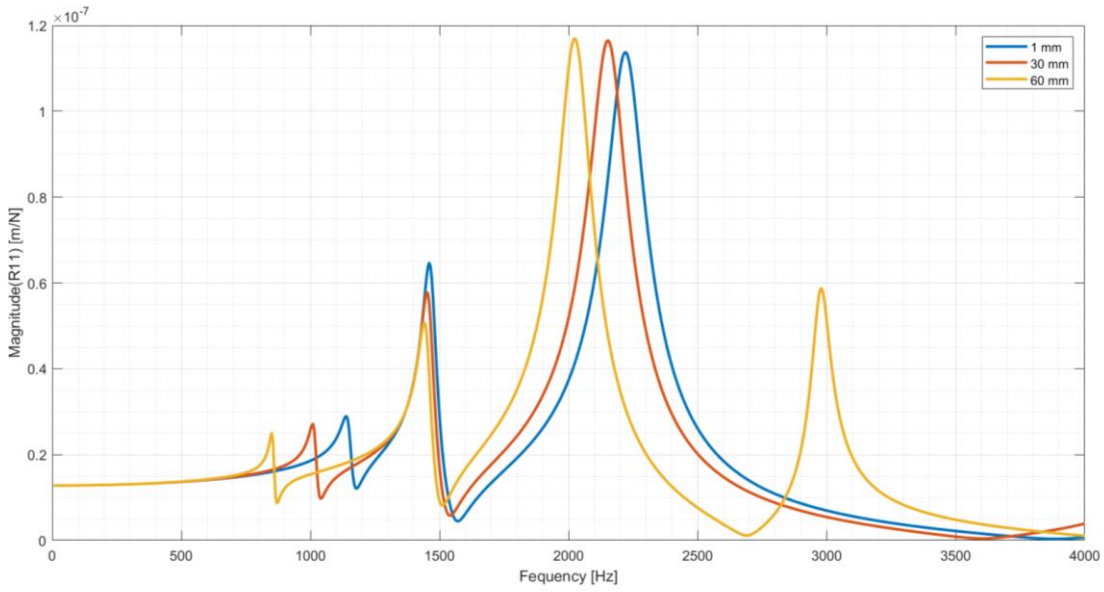

Figure 36: Spindle-tip FRF for various tail length extensions

3.6. Summary

This chapter covered the main contribution in this thesis. An in-depth discussion was presented on how the developed multiobjective optimization scheme was implemented on our high-speed spindle design. The optimization was presented in four stages, each stage representing a different period in the spindle design timeline.

In the first stage, a comprehensive sensitivity analysis was conducted for various spindle design parameters to understand the problem and to identify the parameters most suitable to include in subsequent optimization problems. Numerous dimensions and bearing characteristics were identified.

In the second stage, an optimization problem was designed based on the findings of the previous stage. Based on the current state of the design, the problem was based on a simple shaft-bearing assembly. The optimal solution provided important information on design decisions regarding bearing locations and revealed trade-offs between dynamic and thermal characteristics.

In the third stage, an updated structural optimization problem was formulated based on various auxiliary components added to the design since the previous optimization study. The optimal results showed significant improvements, identifying design configurations that improved dynamic performance via the dynamic absorber effect, reduced thermal growth, and minimized the weight of the rotating assembly.

In the final stage, a basic sensitivity analysis was performed for the design parameters that are still variable in the finalized spindle design. These are to serve as a reference for the assembly of the spindle and for future studies.

4. PRACTICAL ISSUES IN DESIGN & MANUFACTURING OF HIGH-SPEED SPINDLES

The scope of the discussed research project included both the design and manufacturing of a high-speed spindle. The design for this spindle was completed entirely in-house. A significant portion of the manufacturing and assembly was also directly managed and observed by members of our research group. Moreover, throughout the duration of this project, our group extensively collaborated with industrial design and manufacturing experts on practical matters and the refinement of our design.

These efforts, though not academic in nature, consumed significant time and helped us fully understand the working of machine tool spindles.

This chapter will summarize the author's learning and contribution to the design and manufacturing part of this project and explain the justifications behind our decision-making.

4.1. Breakdown of High-Speed Spindle Units

High-speed spindles are a highly complex machinery comprising numerous sub-systems and peripheral devices, all of which are critical to their smooth functioning. The main subsystems included in a typical design are:

- **Mechanical**
- **Cooling**
- **Lubrication**
- **Sealing**
- **Electric**

The schematic in Figure 37 illustrates the interaction between these subsystems as well as their main constituents. The CAD model in Figure 38 represents our final design.

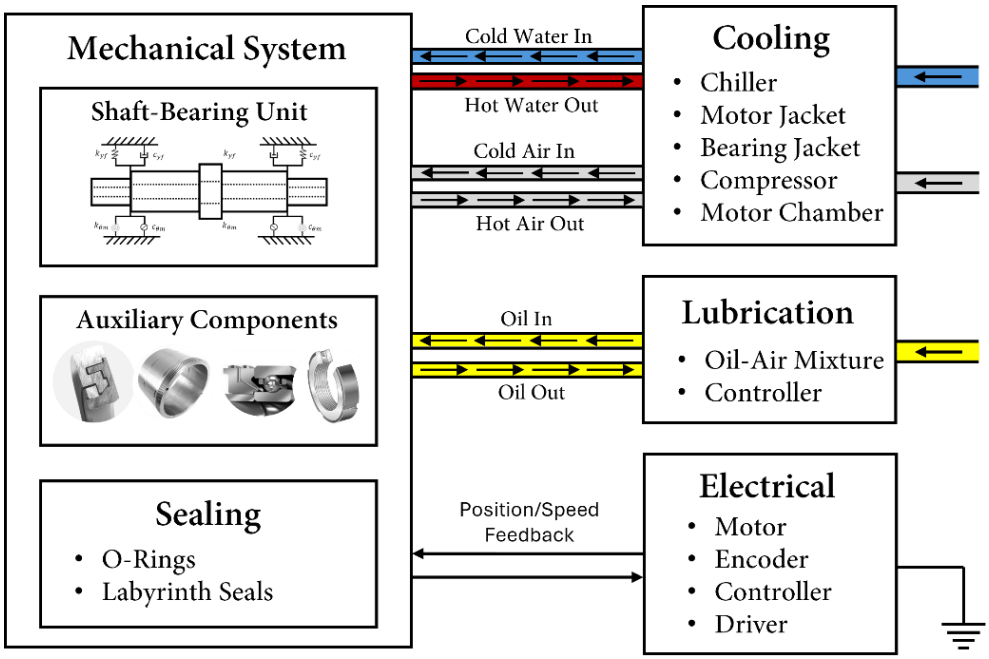

Figure 37: Schematic representation of high-speed spindle

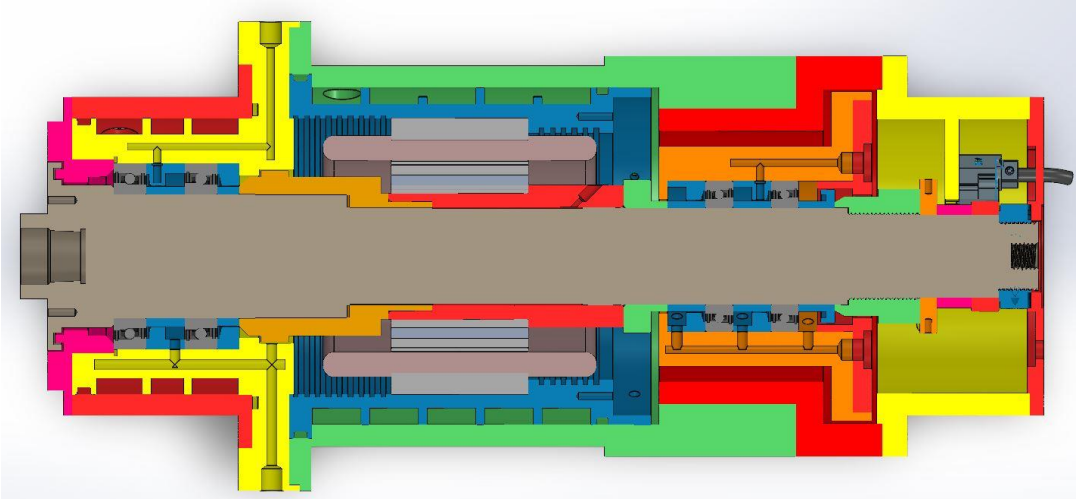

Figure 38: Cross-sectional view of final spindle design

4.2. Mechanical System

The structure of the spindle is its central subsystem, whose main purpose is to accommodate the entirety of the spindle components in a compact and safe manner.

4.2.1. Shaft-Bearing System

The shaft-bearing system defined the main scope of this thesis. Thus, the author was involved in several decisions required to finalize the configuration for this system.

4.2.1.1. Bearings

Design Considerations

The choice of angular contact ball bearings is standard for high-speed spindle applications. These bearings support both axial and radial loads, allow control over shaft rigidity through preloading, and have a low friction design.

A low contact angle of 15^{o} was chosen. Although this lowers axial load carrying capacity, it decreases friction due to less load on the rolling elements. At higher speeds, thermal issues are more significant to tackle than stiffness, thus small contact angles are preferred.

Moreover, high-speed spindles are generally used for low load applications like micro-milling, where slightly lower axial rigidity is also suitable.

Hybrid bearings were chosen due to their superior material combination of nitride ceramic ball and steel rings. Ceramic materials are much lighter than steel, which significantly reduces high-speed inertial effects like centrifugal forces on the balls. Ceramics also have a lower thermal expansion coefficient, which keeps thermally induced preloads to a minimum. Moreover, ceramics have exceptionally superior tribological properties which help improve surface stresses and lubrication efficiency at the ball-ring contact interfaces.

The chosen FAG bearings also feature small ball diameters. This allows for smaller outer ring diameters, decreasing the overall mass of the bearing and allowing a compact design. This is significant in minimizing inertial effects at high speeds. Furthermore, a higher number of balls is used, allowing for a more uniform load distribution on bearing components due to more contact points.

Manufacturing Considerations

The bearing assembly requires care. The inner rings should have a slightly tight fit with the shaft. This is necessary to avoid disengagement of the inner rings from the shaft at higher speeds due to centrifugal expansion. An excessively tight fit is also to be avoided as it causes high friction and heat generation [20]. Moreover, the form (cylindricity, flatness, runout) of the shaft is also important for ensuring even load distribution among the rolling elements.

The outer rings are required to have a slightly loose fit to accommodate centrifugal expansion of the outer rings. Moreover, a tight fit for both rings is also likely to generate excessive internal forces in bearing components.

Considering these concerns, appropriate shaft tolerance (±3.5µm), housing tolerance (-3, +5µm), and form tolerances were selected from the bearing catalogue.

4.2.1.2. Bearing Configuration

Due to the non-symmetric behavior of angular contact ball bearings, they can be mounted on the shaft in different configurations. Numerous studies have shown that the back-to-back configuration, or O-configuration, is better suited for high-speed applications compared to the face-to-face/X configuration [Ref]. The difference between them is shown in Figure 39.

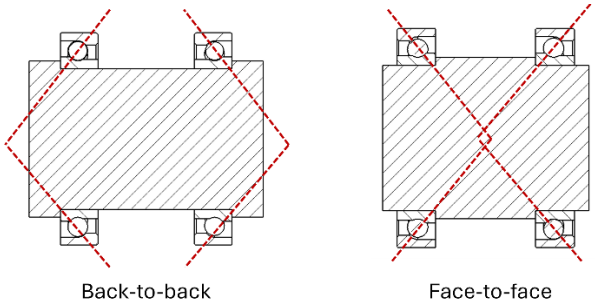

Figure 39: Bearing contact angles in O- and X-configurations

The resultant spindle is more rigid due to a larger support in the bearing load apex points and resistant to angular misalignments. Moreover, this bearing arrangement is also better at accommodating thermally induced preloads as the expanding shaft acts against the direction of bearing contact, causing it to decrease.

4.2.1.3. Preloading Mechanism

Design Considerations

Bearings on a shaft can be preloaded by numerous mechanisms: constant, spring, or fixed displacement. The main difference between these is how the preload changes at higher speeds and under thermal loads. Details of these can be found in [17].

Manufacturing Considerations

The constant preload mechanism is chosen for our spindle as it is the most high-speed-compliant as the preload remains almost constant even in tough operation conditions. Considering that reaching 40,000 RPM is the goal, this mechanism was finalized. The designed preloading mechanism and process is explained through Figure 40 below.

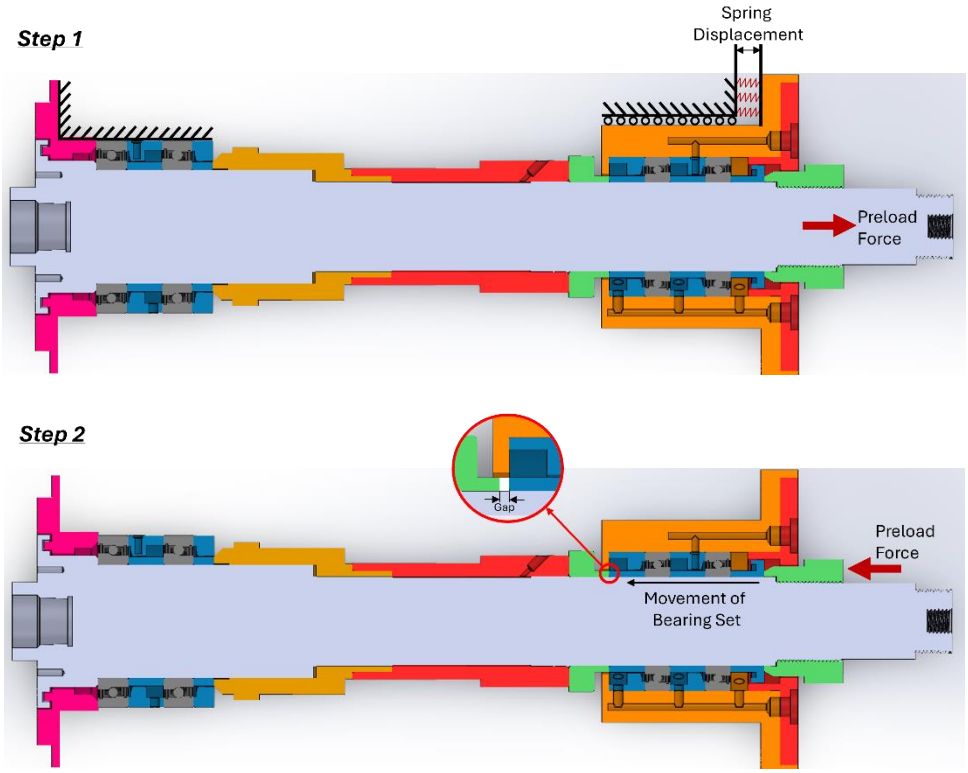

Figure 40: Bearing preloading procedure

Initially, the bearings are mounted on the shaft along with the relevant auxiliary components. The inner rings of both bearing sets are press fit on the shaft. Therefore, their movement is locked to the axis of the shaft. The outer rings of the front bearing set are fixed to the housing.

The outer rings of the rear bearing set, however, are free to move owing to the ball cage in the rear-side assembly, shown as a sliding connection in Figure 40. This ball cage isolates the motion of the rear bearing set from the assembly. Furthermore, soft preloading springs are mounted in between the fixed housing and the movable rear bearing set. These are precision springs whose stiffness constant is known to the assembly expert. Therefore, their linear force can be precisely monitored by measuring the movement of the shaft assembly. The relevant parts are shown in Figure 41.

Figure 41: Ball cage mechanism for constant preloading system

In step 1, the housing is fixed, and the shaft assembly is pulled backwards by approximately the same force as the desired preload. This movement preloads the front bearing set as it is against the contact angle of the front bearings. The force is monitored by measuring how much the springs decompress during this process. Typically, this movement is in the order of a few micrometers, thus, precision equipment is required to measure the displacement. This level of sensitivity also introduces an error of 20-30N in the preload force.

In step 2, upon reaching the desirable preload force, the rear locknut is tightened to the point that the rear bearing set produces an equivalent preload force as the front bearing set. During this operation, the inner rings of the rear bearing set are displaced along the shaft's axis. One of the spacers in the rear-side assembly is used to create the required gap for accommodating this displacement.

It is important to exercise caution in applying tolerances to components assembled with the ball cage due to its important function and it being in close vicinity to a heat source (rear bearing set). Slightly loose fits of -0.01mm on the inner part and +0.005 on the outer part are set to allow the ball cage to maintain a smooth sliding interface throughout the operating temperature range.

4.2.2. Auxiliary Shaft Components

The shaft-bearing system is supported by a range of auxiliary components that are necessary to achieve an assembly with high mechanical integrity.

4.2.2.1. Stepped Sleeve

Stepped sleeves are critical in positioning and fixing bearings on the shaft. The bearings required precision positioning to avoid unwanted misalignments and changes in preload. To generate appropriate axial force to rigidly fix the bearings, a tight fit is used. Additionally, it is important to maintain flatness at the end faces of the stepped sleeve to avoid moment loads induced by uneven force distribution at the contact faces.

Press fit components are also known to increase shaft rigidity [61]. Using press fit stepped sleeves can, therefore, also stiffen the system.

4.2.2.2. Motor Sleeve

The motor rotor is mounted on the shaft via a sleeve. Since this sleeve is the main power transmitting component between the motor and the shaft, it must be tightly fit on the shaft to avoid loss of contact. A precision locational interference fit of H5 is used for this purpose.

Furthermore, a hydraulic mounting setup is used to achieve a uniform tight fit. The cross-sectional view in Figure 42 shows a small chamber machined along the contact interface between the sleeve and shaft. A nozzle opening is provided into this chamber. After the

initial mounting, oil is gradually injected into this chamber via the nozzle to slightly expand the shaft. Due to the uniform nature of hydraulic pressure, all uneven mounting stresses are relieved.

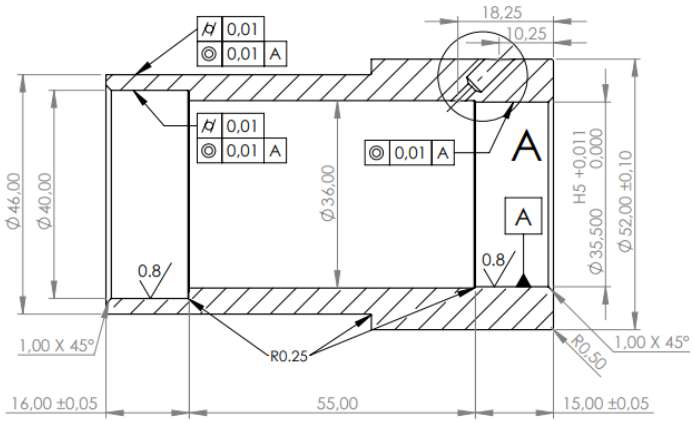

Figure 42: Technical drawing of motor sleeve

Due to the important nature of this component, strict form tolerances are also applied to minimize misalignments and local stress concentrations, as shown in Figure 42.

4.2.2.3. Locknuts

Design Considerations

Locknuts serve the purpose of firmly locating components on the shaft and preloading the bearings. In our design, various locknuts were initially used to fix most of the components on the shaft. However, all but two of these were later replaced by press fit sleeves to prefer uniform tight fits. Locknuts, while very precise, are still not as accurate as sleeves as they have threads, which are very difficult to machine coaxially to the body of the locknut.

The two remaining locknuts are for preloading the bearings from the rear side and for fixing the encoder ring to the shaft (Figure 43). The former locknut is necessary to include as relative axial movement is required for the preloading operation. The latter is kept for ease of assembly/disassembly, it being the last component on the shaft.

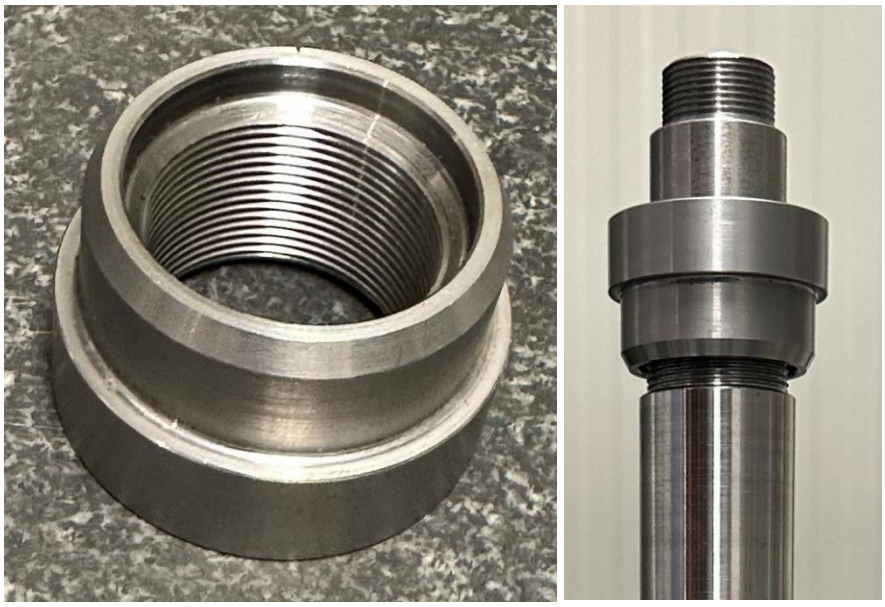

Figure 43: Bearing preloading locknut

Manufacturing Considerations

Precise machining of locknuts is important to achieve even preload on the bearings. Uneven preload force distribution on bearing faces causes misalignments, unwanted stress spikes, and lubrication disparities between rolling components.

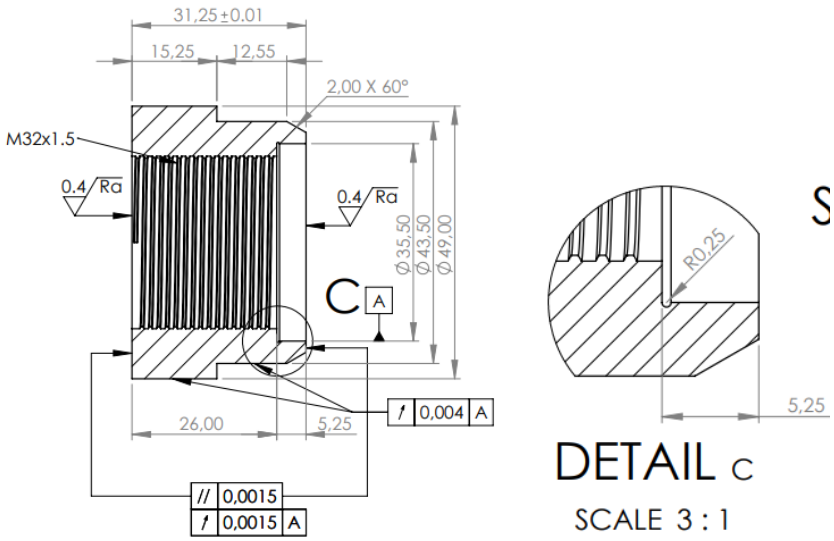

Figure 44: Technical drawing of bearing preloading locknut

Therefore, tight parallelism and runout allowances were included to maintain accurate form as shown in Figure 44. Moreover, a fine surface finish is also preferred. The thread size was chosen based on recommendations in the bearing catalogue for the selected

bearing sizes. This is an important consideration as the thread size also correlates to the required tightening torque for properly mounting the bearings.

The detail view in Figure 44 shows a small groove of R0.25, which is an important design feature that provides an adequate gap for allowing the locknut to freely move axially for preloading.

4.2.2.4. Bearing Spacers

Design Considerations

The bearing spacers are necessary to include as single row angular contact ball bearings cannot be preloaded alone. A spacer setup with a sufficient gap is required to allow the inner and outer rings to displace relative to each other, generating the preload force. They are also critical in providing a degree of thermal isolation between adjacent bearings. The width of the spacers is kept in the range of bearing width, by design convention.

In our design, the spacers also accommodate components from the lubrication system. Figure 45 shows these details. The designed nozzle has two different spraying points within the spacer, the first of which is optimized for a 15-degree contact angle from the ball-bearing base points. The second oil-air nozzle targets the cage-ball bearing space. Notably, the oil-air nozzle diameter is 0.8 mm, Similarly, a drainage hole is also drilled in spacers to allow this mixture to exit. These features were designed according to guidelines provided by the bearing manufacturer KOYO [62].

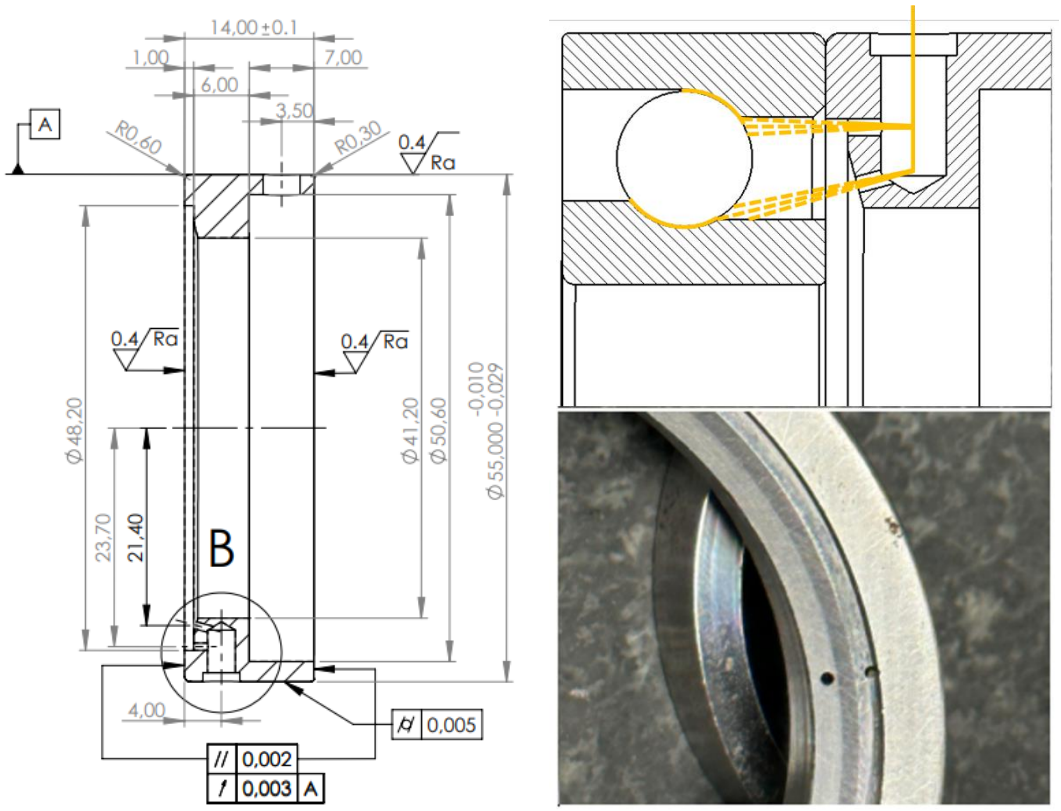

Figure 45: Bearing spacers

Manufacturing Considerations

Precise fits are unnecessary for bearing spacers as their main purpose is to separate adjacently mounted bearings. This is not affected by factors like centrifugal expansion or small thermal expansions. Hence, loose fits are maintained for both the inner and outer spacer rings. Functionally, they will act like floating rings that are axially fixed by the bearings.

4.2.2.5. Balance Ring

Shaft mass balancing is vital for machine tool spindles. Generally, this is achieved by checking the balance after completion of the assembly and removing mass where necessary. In our design, two locations are provided for this purpose for the assembly experts.

A balance ring is mounted at the rear end of the assembly and an area on the front end of the shaft is kept for balancing purposes. These features are shown in Figure 46.

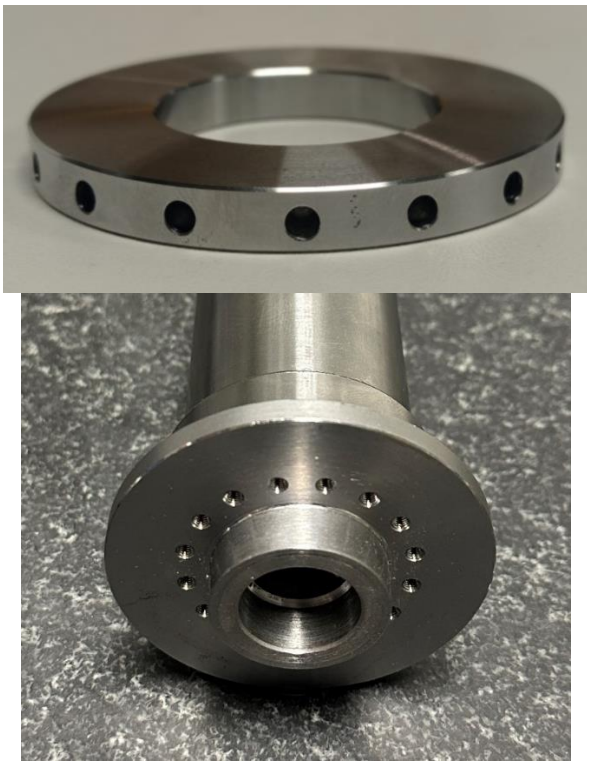

Figure 46: Shaft mass balancing features

4.3. Cooling System

The cooling system is imperative for efficient thermal management of the spindle. There are two main sources of heat in a machine tool spindle: bearings and motor. Thus, the cooling system can be discussed with respect to these two. In fact, it was designed as two separate sub-systems, as shown in Figure 47.

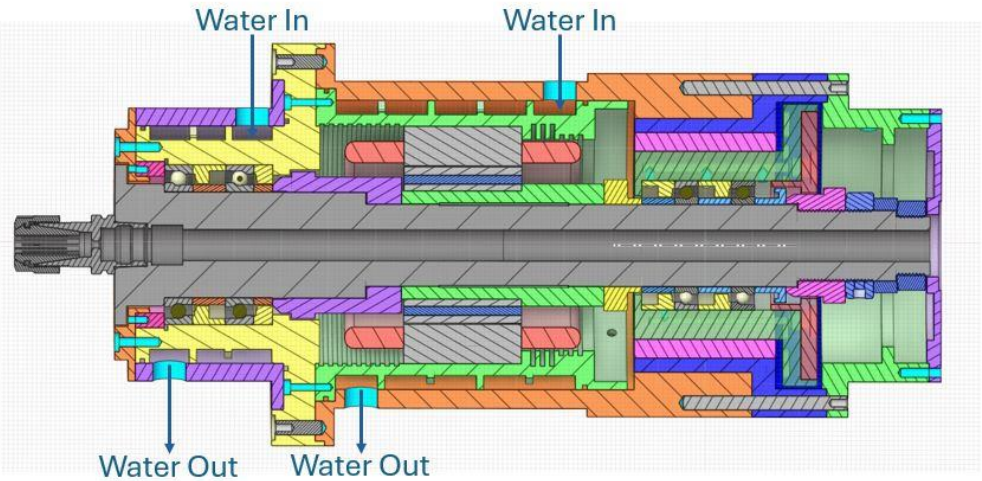

Figure 47: Water cooling system channels

Water is chosen as the cooling media, which will be circulated through cooling jackets assembled around the heat-sensitive areas. A chiller unit will be used to maintain the temperature and flowrate of the cooling water.

4.3.1. Motor Cooling

The motor produces excessive heat that must be continuously transferred away from the spindle body to avoid overheating and thermal expansion. Various cooling jacket channel designs have been studied in literature [63]. From these studies, it was concluded that the cooling channel geometry does not significantly affect heat transfer. However, channel geometry can dramatically affect the pressure drop [64]. Keeping these factors in mind, the quasi-parallel channel design shown in Figure 48 was finalized to minimize pressure drop. The fin dimensions were optimized via simulation to maximize heat transfer efficiency. A high surface roughness of 100 microns will be maintained at heat transfer surfaces to improve efficiency. Figure 48 indicates the faces with intentionally rough surfaces.

Figure 48: Motor cooling jacket design

The cooling jacket can only cool the external surface of the stator. For the internal volume of the motor chamber, a pneumatic system will be used to maintain air flow for cooling via the inlet and outlet points indicated in Figure 49. Thus, the motor cooling jacket also has cooling fins on its internal surface. The fin dimensions are optimized for maximum forced convection coefficient. As with the water cooling surfaces, the surface roughness of air-cooling surfaces is also kept high for maximum heat transfer, as shown in Figure 50. It also shows that this roughness requirement was only met for the round faces of the fins. The internal surfaces of the fins were coated with the adhesive used for assembling the motor stator winding, creating a smoother surface. This can potentially decrease the cooling effect created by air.

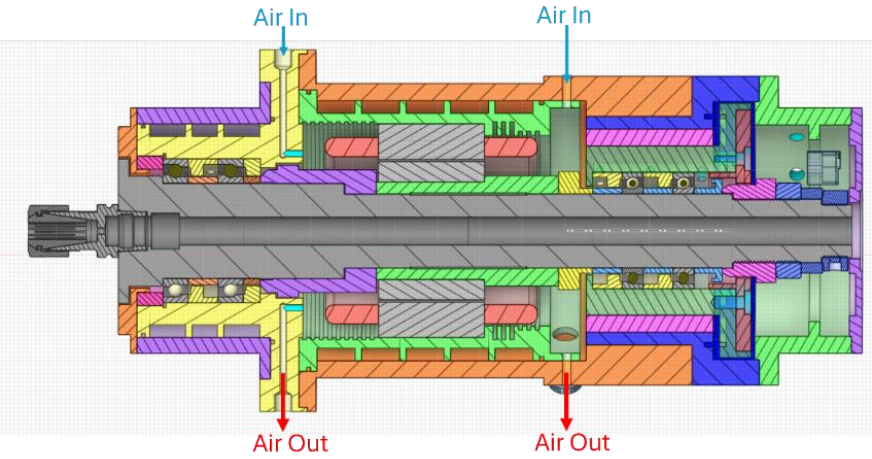

Figure 49: Pneumatic cooling channels

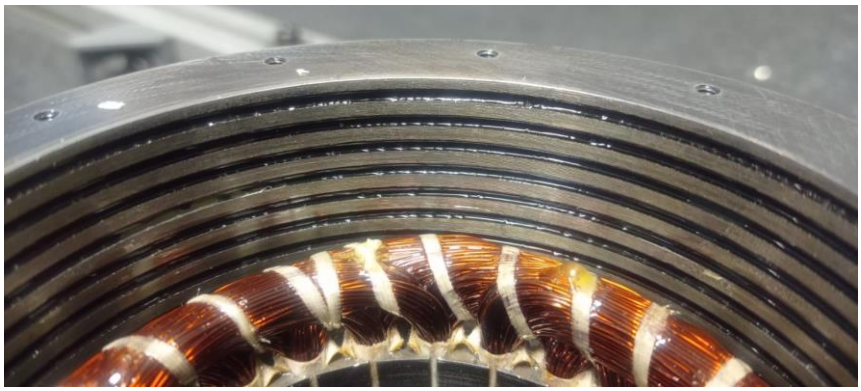

Figure 50: Cooling fins for motor air cooling

4.3.2. Bearing Cooling

Design Considerations

A separate cooling jacket is designed for cooling the front bearing set. The jacket has a 3-pass channel design, and the coolant passages are kept as close as possible to the bearing outer rings (Figure 51). Designing these components took significant time as this unit houses the bearings, has cooling channels, bearing lubrication channels, and sealing requirements. Moreover, it is an important assembly component that connects to multiple other parts.

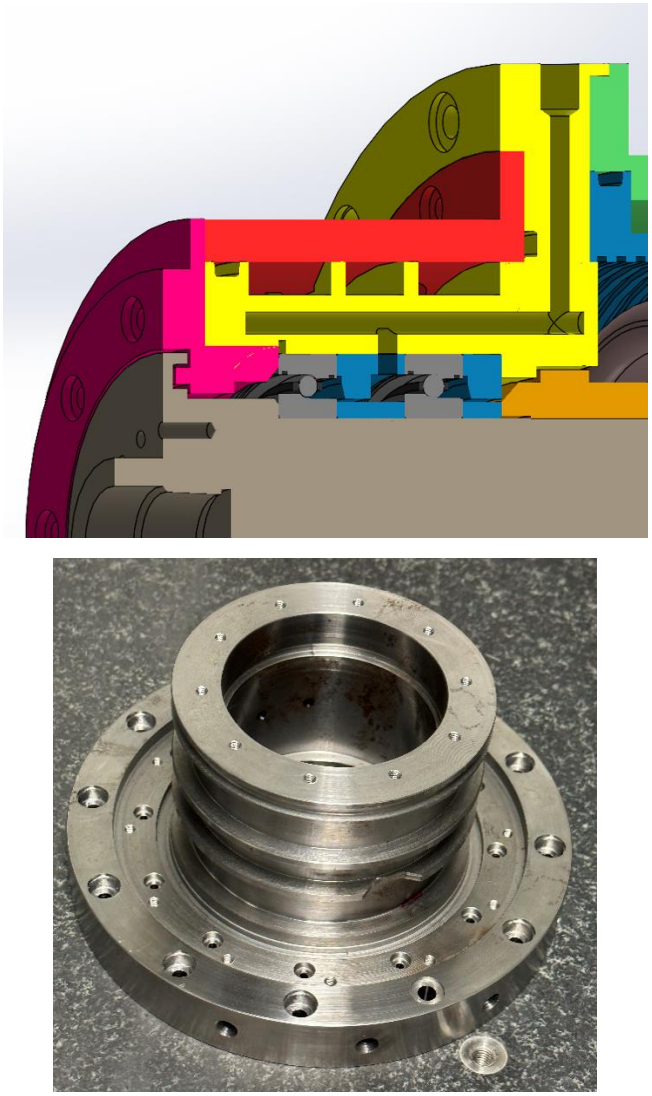

Figure 51: Front bearing cooling jacket design

The rear bearing set is floating and not as sensitive to thermal changes due to its distance from the spindle tip. Thus, no cooling jacket is provided on the rear side.

Manufacturing Considerations

Due to the intricacy of this system, separate dimensional and form tolerances were applied to its components. To adequately house the front bearing set, it should have minimal axial and radial misalignments, a loose fit with the bearing outer rings, and a fine surface finish to avoid damaging the bearings. The cooling surface will have a surface roughness of 100 microns to facilitate heat transfer. These requirements were communication to the production experts through technical drawings.

The mechanical connectors used to connect the water supply to the cooling system were installed to the parts using laser welding (Figure 52).

Figure 52: Mechanical connectors for cooling water supply

4.4. Lubrication System

Design Considerations

The lubrication system is vital for keeping the bearings in optimal working condition throughout the speed range. Since the targeted spindle speed is high, conventional grease-based lubricants are insufficient. Oil-air lubrication is best-suited for this application. In this system, a compressed oil-air mist is injected into the lubrication channel at specific time intervals. The precision metering of the oil volume injects just enough lubricant to

minimize friction and wear, and it avoids over-lubrication, which negatively affects the bearings by increasing viscous friction. Moreover, the compressed air flow also creates an additional cooling effect for the rolling elements inside the bearings including the balls and the cage.

Using an oil-air system requires designing nozzles and drainage chambers inside the spacers for precisely directing the mist flow inside the bearing. Details of these features were shared in section 4.2.2.4.

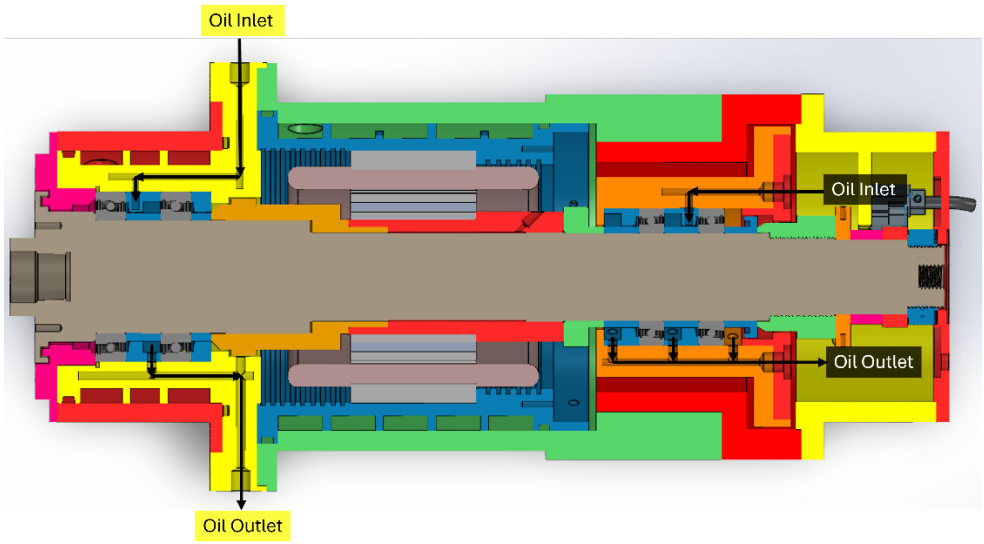

Figure 53: Bearing lubrication channels

Figure 53 shows a cross-section view of one of the planes carrying the lubrication channels. There are two such planes at a 30° angle as there are two bearings in each set. The mist is first injected into the channels built into the housing components. These channels open into the nozzles built into the bearing spacers, which will be aligned to match the channel exits of the housing.

The front side lubrication channels are incorporated into the cooling jacket. For the rear side, the channels are kept isolated from the housing to accommodate small movements caused by thermal expansions.

Manufacturing Considerations

Developing a manufacturable design with several internal channels was time-consuming. Figure 54 shows a 2D view of the front side cooling jacket with all hidden features.

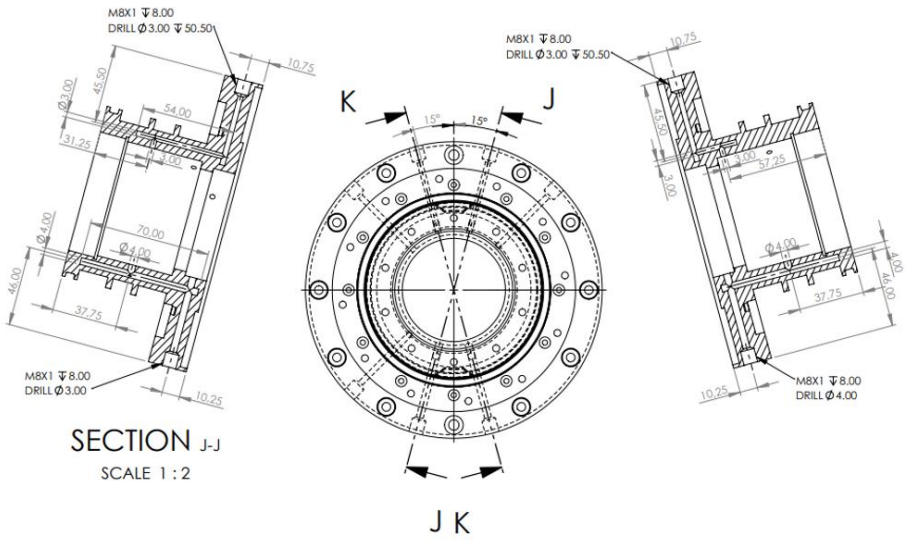

Figure 54: Technical drawing view of bearing lubrication channels

Some of the radially aligned blind holes were not possible to manufacture as their open end opened inside the cooling jacket. Thus, they were initially drilled from the outside and later blunted by laser welding (Figure 55).

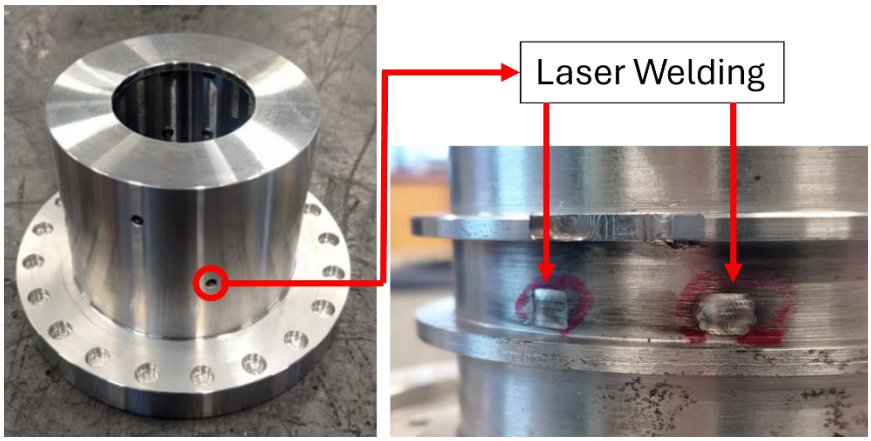

Figure 55: Laser welding operation

4.5. Sealing System

The internal environment of the spindle is filled with different fluids for cooling and lubricating key components. This creates leakage concerns in many areas. Thus, an appropriate sealing system was included in the design to have a contained volume chamber for each fluid.

4.5.1. Coolant Sealing

O-rings are included at the interfaces where there is a risk of the coolant leaking out. The O-ring locations are indicated in Figure 56. Based on the working coolant temperature range of 18-40ºC and the operating pressure of maximum 3 bars, standard nitrile rubber (NBR) O-rings were selected.

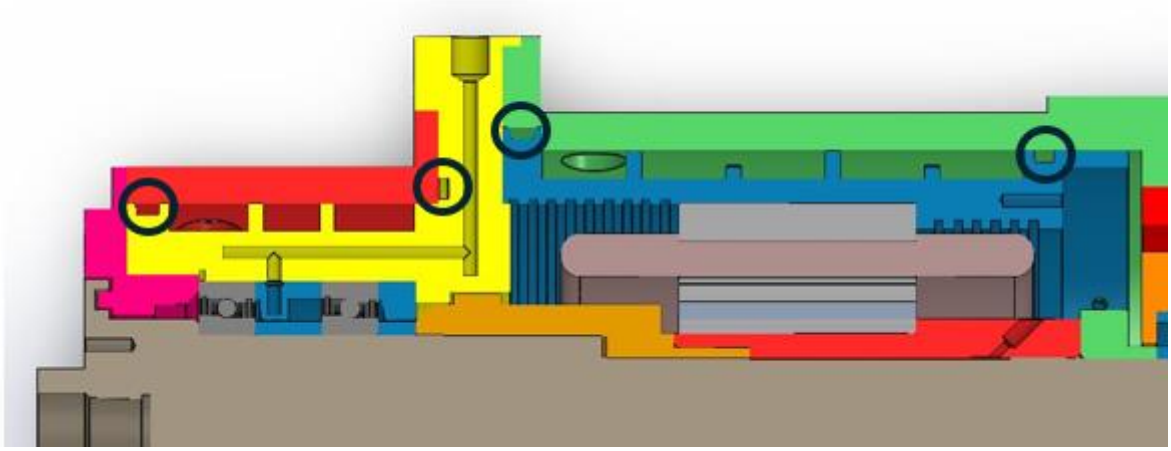

Figure 56: O-Ring locations

Appropriate care must be exercised in designing the O-ring grooves to prevent leakage and O-ring damage. Desing guidelines from the O-ring manufacturer Parker were used to define the dimensions and finish requirements for these grooves [65]. Figure 57 shows an example technical drawing of one of the grooves.

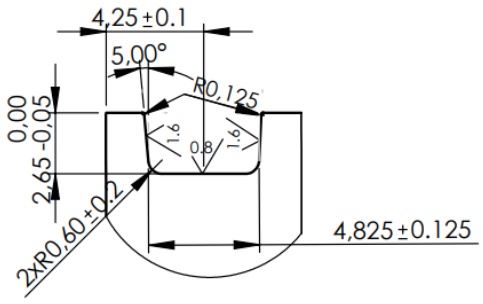

Figure 57: Technical drawing view of O-Ring groove design

Additionally, pipe connectors with built-in O-ring seals will be used at the inlet and outlet points of the coolant.

4.5.2. Lubricant Sealing

The lubricant is in the form of a mist, which requires a different sealing approach. Labyrinth seals are included in the design at core interfaces to prevent oil leaking. The labyrinths designed for the front bearing set are shown in Figure 58. The efficiency of this is further increased by maintaining a constant air flow through the motor chamber, as explained before. This provides extra pressure on one side of the labyrinth seal.

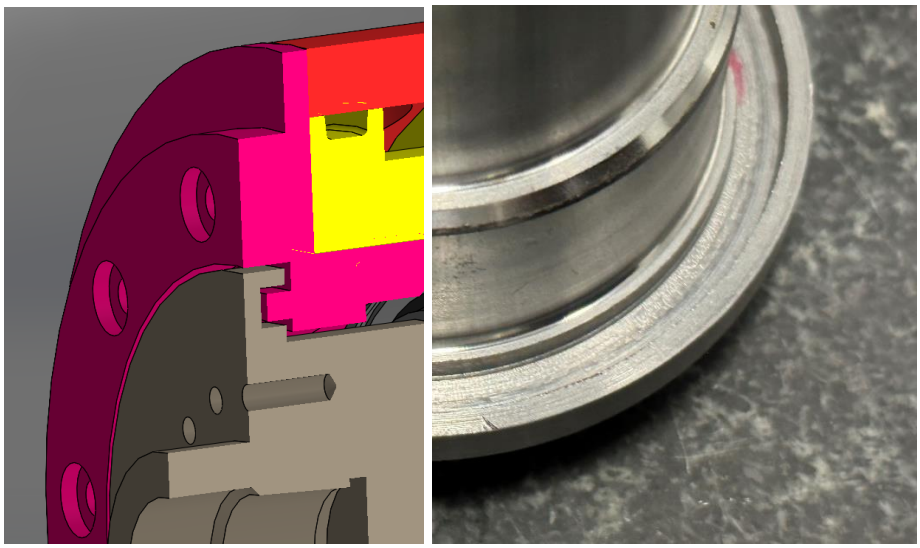

Figure 58: Labyrinth seal feature on shaft

The lubricant exit channels are kept slightly larger (4mm) than the inlets (3mm) to ensure efficient evacuation of the oil-air mist from the system, which further reduces chances of leakages.

4.6. Electric System

The electric system comprises the electric motor, drive, and encoder. The 3 Nm motor is installed directly on the shaft and necessary provisions are made for its cooling and efficient power transmission. A hole had to be provided for passing its wiring. The drive will be mounted at an external platform.

For speed and position feedback, an incremental magnetic encoder will be used. The magnetic ring of the encoder will be mounted on the rear side of the shaft and fixed by a precision locknut (Figure 59). To ensure adequate mounting force, a press fit of r6 will be used as guided by the manufacturer.

The readhead of the encoder picks up the trigger signal from the encoder ring. Thus, it needs to be mounted accurately. A special mounting bracket was designed based on the manufacturer's guidelines and incorporated in the rear housing.

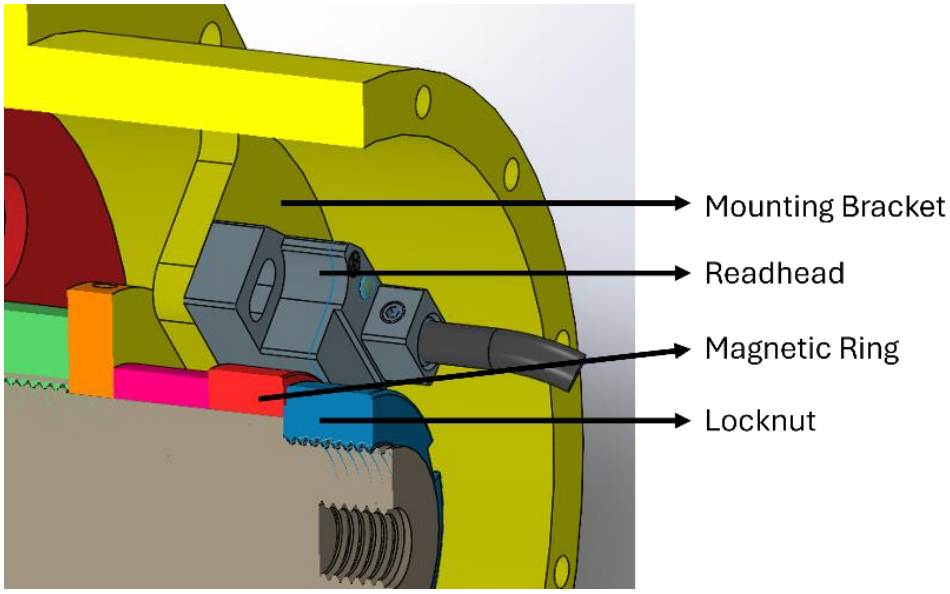

Figure 59: Mounting bracket for encoder unit

4.7. Assembly

In total, this spindle will comprise ~150 parts including the aforementioned components, fasteners, connectors, and peripheral devices. At the time of writing this thesis, the assembly of the spindle is underway. Its development will be shared in future publications. The current state of some of the parts is shared in Figure 60.

Figure 60: Manufactured spindle components

4.8. Summary

This chapter covers different aspects of high-speed spindle design and manufacturing. The key observations and challenges faced by our research group in this project are highlighted. The main design decisions and their justifications are provided.

Various manufacturing considerations like design for manufacturing, tolerancing, and fabrication are also discussed.

5. MACHINE LEARNING-ASSISTED REVERSE IDENTIFICATION OF SPINDLE PARAMETERS

The use of data-based methods and machine learning is rapidly growing in the machine tools industry [66]. It has major applications like generative design, process optimization, system identification, and fault diagnosis. Spindles, being complex and a rich source of data, are one of the well-studied topics in literature. Recognizing this as an opportunity, a side-study was planned as an offshoot of this work, which is still an ongoing effort at the time of writing this thesis. This chapter briefly introduces this work and presents a proof-of-concept study.

In this work, one of the core focus areas was optimizing the spindle's FRF by manipulating shaft dimensions and bearing stiffness parameters. It was observed, quite understandably, that there is a one-to-one relationship between these input parameters and the FRF output. In other words, each spindle FRF is the unique product of its specific combination of inputs like dimensions, bearings, materials, and assembly procedures. This implies that by having knowledge of one of these sets of information, the other may be possible to predict.

Researchers have historically used this understanding to predict the spindle FRF from design parameters. More recently, works like [67] and [68] have also leveraged machine learning techniques for this. There is, however, no known study that has attempted this in the reverse direction. The forward direction prediction has well-known benefits. For example, by identifying the spindle- or tooltip FRF, among other vibration characteristics, one can design systems for applications like chatter suppression [5], spindle health monitoring [69], [70], and tool wear analysis [71]. Similarly, performing this in reverse

can potentially open doors to new applications like identifying structural faults, bearing faults, process planning, etc.

5.1. Methodology

A proof-of-concept study was designed to test the viability of a reverse identification system. The simple spindle geometry shown in Figure 61 is chosen for this. It has three beam sections, and two bearings arranged in O-configuration. Both bearings were taken to be the same model for now.

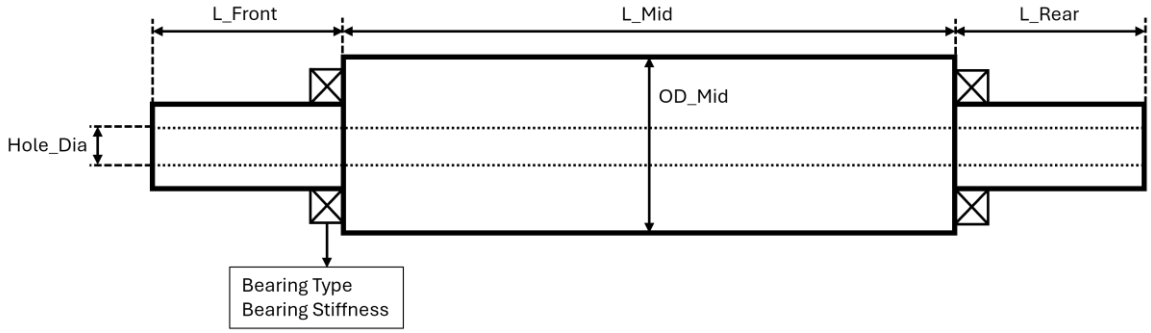

Figure 61: Spindle geometry for reverse identification

The schematic in Figure 62 illustrates the methodology adapted for this study. Initially, a design domain was chosen for the spindle parameters selected for reverse identification. Then a comprehensive database was generated using RCSA with different permutations of these parameters. The outputs are the modal parameters (modal frequencies, stiffnesses, and damping) extracted from the FRF computed at each iteration. In this work, the half-power method has been used to extract the modal parameters.

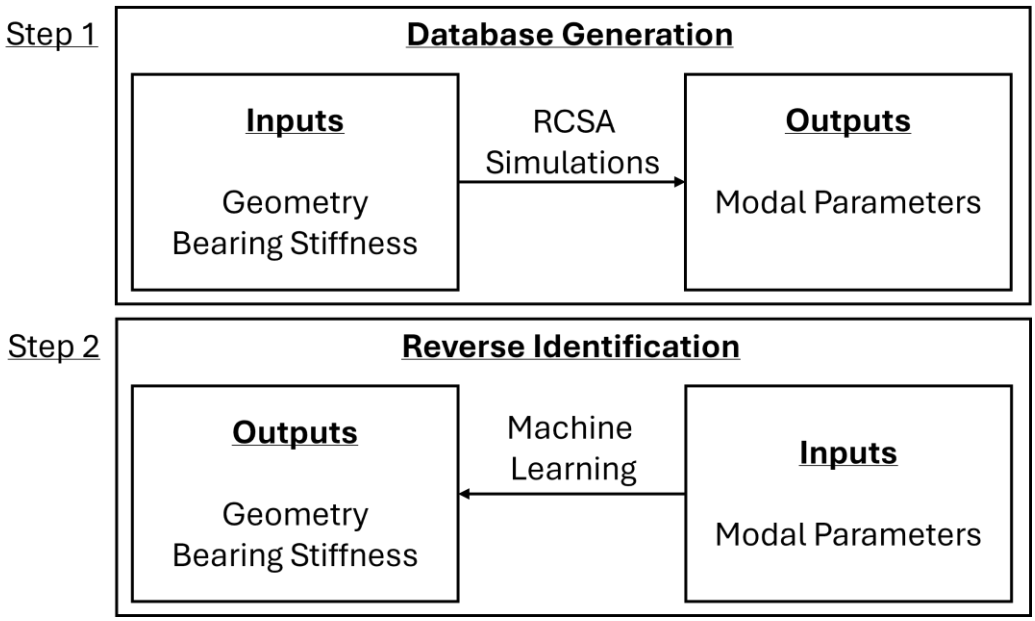

Figure 62: Machine learning-assisted reverse identification methodology

After this database was developed, it was used as the training data for machine learning-assisted reverse identification. Since the goal is to predict the structure from the modal parameters, the inputs and outputs were swapped with each other at this stage.

5.2. Database Generation

The first step in the database preparation process was to define reasonable limits for the input parameters. The selection should be such that significant variations are seen in the output FRF, and also conservative enough to keep the problem within manageable bounds. The size of the database, and the number of simulations to be run, increases exponentially with more parameters and wider limits. The composition of the finalized database inputs is shared in Table 9. The parameters were also chosen based on practical considerations for a similar-sized spindle. Moreover, the FRFs were computed in the range of 0-4000 Hz, considering the reliability of general modal analysis kits utilized in most shop floors or academic labs.

Variable	Type	Range
L_Front	Continuous	2.5-90 mm
L_Rear	Continuous	2.5-90 mm
L_Mid	Discrete	[130, 150, 170] mm
OD_Mid	Discrete	[30, 40, 50] mm
Hole_Dia	Discrete	[0, 20] mm
Bearing Preload	Continuous	10-100 N
Bearing Type	Discrete	Steel Balls, Ceramic Balls

Table 9: Input variables for database generation

To ensure that the database contains only relevant and useful information, a few steps were taken based on domain knowledge. Firstly, the following two filters were applied for picking modes from the FRF:

- Modes with peak modal amplitude less than 10% of maximum FRF amplitude were filtered out.
- Modes with natural frequencies of more than 3500 Hz were filtered out.

Checks were programmed into the code that were triggered in case any two modes occurred very close to each other (within 100 Hz). When this is the case, modal parameter extraction with the half-power method may not yield accurate results, requiring supervision. After the simulations were run, the cases where this check was triggered were checked manually and either confirmed to be accurate or removed from the database.

Finally, one of the important issues to consider here was the number of modes to capture. There can be any number of modes in an FRF within a fixed frequency window, depending upon factors like bearing stiffnesses and structural rigidity. For low stiffness cases, the number of modes increases, and vice versa. For the selected design domain, the number of modes varied between 1 to 3. Therefore, the database output consists of nine features: three modal parameters for each mode. For FRF data with less than three modes, the features for high frequency modes were taken as zero.

In the end, a database with 68,040 samples was generated using the defined parameters and checks.

5.3. Machine Learning-Assisted Reverse Identification

The generated database was used to perform the reverse identification task by taking the modal parameters as inputs and the design parameters as the output target variables. Initially, various machine learning algorithms were tested using standard toolboxes. Based on the observations, it was decided to use the XGBoost algorithm [72] for this task as it outperformed other algorithms. The implementation was performed in a Python 3.0 environment using standard packages like scikit-learn and pandas. Hyperparameter optimization was performed using the hyperopt package [73]

Another important issue to address here was to decide between using single-output and multi-output algorithms. The database has six target variables which are interdependent. Thus, using a multi-output approach made sense. However, based on preliminary testing with multi-output and single-output versions of XGBoost, it was decided to move forward with single-output machine learning models due to their superior performance on the dataset in question. While this may be counterintuitive, the multi-output version of XGBoost (multi-vector leaf method) was still in an unrefined, experimental phase, which may have caused its performance to be inadequate.

Therefore, six different models were trained for each target variable. Since some of the target variables were continuous and others categorical, an appropriate selection between regression and classification models was applied. The evaluation metrics were selected as accuracy and r2 scores for classification and regression tasks, respectively.

To evaluate the efficiency of the developed models on unseen data, 10% of the dataset was kept aside initially as an ‘unseen dataset’. This dataset did not pass through the code and was reserved for final evaluation after the entire training was finished. The train-test split was kept at 80:20 for the remaining dataset.

Variable	Problem Type	Accuracy/r2 Score	Accuracy/r2 Score on Unseen Dataset
Stiffness	Regression	94%	94%
L_Front	Regression	99%	99%
L_Rear	Regression	99%	99%
Length	Classification	93%	93.5%
OD_Mid	Classification	99%	99%
Hole_Dia	Classification	94%	94.3%

Table 10: Summary of machine learning results

The results are summarized in Table 10. The machine learning models are well-suited for the problem as the performance metrics are all higher than 90%. Moreover, the performances are comparable between the seen and unseen datasets, indicating that the algorithm is capable of learning the internal variations of the dataset.

To visually illustrate the performance of the trained machine learning models, three cases were randomly picked from the dataset and predicted with the trained models. The FRF plots of these predictions are shared in Figure 63, which shows strong resemblance in the real and predicted values. In case 1, the second mode is not captured as it occurs after 3,500 Hz, which was filtered out. The first mode, however, is accurately predicted. In cases 2 and 3, there are small discrepancies that are reasonable when dealing with experimental data and can be improved with manual fine-tuning techniques.

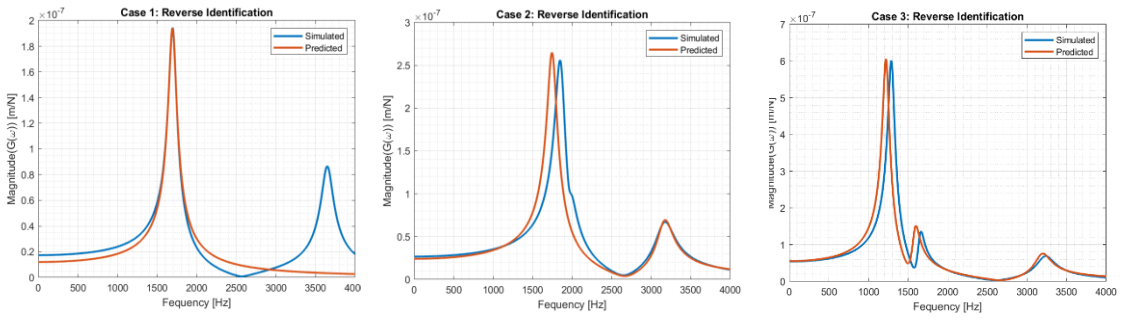

Figure 63: FRF plots of machine learning predictions

5.4. Conclusion & Future Recommendations

In this chapter, a basic study for the reverse identification of spindle parameters was presented. The results of this study offer strong proof of concept in favor of using the used database-assisted approach. The fact that FRFs are unique indicators of the internal structures of spindles makes this application worthy of further inspection.

These results, however, do not provide a guarantee that such a system would be sustainable on a more complex scale. There are various avenues of improvement that can be further explored, which will be presented in future works. Some of the possible recommendations are briefly discussed below.

- A more complex and realistic spindle structure can be studied. In reality, machine tool spindles are the result of several variables, which highly complicate the problem of generating informative databases.
- The use of experimental data can be added to the problem, both for verification of the models and enhancing the prediction capabilities in real-life scenarios.
- Better-performing machine learning algorithms and techniques can be explored. Similarly, multi-output models may also be used to investigate the problem.

6. CONCLUSIONS & RECOMMENDATIONS

This chapter concludes this thesis and highlights the main contributions of this work. Recommendations for future work are also discussed.

6.1. Thesis Contributions

The major contributions of this work on the design, optimization, and manufacturing of high-speed spindles are:

1. A multi-objective optimization scheme is implemented with numerous objectives and variables, showcasing its extensive capabilities in analyzing complex engineering systems. The full application of these schemes is still underutilized. This work can perhaps contribute to the broader adoption of these techniques.
2. A holistic, design-guided optimization strategy was adopted in this project. It demonstrates that, for complex systems like machine tool spindles, the optimization approach should be implemented from start to finish and regularly revised based on the prevalent design and constraints. This work offers a framework for engineering designers to develop practical optimization strategies.

3. Detailed notes are included regarding practical design and manufacturing aspects of high-speed spindles, providing valuable insights to those interested in learning about these topics.

6.2. Conclusions

This thesis focused on numerous aspects of high-speed spindles. The characteristic dynamic and thermal behaviors of high-speed spindles were initially discussed, for which the Receptance Coupling Substructural Analysis (RCSA) method and Finite Element Methods (FEM) are used, respectively. These models were integrated with the code developed for a multi-objective optimization scheme based on the Teaching Learning Based Optimization (TLBO) method and Non-Dominated Sorting Algorithm (NSGA-III).

The optimization is conducted as a four-stage process. The first stage identifies various shaft dimensions and bearing preloads as the most sensitive design variables. In the second and third stages, multi-objective optimization problems are developed based on the current status and implications of the spindle design. The optimization successfully revealed conflicting trends between the dynamic and thermal spindle behaviors through well-defined pareto fronts and was able to enhance performance by exploiting the dynamic absorber effect. In the last stage, a final sensitivity analysis is performed to serve as a reference during spindle assembly.

The practical implications in designing and manufacturing a high-speed spindle are also discussed in detail. The design intent behind main subsystems, their integration, and implementation from a production point of view are commented upon. These comments signify the challenges of designing and manufacturing a machine tool spindle with an academic perspective in mind.

6.3. Future Recommendations

This work can be furthered by considering the following recommendations.

- Although the stepwise design-guided optimization approach is beneficial practically, a broader, universal optimization with all variables and more objective functions can also be investigated to further test the efficiency of the multi-objective optimization scheme.
- The optimization studies are conducted for either static conditions or maximum rotational speed i.e. 40,000 RPM. Expanding the optimization approach to cover the entire speed range can add more depth to the study.
- Verification of the optimization results with FE analyses or experimental data can be beneficial.
- The cooling system has been previously investigated due to its sensitive behaviors [35]. While the cooling system dimensions were separately optimized, extending the thermal modelling to include the cooling system parameters can enlarge the scope of the core thermal-dynamic optimization problem.
- The constant preload mechanism is used in our design, which maintains axial preload in bearings at elevated temperatures. The radial preload, however, may still increase to non-negligible levels at high speeds. Investigating this thermally induced radial preload can increase the efficiency of both dynamic and thermal modules.

BIBLIOGRAPHY

[1] "Kapil" "Gupta" and ' J. Paulo' "Davim," High Speed Machining. 2020.

[2] E. Abele, Y. Altintas, and C. Brecher, "Machine tool spindle units," CIRP Ann Manuf Technol, vol. 59, no. 2, pp. 781–802, 2010, doi: 10.1016/j.cirp.2010.05.002.

[3] M. Postel, O. Özsahin, and Y. Altintas, "High speed tooltip FRF predictions of arbitrary tool-holder combinations based on operational spindle identification," Int J Mach Tools Manuf, vol. 129, pp. 48–60, Jun. 2018, doi: 10.1016/j.ijmachtools.2018.03.004.

[4] B. Bediz, B. Arda Gozen, E. Korkmaz, and O. Burak Ozdoganlar, "Dynamics of ultra-high-speed (UHS) spindles used for micromachining," Int J Mach Tools Manuf, vol. 87, pp. 27–38, 2014, doi: 10.1016/j.ijmachtools.2014.07.007.

[5] Y. Altinta9 and E. Budak, "Analytical Prediction of Stability Lobes in Milling."

[6] H. Li and Y. C. Shin, "Integrated dynamic thermo-mechanical modeling of high speed spindles, part 2: Solution procedure and validations," J Manuf Sci Eng, vol. 126, no. 1, pp. 159–168, 2004, doi: 10.1115/1.1644546.

[7] C. W. Lin, J. F. Tu, and J. Kamman, "An integrated thermo-mechanical-dynamic model to characterize motorized machine tool spindles during very high speed rotation," Int J Mach Tools Manuf, vol. 43, no. 10, pp. 1035–1050, Aug. 2003, doi: 10.1016/S0890-6955(03)00091-9.

[8] B. Fang, J. Zhang, S. Wan, and J. Hong, "Determination of optimum preload considering the skidding and thermal characteristic of high-speed angular contact ball bearing," Journal of Mechanical Design, vol. 140, no. 5, May 2018, doi: 10.1115/1.4039386.

[9] Y. Cao and Y. Altintas, "Modeling of spindle-bearing and machine tool systems for virtual simulation of milling operations," Int J Mach Tools Manuf, vol. 47, no. 9, pp. 1342–1350, Jul. 2007, doi: 10.1016/j.ijmachtools.2006.08.006.

[10] A. Matsubara, T. Yamazaki, and S. Ikenaga, "Non-contact measurement of spindle stiffness by using magnetic loading device," Int J Mach Tools Manuf, vol. 71, pp. 20–25, 2013, doi: 10.1016/j.ijmachtools.2013.04.003.

[11] A. B. Jones, "A General Theory for Elastically Constrained Ball and Radial Roller Bearings Under Arbitrary Load and Speed Conditions," 1960. [Online]. Available: http://fluidsengineering.asmedigitalcollection.asme.org/

[12] J. M. Vree and D. A. Maas, “Equilibrium and Associated Load Distribution in Ball and Roller Bearings Loaded in Five Degrees of Freedom While Neglecting Friction-Part 11: Application to Roller Bearings and Experimental Verification,” 1989. [Online]. Available: http://www.asme.org/terms/Terms_Use.cfm

[13] P. K. Gupta, “Dynamics of Rolling-Element Bearings Part IV: Ball Bearing Results,” 1979. [Online]. Available: http://www.asme.org/about-asme/terms-of-use

[14] S. W. Hong and V. C. Tong, “Rolling-element bearing modeling: A review,” Dec. 01, 2016, SpringerOpen. doi: 10.1007/s12541-016-0200-z.

[15] A. Ertürk, E. Budak, and H. N. Özgüven, “Selection of design and operational parameters in spindle-holder-tool assemblies for maximum chatter stability by using a new analytical model,” Int J Mach Tools Manuf, vol. 47, no. 9, pp. 1401–1409, Jul. 2007, doi: 10.1016/j.ijmachtools.2006.08.016.

[16] O. Özşahin, A. Ertürk, H. N. Özgüven, and E. Budak, “A closed-form approach for identification of dynamical contact parameters in spindle-holder-tool assemblies,” Int J Mach Tools Manuf, vol. 49, no. 1, pp. 25–35, Jan. 2009, doi: 10.1016/j.ijmachtools.2008.08.007.

[17] H. Li and Y. C. Shin, “Analysis of bearing configuration effects on high speed spindles using an integrated dynamic thermo-mechanical spindle model,” Int J Mach Tools Manuf, vol. 44, no. 4, pp. 347–364, Mar. 2004, doi: 10.1016/j.ijmachtools.2003.10.011.

[18] C. Rabréau, D. Noël, S. Le Loch, M. Ritou, and B. Furet, “Phenomenological model of preloaded spindle behavior at high speed,” International Journal of Advanced Manufacturing Technology, vol. 90, no. 9–12, pp. 3643–3654, Jun. 2017, doi: 10.1007/s00170-016-9702-1.

[19] by Kazi Sher Ahmed, “DESIGN OF ACTIVE MAGNETIC BEARING SPINDLES FOR MICRO-MILLING APPLICATIONS,” 2021.

[20] G. Liu, J. Hong, W. Wu, and Y. Sun, “Investigation on the influence of interference fit on the static and dynamic characteristics of spindle system,” International Journal of Advanced Manufacturing Technology, vol. 99, no. 5–8, pp. 1953–1966, Nov. 2018, doi: 10.1007/s00170-018-2567-8.

[21] B. Bossmanns and J. F. Tu, “A thermal model for high speed motorized spindles,” 1999.

[22] J. S. Chen and W. Y. Hsu, “Characterizations and models for the thermal growth of a motorized high speed spindle,” Int J Mach Tools Manuf, vol. 43, no. 11, pp. 1163–1170, Sep. 2003, doi: 10.1016/S0890-6955(03)00103-2.

[23] T. Liu et al., “Analytical modeling for thermal errors of motorized spindle unit,” Int J Mach Tools Manuf, vol. 112, pp. 53–70, Jan. 2017, doi: 10.1016/j.ijmachtools.2016.09.008.

[24] Q. Meng, X. Yan, C. Sun, and Y. Liu, “Research on thermal resistance network modeling of motorized spindle based on the influence of various fractal parameters,” International Communications in Heat and Mass Transfer, vol. 117, Oct. 2020, doi: 10.1016/j.icheatmasstransfer.2020.104806.

[25] B. R. Jorgensen and Y. C. Shin, “Dynamics of Machine Tool Spindle/Bearing Systems Under Thermal Growth,” 1997. [Online]. Available: http://www.asme.org/about-asme/terms-of-use

[26] T. Hamada, K. Yura, R. Assistant, and K. Hitomi, “Multiobjective Design Optimization of Machine-Tool Spindles,” 1984. doi: 10.1115/1.3258560.

[27] J. Hoyt, “Machine tool spindle design.” [Online]. Available: https://scholarworks.rit.edu/theses

[28] O. Maeda, Y. Cao, and Y. Altintas, “Expert spindle design system,” Int J Mach Tools Manuf, vol. 45, no. 4–5, pp. 537–548, Apr. 2005, doi: 10.1016/j.ijmachtools.2004.08.021.

[29] C. W. Lin and J. F. Tu, “Model-based design of motorized spindle systems to improve dynamic performance at high speeds,” J Manuf Process, vol. 9, no. 2, pp. 94–108, 2007, doi: 10.1016/S1526-6125(07)70111-1.

[30] Y. Mohammadi, M. Azvar, and E. Budak, “Suppressing vibration modes of spindle-holder-tool assembly through FRF modification for enhanced chatter stability,” CIRP Annals, vol. 67, no. 1, pp. 397–400, Jan. 2018, doi: 10.1016/j.cirp.2018.03.003.

[31] S. M. Kim and S. K. Lee, “Spindle housing design parameter optimization considering thermo-elastic behaviour,” International Journal of Advanced Manufacturing Technology, vol. 25, no. 11–12, pp. 1061–1070, Jun. 2005, doi: 10.1007/s00170-003-1958-6.

[32] H. tao Yue, C. guang Guo, Q. Li, L. juan Zhao, and G. bo Hao, “Thermal error modeling of CNC milling machining spindle based on an adaptive chaos particle swarm optimization algorithm,” Journal of the Brazilian Society of Mechanical Sciences and Engineering, vol. 42, no. 8, Aug. 2020, doi: 10.1007/s40430-020-02514-z.

[33] K. Fan, R. Gao, H. Zhou, Y. Zhao, S. Tian, and Y. Xie, “An optimization method for thermal behavior of high-speed spindle of gear form grinding machine,” International Journal of Advanced Manufacturing Technology, vol. 107, no. 1–2, pp. 959–970, Mar. 2020, doi: 10.1007/s00170-020-05095-2.

[34] L. Koch, K. Gross, and G. Krueger, “Special Issue | ICTIMT2021 2 nd International Conference on Thermal Issues in Machine Tools ICTIMT2021-035 COMPARATIVE ANALYSIS OF FLUID COOLING SYSTEMS IN MOTORIZED SPINDLES,” 2021, doi: 10.17973/MMSJ.2021_07_2021068.

[35] K. Y. Li, W. J. Luo, and S. J. Wei, “Machining accuracy enhancement of a machine tool by a cooling channel design for a built-in spindle,” Applied Sciences (Switzerland), vol. 10, no. 11, Jun. 2020, doi: 10.3390/app10113991.

[36] V. C. Tong, J. Hwang, J. Shim, J. S. Oh, and S. W. Hong, “Multi-objective Optimization of Machine Tool Spindle-Bearing System,” International Journal of Precision Engineering and Manufacturing, vol. 21, no. 10, pp. 1885–1902, Oct. 2020, doi: 10.1007/s12541-020-00389-7.

[37] Q. Yi, C. Li, Q. Ji, D. Zhu, Y. Jin, and L. Li, “Design optimization of lathe spindle system for optimum energy efficiency,” J Clean Prod, vol. 250, Mar. 2020, doi: 10.1016/j.jclepro.2019.119536.

[38] J. L. J. Pereira, G. A. Oliver, M. B. Francisco, S. S. Cunha, and G. F. Gomes, “A Review of Multi-objective Optimization: Methods and Algorithms in Mechanical Engineering Problems,” Jun. 01, 2022, Springer Science and Business Media B.V. doi: 10.1007/s11831-021-09663-x.

[39] T. L. Schmitz, “Predicting high-speed machining dynamics by substructure analysis,” CIRP Ann Manuf Technol, vol. 49, no. 1, pp. 303–308, 2000, doi: 10.1016/S0007-8506(07)62951-5.

[40] A. Ertürk, H. N. Özgüven, and E. Budak, “Analytical modeling of spindle-tool dynamics on machine tools using Timoshenko beam model and receptance coupling for the prediction of tool point FRF,” Int J Mach Tools Manuf, vol. 46, no. 15, pp. 1901–1912, Dec. 2006, doi: 10.1016/j.ijmachtools.2006.01.032.

[41] W. Weaver Jr, S. P. Timoshenko, and D. H. Young, Vibration problems in engineering. John Wiley & Sons, 1991.

[42] A. Ertürk, “DYNAMIC MODELING OF SPINDLE-TOOL ASSEMBLIES IN MACHINING CENTERS A THESIS SUBMITTED TO THE GRADUATE SCHOOL OF NATURAL AND APPLIED SCIENCES OF MIDDLE EAST TECHNICAL UNIVERSITY,” 2006.

[43] H. Li and Y. C. Shin, “Integrated dynamic thermo-mechanical modeling of high speed spindles, part 1: Model development,” J Manuf Sci Eng, vol. 126, no. 1, pp. 148–158, 2004, doi: 10.1115/1.1644545.

[44] “https://www.akimmetal.com.tr/tr/uretim/motor-uretim-3.”

[45] R. V. Rao, V. J. Savsani, and D. P. Vakharia, “Teaching-learning-based optimization: A novel method for constrained mechanical design optimization problems,” CAD Computer Aided Design, vol. 43, no. 3, pp. 303–315, Mar. 2011, doi: 10.1016/j.cad.2010.12.015.

[46] R. V. Rao, “Teaching Learning Based Optimization Algorithm And Its Engineering Applications.”

[47] K. Deb, A. Pratap, S. Agarwal, and T. Meyarivan, “A fast and elitist multiobjective genetic algorithm: NSGA-II,” IEEE Transactions on Evolutionary Computation, vol. 6, no. 2, pp. 182–197, Apr. 2002, doi: 10.1109/4235.996017.

[48] K. Deb and H. Jain, “An Evolutionary Many-Objective Optimization Algorithm Using Reference-point Based Non-dominated Sorting Approach, Part I: Solving Problems with Box Constraints,” 2013. [Online]. Available: http://www.egr.msu.edu/

[49] H. Jain and K. Deb, “An Evolutionary Many-Objective Optimization Algorithm Using Reference-point Based Non-dominated Sorting Approach, Part II: Handling Constraints and Extending to an Adaptive Approach,” 2013. [Online]. Available: http://www.egr.msu.edu/

[50] F. Zou, L. Wang, X. Hei, D. Chen, and B. Wang, “Multi-objective optimization using teaching-learning-based optimization algorithm,” Eng Appl Artif Intell, vol. 26, no. 4, pp. 1291–1300, Apr. 2013, doi: 10.1016/j.engappai.2012.11.006.

[51] H. R. Tizhoosh, “Opposition-Based Learning: A New Scheme for Machine Intelligence,” 2005.

[52] “Mostapha Kalami Heris, NSGA-III: Non-dominated Sorting Genetic Algorithm, the Third Version — MATLAB Implementation (URL: https://yarpiz.com/456/ypea126-nsga3), Yarpiz, 2016.”

[53] E. Zitzler, K. Deb, and L. Thiele, “Comparison of Multiobjective Evolutionary Algorithms: Empirical Results.”

[54] X. Li, Y. Xue, Y. Yu, D. Si, and D. Li, “Analysis for Thermal Characteristics of High-Speed Angular Contact Ball Bearing under Different Preload,” 2018.

[55] G. Karataş, O. Özşahin, H. N. Özgüven, and E. Budak, “Design optimization of tool holder extension for enhanced chatter stability by using component mode tuning method,” in Procedia CIRP, Elsevier B.V., 2020, pp. 294–297. doi: 10.1016/j.procir.2021.02.033.

[56] S. Hayati, M. Shahrokhi, and A. Hedayati, “Development of a frictionally damped boring bar for chatter suppression in boring process”, doi: 10.1007/s00170-021-06791-3/Published.

[57] F. A. M. Galarza, M. V. de Albuquerque, A. Í. S. Antonialli, R. Pederiva, and A. E. Diniz, “Design and experimental evaluation of an impact damper to be used in a slender end mill tool in the machining of hardened steel,” International Journal of Advanced Manufacturing Technology, vol. 106, no. 5–6, pp. 2553–2567, Jan. 2020, doi: 10.1007/s00170-019-04786-9.

[58] F. A. Maldonado, H. W. Chen, G. A. Durazno, C. G. Helguero, and J. L. Amaya, “Stiffness and natural frequency effects on a hollow truncated conical shaft,” in Procedia CIRP, Elsevier B.V., 2022, pp. 286–291. doi: 10.1016/j.procir.2022.09.086.

[59] “NSK Technical Report.”

[60] J. P. D. ’Hartog, Mechanical Vibrations, 3rd ed. 1947.

[61] Z. Wang, Z. Wang, X. Bai, X. Zhang, and Y. Wang, “Effect of interference fit on dynamic characteristics of spindle rotor system,” Journal of the Brazilian Society of Mechanical Sciences and Engineering, vol. 44, no. 8, Aug. 2022, doi: 10.1007/s40430-022-03545-4.

[62] “Precision Ball & Roller Bearings for Machine Tools, CAT. NO. B2005E-3.”

[63] J. Mayr et al., “Thermal issues in machine tools,” CIRP Ann Manuf Technol, vol. 61, no. 2, pp. 771–791, 2012, doi: 10.1016/j.cirp.2012.05.008.

[64] M. Satrústegui De Legarra and J. Carlos Ramos González, “Thermal and hydraulic design of water-based cooling systems for electrical machines Dr. Miguel Martínez-Iturralde Maiza,” 2017.

[65] “Parker O-Ring Handbook, ORD 5700.”

[66] M. Soori, B. Arezoo, and R. Dastres, “Machine learning and artificial intelligence in CNC machine tools, A review,” Sustainable Manufacturing and Service Economics, vol. 2, p. 100009, Apr. 2023, doi: 10.1016/j.smse.2023.100009.

[67] H. Mostaghimi, S. S. Park, D. Y. Lee, S. Nam, and E. Nam, “Prediction of Tool Tip Dynamics Through Machine Learning and Inverse Receptance Coupling,” International Journal of Precision Engineering and Manufacturing, vol. 24, no. 10, pp. 1739–1752, Oct. 2023, doi: 10.1007/s12541-023-00831-6.

[68] S. S. Park, S. Amani, D. Y. Lee, J. Lee, and E. Nam, “Machine learning based substructure coupling of machine tool dynamics and chatter stability,” CIRP Annals, vol. 73, no. 1, pp. 297–300, Jan. 2024, doi: 10.1016/j.cirp.2024.04.088.

[69] C. Y. Tai and Y. Altintas, “A Physics-Based Model-Data-Driven Method for Spindle Health Diagnosis, Part I: Modeling of Geometric Faults,” J Manuf Sci Eng, vol. 146, no. 8, Aug. 2024, doi: 10.1115/1.4065062.

[70] C. Y. Tai and Y. Altintas, “A Physics-Based Model-Data-Driven Method for Spindle Health Diagnosis, Part II: Dynamic Simulation and Validation,” J Manuf Sci Eng, vol. 146, no. 8, Aug. 2024, doi: 10.1115/1.4065221.

[71] M. M. De Aguiar, A. E. Diniz, and R. Pederiva, “Correlating surface roughness, tool wear and tool vibration in the milling process of hardened steel using long slender tools,” Int J Mach Tools Manuf, vol. 68, pp. 1–10, 2013, doi: 10.1016/j.ijmachtools.2013.01.002.

[72] T. Chen and C. Guestrin, “XGBoost: A scalable tree boosting system,” in Proceedings of the ACM SIGKDD International Conference on Knowledge Discovery and Data Mining, Association for Computing Machinery, Aug. 2016, pp. 785–794. doi: 10.1145/2939672.2939785.

[73] B. Komer, J. Bergstra, and C. Eliasmith, “Hyperopt-Sklearn: Automatic Hyperparameter Configuration for Scikit-Learn,” 2014.